NORTHWESTERN UNIVERSITY

Understanding and Exploiting Electroadhesion of Human Fingertips for
High Performance Surface Haptic Applications

A DISSERTATION

SUBMITTED TO THE GRADUATE SCHOOL

IN PARTIAL FULFILLMENT OF THE REQUIREMENTS

for the degree

DOCTOR OF PHILOSOPHY

Field of Mechanical Engineering

By

Craig Daniel Shultz

EVANSTON, ILLINOIS

December 2017

ABSTRACT

Understanding and Exploiting Electroadhesion of Human Fingertips for High Performance Surface Haptic Applications

Craig Daniel Shultz

The aim of this dissertation is to make sense of nearly a century and a half's worth of observations concerning skin based electroadhesion phenomena. While this is a noble goal in and of itself, further motivation of this work is drawn from fact that the electroadhesive effect is increasingly being utilized in modern day practical applications, and appears poised for integration into the now ubiquitous touchscreen interface. It was with each of these contexts in mind that I set about resolving decades of disparate observational reports and various measurements in the literature with one another. In the course of this reckoning I was able to construct a simple, yet flexible, working model which seemingly brought everything together, and which led to predictions of future capabilities of the effect. It is my aim that the model and experiments given here will essentially show how aspects of electroadhesion may not just be better understood, but may be, in the end, actively *exploited* for practical finger based applications.

I begin by demonstrating the previously overlooked DC capabilities of electroadhesion, based on work performed in the 1920s by Johnsen and Rahbek, which is capable of producing forces on the finger an order of magnitude greater than those previously reported in the haptics literature. To model the ability of electroadhesion to generate such high force (especially at DC), I propose a unified force model, based on lumped electrical impedance parameters and an interfacial air gap, and resolve this model with those in previous reports. In this process I briefly discuss the background and specifics of the Johnsen-Rahbek effect, and include friction measurements made with my own electroadhesive surface and experimental apparatus.

Expanding from this initial DC understanding of the effect, I then set about characterizing two different variable friction electroadhesive displays using careful electrical and electrochemical impedance measurements across a broad range of frequencies. I qualitatively and quantitatively examine the properties of the skin, body, surface coating, and various electrode interface impedances in isolation using different contact interface conditions, measurement types, and custom electrical hardware. My lumped series impedance model is filled out and used to explain how all impedances are related during normal usage. The linearity of this model is shown to be valid under certain assumptions, such as high applied frequencies or small applied currents, and speculation as to the physical mechanisms underlying each impedance element is given. This analysis unambiguously verifies and expands upon the existence of the hypothesized key electrical system parameter: the air gap impedance (or sliding interfacial impedance). This parameter represents a large increase (100- 1000%) in overall impedance observed when a finger is sliding versus

when it is stationary which cannot be explained by other electrical impedance measures and which vanishes again should the finger come to rest.

Finally, I report on an extremely high bandwidth electroadhesive approach to controlling friction forces on sliding fingertips which is capable of producing vibrations across an exceedingly broad range of tactile, audible, and ultrasonic frequencies. Vibrations on the skin can be felt directly, and vibrations in the air can be heard emanating from the finger. Additionally, I present evidence of how the interfacial air gap voltage is primarily responsible for the induced electrostatic attraction force underlying the electroadhesion effect. I develop an experimental apparatus capable of recording friction forces up to a frequency of 6 kHz, and use it to characterize my two electroadhesive systems, both of which exhibit flat current-to-force magnitude responses throughout the measurement range. These systems use custom electrical hardware to modulate a high frequency current and apply surprisingly low distortion, broadband forces to the skin. Recordings of skin vibrations with a laser Doppler vibrometer demonstrate the tactile capabilities of the system, while recordings of vibrations in the air with a MEMS microphone quantify the audible response and reveal the existence of ultrasonic forces applied to the skin via electronic friction modulation.

Acknowledgements

I would like to acknowledge and thank Ed Colgate and Michael Peshkin for their guidance and encouragement throughout my time at Northwestern. They have been exemplary academic and professional role models, and I cannot imagine achieving the same high standard of research without their weekly support and feedback. They made navigating the waters of academic and engineering achievement seem effortless.

In that same vein, I'd like to thank all members and faculty of the NxR lab for their social and academic support during my time, and especially those of the surface haptics research group, including Michael W, David, Becca, Steven, Philip, Roman, Heng, and others. I will forever cherish times spent around the lunch table and Friday afternoon happy hours. I especially appreciate Joe Mullenbach for his initial guidance, and then wonderful continued collaboration and encouragement on various high impact projects in the lab, such at the TPad Tablet project and TPad Phone.

I'd like to thank my parents, Dr. Thomas Shultz and Julie Shultz, for their continual support of their youngest child. I no doubt received my inquisitiveness and confidence from their parenting efforts, and look forward to passing these traits on. I'd also like to thank my siblings Jennifer, Jessica, Kevin, and Kent for their encouragement.

Finally, I would like to acknowledge and thank my loving wife Becca. She has been a continual source of strength and support since before my application to graduate school, and I can't wait to see what's in store for us in the future.

Preface

The material presented here has been either published or submitted for review and publication at various haptics conferences and journals. Approximately half of it is already in a form which may reach the wider research community, and I look forward to presenting the rest here, and in associated publications.

Though it is compiled in this dissertation as a single linear work, it has taken place over many years of parallel exploration, discovery, trial and error, and careful planning. I viewed this as one of the challenges of entering a new research area in which norms have yet to be established and in which the foundational principles of the field have yet to be widely understood and disseminated. There is much reward to be gained for pushing the boundaries of the field forward, however, for every success presented here, there were probably a handful of failures, false starts, and misunderstandings. There were attempts that probably seem absurd in retrospect (i.e. boiling aluminum, which worked, or applying salt water to finely polished sanding stones, which didn't), and yet, at the same time were most likely pivotal to my understanding.

I say this simply to encourage those who may follow this line of research (or at least concern themselves with following this dissertation). The path to understanding is not always as straightforward as it seems, and do not discount the experience of others along the way, whether they be accounts from an inventor nearly 150 years ago, or comments made by colleagues struggling with similar problems today.

Table of Contents

List of Figures

of the modulation envelope. Distortion products are minimal in the case of the 3M coated surface with envelope correction applied.   94

CHAPTER 1

Introduction

The work presented here is part of a larger research program called surface haptics. Surface haptics research asks the following question: *how might one go about controlling the complex mechanical interactions between human fingertips and physical surfaces?*

One popular answer to this question is based on varying the friction force (the lateral resistance to motion) of fingertips as they move on smooth surfaces. These so-called variable friction displays are typically co-located with a visual display, and finger position is tracked by the system. The friction of the surface is then programmed to vary due to finger position, finger velocity, time, or any number of variables to produce complex tactile effects as feedback to the user. One reason variable friction displays have come to receive considerable interest is because they can be seamlessly integrated into existing direct-touch user interfaces (e g. tablets and smartphones).

When operated at steady state, variable friction displays are able to arrest the motion of a sliding finger, or to reduce friction to a near negligible level. These effects are achieved by applying additional Coulombic force, which increases friction [2] [3], or by altering the skin/surface interface via low amplitude, ultrasonic oscillations [4] [5], which decreases friction. These effects can also be combined for greater dynamic range [6]. These types of displays have seen a wide variety of applications such as: increasing the physicality of touch interaction [7], influencing shape perception [8], rendering high fidelity textures [9], communicating emotion between partners [10], aiding the blind in navigation [11], and

even turning everyday objects into expressive interactive surfaces [12]. With such a wide array of applications in mind, and with such seamless integration into existing interactions, these devices show great promise for the future of haptic interaction design. Indeed, I spent a considerable amount of time at Northwestern creating and integrating these types of displays into Android phones, tablets, and smartwatches as part of the TPad Tablet Project, and into a high-performance PC based audio-visual-tactile platform called Tactile Soundboard (documented in Appendix A).

While many early variable friction displays were based on the ultrasonic TPaD described by Winfield et al. in 2007 [4], at the beginning of my research comparatively little had been explored in the area of electrostatic displays since their modern introduction by Linjama et al. [2] and Bau et al. [3]. However, since electrostatic displays are inherently solid state and low power, two large practical advantages when compared to resonant ultrasonic devices, they have quickly begun to garner greater attention from various research groups [3] [13] [14] [15] [16] [17] [18], and from commercial industry. Despite this fact, the underlying principle of electroadhesion, or electrovibration as it is sometimes called in the literature, is not well understood in the context of fingertips, and principles for exploiting the effect have not been analyzed or established.

As a starting point for my research, a variety of groups had used perceptual and/or force measurements in an attempt to characterize displays [3] [13] [18]. However, since the forces and effects were so small, what was usually asked was *how might any force or perception be generated at all?* Typically, an ac voltage was input to the electroadhesive system, and the resulting force or perceptual output was measured, with a very rough theoretical model linking the two. These approaches many times lacked empirical

measurements of parameters for the systems in question, and usually relied heavily on values pulled from the literature to approximately map applied voltage input to recorded force and perceptual output. The results from these tenuous mappings many times led to overly general conclusions being made, or conclusions that were at odds with other reports. While essential for evaluating the capabilities of existing hardware, I saw this 'black box' or perhaps 'top-down' type approach as ultimately limiting in terms of designing and optimizing new electroadhesive systems. It gave a sense of why these specific systems and manners of excitation *might* work, but didn't give any insight as to what the electroadhesive effect might be capable of and, more interestingly, how it might be *exploited*.

Instead, what I thought was needed was a 'bottom-up' approach. Something that would let me crack open the black box a bit, and start to predict what types of systems and excitation methods I might need in order to get the specific high performance characteristics different applications desire. What this different approach led to is a unifying model that attempted to explain various electroadhesive based observations, and, at the same time, offer effective parameterization techniques and metrics for optimization (some of which have already been used successfully in other research endeavors [**19**]). To summarize, at the beginning of my research I asked these two questions:

(1) What is the direct origin of the transduction from an electrical voltage to a mechanical force in these finger based systems, i.e. what voltage (or charge) and where, creates an effective increase in frictional force?

(2) What factors affect how an applied voltage (or current) by some external source results in this effective voltage?

What follows is my attempt at answering these questions, and some interesting observations and example systems that became apparent directly as a result of my increased understanding of the subject. An outline of the rest of the dissertation is given below.

In **Chapter 2** I summarize the related work in the field at the time of my first investigation as it relates to the dissertation as a whole. As this was a relatively small field at the time, this chapter is brief. There are, however, notations to other related works within each chapter as they become relevant.

In **Chapter 3** I set about answering the first question above about the origin of the electroadhesive effect. The search for this answer took me deep into the history of the effect, and I rediscovered the free charge effects (DC) of electroadhesion, desribed at the turn of the the 20th century. Work which originated during this time postulated the existence of an interfacial gap between slabs of metal and stone, which was where the electrical to mechanical transduction took place. I summarize and extend these reports to finger based devices, and setup a lumped parameter series model as a basis for further research.

In **Chapter 4** I develop an electrical analysis technique which allowed me to inspect various qualitative and quantitative aspects of the electroadhesive system both in isolation, and as a whole. I tried to approach this work with a high level of scientific rigor in order to both communicate my results effectively, and establish a common set of measurements that may be used in the future for different types of displays, and across different research groups. I also wanted to leave little doubt to the over-arching conclusion that I was quickly reaching, the so-called gap impedance appeared to play an extremely pivotal role in electroadhesion, but is hardly even mentioned in the haptic research literature.

It is in this chapter that I hope to rectify what appears to be a large oversight by the community.

In **Chapter 5** I attempt to show the benefit that comes with this larger understanding of the electroadhesive phenomenon, and how these various system parameters may be exploited. I, once again, punctuate the importance of the gap impedance, and its effects on the applied force profiles to the finger. In addition, I show direct evidence of the widest bandwidth of variable friction forces to ever be applied to the skin, and demonstrate the incredible fidelity with which these systems can apply known force spectra to the skin. I finish this chapter by discussing how this technique may be used in the future to apply relatively well known force signals to the finger, which may allow for better mechanical characterization of variable friction systems.

Finally, in **Chapter 6**, I summarize the main findings of my work, and outline some areas of future work. These mainly include utilization of electroadhesion for high fidelity texture display, fingertip mechanical characterization, further investigation as to the origin of the gap impedance, specifically as it pertains to frustrated total internal refraction (FTIR) measurements of real area of contact, and the development of multimodal touch-screen interfaces.

Appendix A documents an example of a high performance audio-visual-tactile interface called Tactile Soundboard, which I have demonstrated, but never detailed before.

Appendix B contains a technical discussion of the design and construction of the wide-bandwidth transconductance amplifier used throughout my research, including full schematics and a bill-of-materials (BOM) for off the shelf parts.

CHAPTER 2

Related Work

Observations of electroadhesion have been recorded for over 140 years. Throughout the late 19th and 20th centuries the effect intrigued scientists and engineers, causing tactile vibrations and sounds to be emitted via their fingertips, almost as if by magic [20] [21] [22] [23]. Modern day application of this effect, however, has so far been limited. It has been used for semiconductor wafer chucking [24], for industrial material handling and robotic gripping [25] [26], as a tactile display technology for the visually impaired [27] [28], and, most recently, as a visuo-tactile display technology for general tablet and smartphone type interactions [2] [3].

Below I highlight some of these historical examples of electroadhesion first, and then detail more of the modern day related work and theories of operation.

2.1. Early Examples of Electroadhesion

Almost entirely forgotten throughout the last century and uncovered during the course of my research, the acoustic-tactile electroadhesive effect was first discovered in 1873 by the famous Chicago area inventor Elisha Gray when he observed sound emanating from his nephew's finger as it was run along the surface of an electrified tin bathtub, Fig. 2.1.

At first, it was speculated that the induced vibration may have been from the actuation of the nervous system actively twitching the finger, or due to sparks being discharged in the gap between the finger and surface, but these hypotheses were quickly thrown out after

Figure 2.1. First documented discovery of electroadhesion (1873). Public domain image reproduced from [**1**].

further testing. Gray noted that the sound and vibration stopped if his finger stopped, or if the interface was wetted, and appeared to quickly come to the conclusion that the effect was do to an intermittent increase in friction between the finger and surface.

In fact, even at this early stage in the development of electromagnetic theory (Maxwell published his full list of equations that same year), Gray suspected that the friction force

was similar in nature to the electrostatic force which develops between the plates of a condenser (the early name for a capacitor). In fact, Gray appears to have gotten many of the intuitive and qualitative aspects of the electroadhesive effect correct, even if he was unable to describe his system mathematically, or precisely control the effect.

Gray used the acoustic-tactile electroadhesive effect in a patent for the harmonic transmission of musical tones [20], and the effect has even been said to have led to his idea and patent application for the modern telephone on the same exact day as Alexander Graham Bell in 1876. This was only a few years after the discovery of electroadhesion ignited his imagination [1].

Markedly less famous than the telephone, another of Gray's early inventions was an electroadhesion powered violin, seen in Fig 2.2, which had its strings replaced with a conductive plate. As Gray rubbed the plate, a pitch matching that of the alternating induction coil electrical source was heard. The vibration also excited the natural resonances of the violin, imbuing the sound with the instrument's timbre.

Gray's curious audio-tactile effect wasn't investigated again until 1917, when two Danish scientists, Johnsen and Rahbek, studied the effect in great detail. They also demonstrated a "speaking violin," where the body of a violin was used as a resonant mechanical amplifier for the reproduction of music and speech [21]. Sounds played through the apparatus had their natural qualities preserved, though they were once again transformed by the violin's unique timbre. Further discussion of Johnsen and Rahbek's work is discussed in Chapter 3, as they are also known for a DC version of the electroadhesive effect

Figure 2.2. One of the first demonstrations of an audio-tactile display using electroadhesion (1874). Public domain image reproduced from [1].

which shares their name. Gray, Johnsen, and Rahbek envisioned wide-ranging applications for their audio reproduction technology, but over the past century their techniques have largely been forgotten and usurped by more practical coil based techniques.

2.2. Modern 'Electrovibration' Research

In contrast to these historical examples, the line of research at the beginning of my studies concerning electrostatic variable friction displays dates back to 1950 when Mallinckrodt, by accident, noted that a certain brass electric light socket no longer felt smooth when the light was turned on [22]. As it turned out, the socket housing was connected to a live power wire, and current was flowing through the finger/surface interface. Using both bare and insulated aluminum plates, along with a 60Hz, 110V excitation, it

was determined that an intermittent increase in friction was what created this peculiar resin-like feeling and faint 120Hz audible tone. It was theorized that either the outer keratin layer of skin or the varnish insulating layer acted as the dielectric of a capacitor. When voltage was applied, force developed between the capacitor plates, which were the metallic surface and inner conducive fluids in the skin.

This AC effect was later given the name electrovibration and studied in more detail by Grimnes, who, again, used both bare and insulating surfaces [23]. Grimnes also noted that surface roughness seemed to have a certain effect, and the electrovibration intensity seemed to increase with the dryness of the skin. Measurements of the current flowing in the skin were in the μA range, much below the traditional electro-cutaneous sensation limit of approximately 1 mA.

Strong and Troxel were the first to use this electrovibration effect as a tactile display, forming an electrode pin array which could be independently excited with pulsed waveforms [27]. They also put forward the first mathematical model based on the previous capacitor plate explanation. Their model is given below:

(2.2.1)
$$F_e = \frac{A\varepsilon_0 V_t^2}{2(\frac{d_d}{\varepsilon_d} + \frac{d_s}{\varepsilon_s})^2}$$

In this equation, the electrostatic normal force on the finger (F_e) is given in terms of the relevant area of contact (A), the permittivity of free space (ε_0), the total applied voltage between the electrode and ground (V_t), the thickness of the outer layer of skin (d_s) and dielectric insulating layer (d_d), and the relative permittivities of the skin (ε_s) and dielectric (ε_d) layers.

More recently, Beebe et al. developed a polyimide-on-silicon version of Strong and Troxel's tactile display [28], which was later used in tests with the visually impaired [29]. Little was mentioned, however, as to the underlying principle of the electrostatic effect. Psychophysical measurements of this type of display have included voltage detection thresholds in relation to dielectric layer thickness [30] and the polarity of the pulsed excitation waveforms [31].

The first systematic force measurements, however, were made by Meyer et al. [13], who recorded both normal and friction (lateral) forces as a subject's finger was driven across a commercially available surface capacitive touch screen (3M MicroTouch). This was the same type of device used in Disney Research's TeslaTouch studies [3], [11], [8]. Using tribological methods, Meyer was able to infer the magnitude of additional normal force created when an AC excitation voltage was applied across the skin/surface interface. The general square law of the inferred normal force as a function of applied voltage was verified across several subjects, but the theoretical model used to describe the frequency dependence of the force seemed to be at odds with other recorded data. A conclusion of that work was that a more detailed electrical model of the finger/surface system was needed in order to accurately predict the electrostatically induced force. This more nuanced model, based on work done on electrostatic chucking devices, is presented in the next chapter.

CHAPTER 3

Large DC Electroadhesion Forces - Expanding Electrovibration

At the beginning of my research, most, if not all, electroadhesive displays utilized purely AC excitation waveforms for their operation. This was an artifact of the history of the electrovibration effect as a display technology. In short, the effect was so limited early on, that only the vibratory frequencies in the peak tactile range were noted to work well. This early constraint, however, seemed to be at odds with decades old research from the electrostatic chucking industry which seemed to suggest powerful DC forces should be able to be produced as well. Why wasn't I seeing this when it came to human fingers? Why couldn't 'electrovibration' displays generate low-frequency or DC forces? Was there something fundamental here I was missing? If so, how could I hope to understand the origin of electrical to mechanical transduction? These questions led to my investigation and attempt to rectify these two parallel lines of research with each other, and to see if I could, in fact, produce large DC electroadhesive forces using a sliding finger. I began from the start of the electrostatic chucking research: the so-called Johnsen-Rahbek Effect.

3.1. Johnsen and Rahbek's Effect

The term electroadhesion is drawn from the 1923 work of Danish scientists Alfred Johnsen and Knud Rahbek [21]. Working with polished lithographic stone and metal surfaces, this term was used to describe the physical phenomenon of considerable adhesion

which developed when the highly resistive stone was placed on top of a metal plate and a high voltage was applied between them.

Interestingly, Johnsen and Rahbek also reported the use of electrostatic attractive forces on human fingertips some 40 years after Elisha Gray and some 30 years before the first report by Mallinckrodt. They even noted several key aspects of electrovibration, for instance, that force does not exist at DC with a completely insulating layer. They mentioned a previous design of the technology by a separate American inventor which employed a thin mica dielectric, but explained that, at DC, charge would quickly accumulate on the surface of the insulator and cancel any electroadhesive effect.

They also mentioned that a faint tone twice the excitation frequency was heard as the finger moved along the surface. The majority of their work, however, was focused on the DC version of the electroadhesive effect, as it was a highly intensified version of the AC effect. When the term Johnsen-Rahbek effect is used in literature, it solely refers to intensified electroadhesion with DC excitation.

3.2. An Explanation and its Development

An in-depth explanation of the Johnsen-Rahbek effect is beyond the scope of this dissertation, but a basic explanation is as follows. First, imagine a finely polished slab of semi-conductive material placed on top of a similarly smooth metallic plate (as seen in Fig 3.1a). Since the surface of the plate and the surface of the semi-conductor are highly polished, it would appear that the two materials are in intimate contact across their entire interface. However, due to the presence of microscopic asperities on the surface of each material (generally on the scale of microns), the area where the two surfaces come into
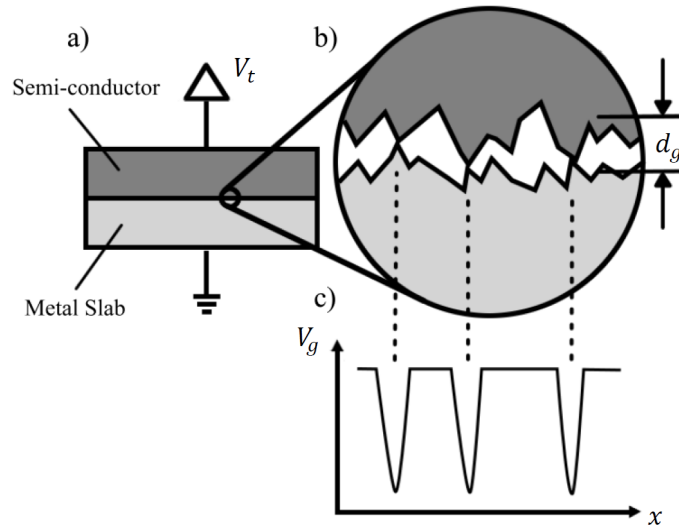
Figure 3.1. a) General setup of Johnsen Rahbek devices b) Close up the contacting surfaces and the interface gap. Asperities keep the surfaces separated by approximately d_g c) Voltage across the gap,V_g plotted as a function of position. The voltage drops to zero at asperity contact points,but remains high elsewhere.

real contact is a small fraction of the total apparent area of contact. There is, therefore, a non-uniform gap at the interface of the two surfaces (Fig 3.1b). This gap thickness is on the order of the average surface roughness of the two materials [32]. The gap is also composed primarily of air, as only a small set of highly resistive asperities from the slab of semi-conductor come into contact with the metal surface.

Next, imagine a constant voltage source is attached between the metallic plate and the non-contacting surface of the semi-conductor. Charge will make its way through the slab of semi-conductor and towards the gap at the interface, where it will then become constricted by the limited points of contact with the metal surface. It is this constricting geometry that can, in general, lead to high contact resistances between flat surfaces [33],

these small points of contact will be the only place that the voltage drops to zero (Fig 3.1c).

The majority of the interface, therefore, will have a very large voltage (though usually somewhat lower than the total applied voltage) across a gap that is only microns thick. Now, due to the fact that force on the plates of a parallel plate capacitor is inversely proportional to the square of the plate separation, the force across the air gap at the interface can be surprisingly large, with one researcher recording a measured adhesive pressure of nearly 10 N/cm2 at a total applied voltage of 100V [34], and estimated gap voltage of 40V [35].

The explanation given above matches closely with the original one given by Johnsen and Rahbek in 1923, which has since been further investigated and validated. In 1950, Balakrishnan repeated the results of Johnsen and Rahbek, but instead used various magnesium and titanium oxides to get rid of the humidity dependence of the original devices [36]. Soon after, Stuckes further polished the metal surface to achieve nearly four times higher adhesive forces. She also put forward the idea of constricting resistance points at the interface, and an electrical circuit model to make sense of the data [34]. This approach was subsequently taken further by Atkinson, who incorporated Stuckes' initial explanations into a model that predicted anomalies in Stuckes' data at higher voltages [35].

Little additional progress was reported in the literature until Watanabe's creation and investigation of modern day electrostatic chucks with doped alumina [37]. Further work by Kanno [38], [39] and Qin and McTeer [40] combined the previous models into an electrical circuits based equivalent model, which is the basis of the model described here.

I will briefly overview this model in the context of electrostatic chucks before applying it to human fingers.

3.3. Johnsen-Rahbek Force Model

The force model for electrostatic chucks begins with the description of two electrically relevant layers. The first layer consists of the bulk of the semi-conductor material, which, in the literature, has been called the dielectric layer. This name is leftover from purely AC electrostatic chucks, where this layer is a pure dielectric with essentially infinite resistivity. In the context of Johnsen-Rahbek, however, the dielectric can be said to be leaky, that is, it has a finite resistivity that allows charges to pass through it. The second electrical layer consists of the dielectric/metal surface gap. As stated above, this layer consists mostly of a thin layer of air, with a small set of resistive asperities. The model then follows from two simple assertions.

First, the only relevant force in the system is that which develops across the thin gap of air at the interface:

$$(3.3.1) \qquad F_e = \frac{A\varepsilon_0\varepsilon_g}{2}\left(\frac{V_g}{d_g}\right)^2$$

Equation 3.3.1 is simply the standard equation for force on an air filled parallel plate capacitor in terms of the gap separation (d_g), relative gap permittivity (ε_g), permittivity of free space (ε_0), area (A), and gap voltage (V_g). Note that the relevant area of the gap technically includes only the non-contact air gap sections, however, since the real area of contact is typically much smaller than the overall apparent area of contact, the latter is used in most contexts. To get a feel for this equation, consider a gap voltage of $V_g = 100V$,

a gap thickness of $d_g = 1\mu m$, and a relative permittivity of $\varepsilon_g = 1$ (air), which would yield a predicted electrostatic pressure of 4.4 N/cm^2.

In reality, however, for a total applied voltage of 100V, the actual voltage across the gap will be somewhat lower. This is because of the model's second stipulation, which is that the gap voltage (V_g) is an attenuated version of the total applied voltage across the dielectric and gap system. If I model the system as two resistances in series, this is simply a resistive divider:

$$(3.3.2) \qquad\qquad V_g = V_t \frac{R_g}{R_d + R_g}$$

R_g is the previously mentioned gap contact resistance, and R_d is the bulk resistance of the dielectric layer. Taken together, 3.3.2 and 3.3.1 lead to:

$$(3.3.3) \qquad\qquad F_e = \frac{A\varepsilon_0\varepsilon_g}{2} \left(\frac{V_t}{d_g} * \frac{R_g}{R_d + R_g} \right)^2$$

From this equation, it can be seen that, in order to achieve the maximum force possible for a given voltage, I must ensure $R_g \gg R_d$, that is, have a contact resistance that is much higher than the dielectric resistance. Additionally d_g should be minimized, that is, contacting surfaces should be quite smooth. It is with this model in mind that I set out to find a suitable surface for finger-based electroadhesive devices.

3.4. Material and Model

I investigated many materials in an effort to find an appropriate surface for DC electroadhesion and human fingertips. As described in the original Johnsen and Rahbek paper, electroadhesion can be achieved with a bare metal plate and human fingers, as

the outer layer of the skin can act as a somewhat resistive dielectric. Due to the variable nature of human skin, however, I soon discovered that it is advantageous for practical devices to have a surface coating on top of the bare metal plate. Furthermore, surface coatings need to offer high electrical resistivity, have minimal roughness, achieve excellent coating conformity, and ideally be easy to create or acquire. One material that fits these requirements, and has been found to offer good electroadhesive capabilities, is anodized aluminum. Indeed, similar doped alumina electrostatic chucks have been shown to have good DC electroadhesive properties [**41**], and anodized aluminum was used recently in electrovibration [**12**] for an AC electroadhesive effect. For my tests, I used 6061 anodized aluminum.

Another important factor in designing the electroadhesive system is the excitation source. I chose to use a current control amplifier, specifically a Trek model 610C high-voltage capable amplifier. This amplifier has a trans-conductance mode that allows the user to control an output current given an input voltage. The chief benefit of current controlled excitation is safety. Current was limited to no more than 100μA in my tests. Voltage was also limited to under 1kV. As noted in [**12**], these currents and voltages are much less than those experienced with static shocks occurring in day-to-day life, and they pose no known health concerns.

With a different system setup and excitation from traditional electrostatic chucks (Fig 3.2a), I must now also edit 3.3.3 to represent the skin/anodized aluminum system (Fig 3.2b). First, I can add in the additional skin layer to the resistor divider term:
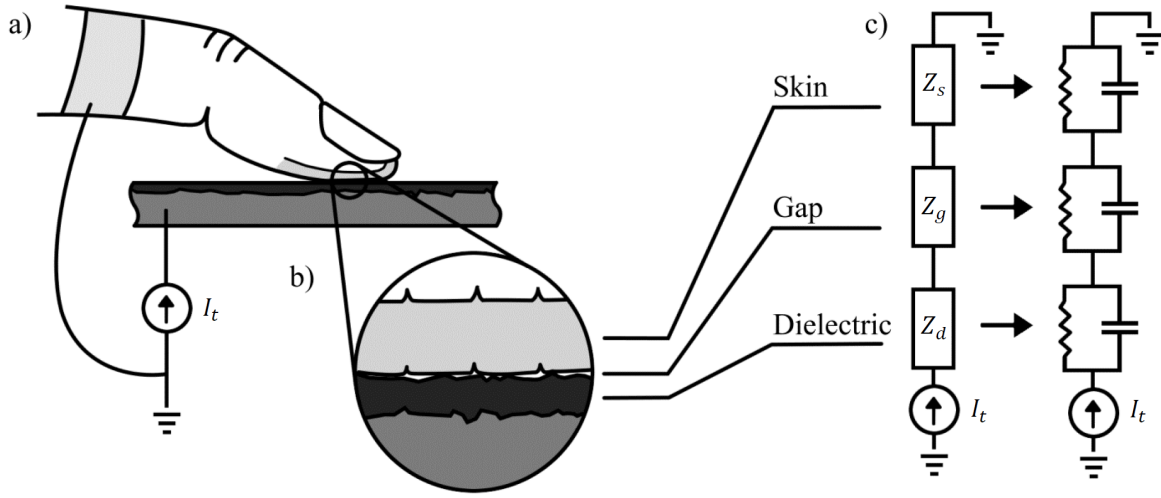
Figure 3.2. a) Overview of entire electrical system b) Detail of the skin/anodized aluminum interface, showing approximate geometry (not to scale) of the 3 electrical layers c) Generalized system impedance model, and equivalent RC impedance model. Model assumes force develops across Z_g .

$$(3.4.1) \qquad F_e = \frac{A\varepsilon_0\varepsilon_g}{2}\left(\frac{V_t}{d_g} * \frac{R_g}{R_d + R_g + R_s}\right)^2$$

Where R_d now represents the bulk resistance of the anodization layer (previously the dielectric layer), R_s represents the bulk resitance due to the outer layer of the skin, and R_g represents the constriction resistance of the gap interface. Furthermore, if it is noted that:

$$(3.4.2) \qquad V_t = I_t R_t = I_t(R_d + R_g + R_s)$$

I can combine 3.4.1 and 3.4.2 to yield the governing equation for my system at DC:

$$(3.4.3) \qquad F_e = \frac{A\varepsilon_0\varepsilon_g}{2}\left(\frac{I_t R_g}{d_g}\right)^2$$

Here it can be seen that for a current controlled excitation, the force on the skin depends not on the entire system as shown by 3.4.1, but only on the constriction resistance of the skin/surface interface. A similar effect has been noted before with electrovibration devices, at it can lead to more consistent forces across multiple skin/surface interfaces [**12**]. Equation 3.4.3 helps explain why this is the case. I will return to a generalized form of this equation later in Chapter 5.

3.5. Parameter Estimation

Though 3.4.1 or 3.4.3 are relatively simple, the parameter values are non-trivial to calculate. For A, I ensured a constant area by using a $150\mu m$ thick, electrically insulating plastic disc inserted between my finger and the anodized aluminum. The disc was 12.5mm in diameter and had a 6.4mm diameter hole in the center of it which allowed my finger to electrically contact the anodized aluminum with an area of $32.17mm^2$. Relative permittivity of the gap is assumed to be that of air, close to 1.

To estimate R_g, I used a method similar to [**38**]. I first measured the total system resistance R_t by recording the applied current and resulting voltage during normal finger exploration. This was done via current and voltage monitor connections provided by the amplifier. I then measured the total system resistance with the contact resistance shorted out, (i.e.$R_g + R_s$) by placing conductive silver paste between the finger and the anodized aluminum. This conductive silver paste essentially causes R_g to go to zero, as it fills the gap interface, ensuring intimate electrical contact. This measurement was made immediately after force data was taken. I then subtracted $R_d + R_s$ from R_t to give an estimation of the contact resistance R_g. It is important to note that this estimate is prone

to error, as it is well known that DC skin impedance can vary due to a wide variety of factors [42], [43], and because the skin/surface interface can change with the addition of sweat or oils dirtying the surface. Further investigation in this area is undertaken in Chapter 4. Nonetheless, by measuring resistances during and immediately after exploration, I estimated a contact resistance of approximately $7M\Omega$.

A measurement of the anodized aluminum surface roughness was made using a Zygo 3D optical surface profilometer. The average roughness was $0.34\mu m$. A similar measurement of an alginate cast made of a finger pressing against a hard surface was made, but, as the distribution of surface heights was highly non-Gaussian, a single roughness parameter for the skin was difficult to compute. Numbers for this value in the literature are typically on the order of $20\mu m$ [44], yet data taken on my casts seem to indicate typical roughness below $5\mu m$. This may be because the skin is flattened out under applied pressure. Further investigation as to the value of the d_g parameter is needed. I can, however, conclude that, of the two contacting surfaces, the skin appears to be rougher than the anodized aluminum.

3.6. Force Measurement

Using a tribometer similar to Meyer et al. [9], and seen in Fig. 3.3, I measured normal force and lateral force as the I explored the surface with my index finger. Normal force was measured using two strain gauge based load cells, while lateral force was measured using a piezoelectric load cell. I swiped left and right across the surface, using a metronome to maintain a speed of approximately 10cm/s. The excitation used to approximate DC was a 0.1Hz square wave, alternating between $0\text{-}100\mu A$. Accordingly, the total voltage
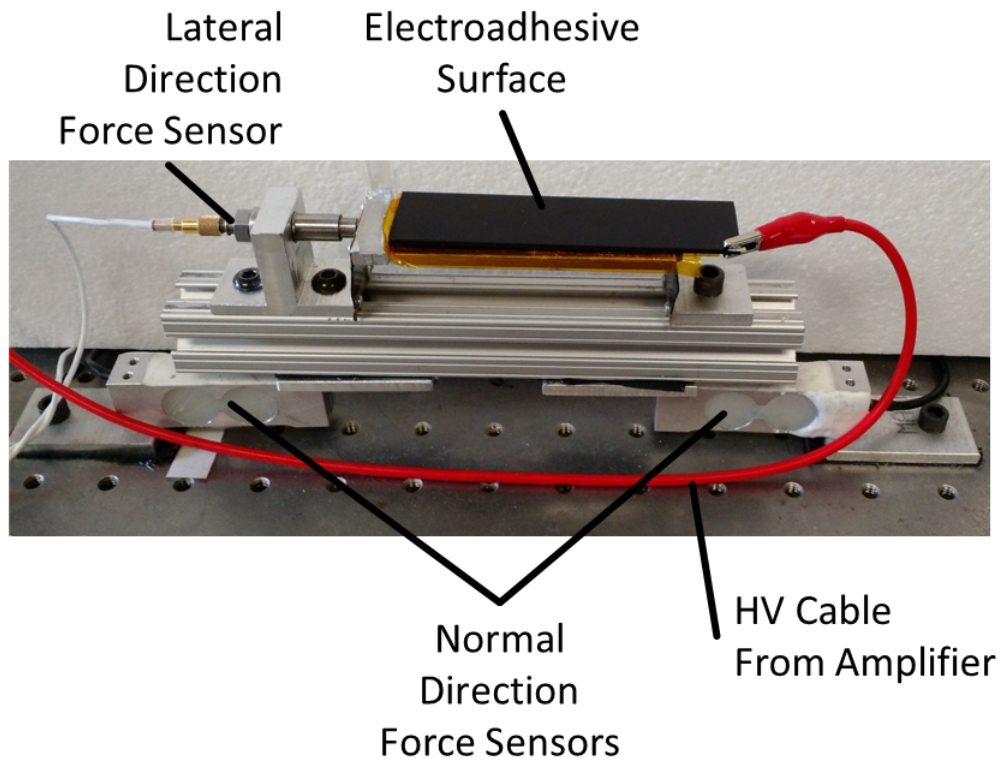
Figure 3.3. Picture of the tribometer and electroadhesive surface used to collect normal and lateral force data.

applied across the 8MΩ system impedance was approximately 800V. I observed that over the course of several minutes of use the electroadhesive effect would become significantly stronger and then stabilize. This is possibly due to drying of the skin, which would, in turn, increase the gap resistance. Because of this, data was taken over the course of 500 seconds, and the first 250 seconds were excluded. An example plot of the data recorded can be seen in Fig 3.4. Each point on the graph represents the average of a single swipe left or right over the 250 seconds. Linear functions were fit to each set of data (current on and off).
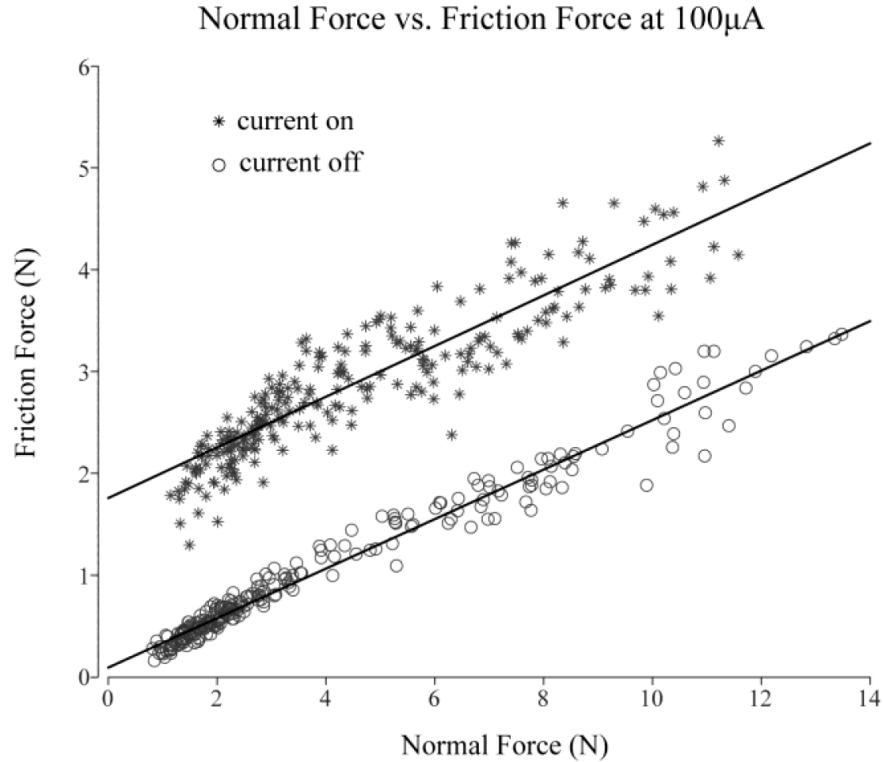
Figure 3.4. A friction force of 2.5N corresponds to a normal force of 3N with the current on, and 10N with the current off. The difference in normal force, 7N, is assumed to be the additional electroadhesive force.

From these data, I can estimate the additional normal force due to electroadhesion, in much the same manner as Meyer et al. [13]. Seen is an additional electrostatic normal force of approximately 7N. Using (7) and my parameter measurements, this corresponds to an effective gap thickness of 3μm. As mentioned above, this would seem to indicate that the skin is deformed under the applied pressure, similar to the behavior reported in electrostatic chucks [39].

3.7. Frequency Extension of Force Model

Up until this point in the discussion I have treated only the DC case, allowing me to model the layers as pure resistors. While this is a safe assumption for large timescales, it must be lifted if I am to extend the model to AC electroadhesion (i.e. electrovibration). To generalize, I model the impedance of each electrical layer as a resistor in parallel with a capacitor:

$$(3.7.1) \qquad Z_x(\omega) = \frac{R_x}{1 + j\omega R_x C_x}, \ x = d, g, s$$

Where x denotes the dielectric, gap, or skin impedance layer respectively (see Fig 3.2c). Replacing the resistor divider in 3.4.1 with an impedance divider, a generalized equation for force as a function of frequency is obtained:

$$(3.7.2) \qquad |F_e(\omega)| = \frac{A\varepsilon_0\varepsilon_g}{2} \left(\frac{V_t}{d_g} * \frac{|Z_g(\omega)|}{|Z_d(\omega) + Z_g(\omega) + Z_s(\omega)|} \right)^2$$

Equation 3.7.2 is, therefore, the proposed generalized force equation that extends a model of DC electroadhesion into the AC regime. This result may be compared to both Johnsen-Rahbek and electrovibration models by examining the impedance divider term at both low frequencies ($\omega \to 0$) and high frequencies ($\omega \to \infty$).

3.8. Model at Frequency Extremes

Looking at equation 3.7.1, note that, for low frequencies, Z_x reverts back to R_x, and the impedance divider term turns into a resistor divider as seen in equation 3.4.1. It is also interesting to note that equation 3.4.1 also explains why traditional electrovibration devices will not work with DC excitation. If R_d is allowed to go towards infinity (by using

a perfectly insulating dielectric) the model predicts the steady state electroadhesive force will go to zero. This prediction aligns well with reports given in the background literature above, which state that charge will leak across the interface gap and collect on the surface of the insulator, negating adhesive effects. During this leakage transient, however, force may still be generated.

Looking instead at 3.7.1 at high frequencies ($\omega \to \infty$), the capacitor dominates over the resistor, and the impedance is $1/j\omega C_x$. The impedance ratio then becomes a capacitive divider and 3.7.2 turns into:

$$(3.8.1) \qquad F_e = \frac{A\varepsilon_0\varepsilon_g}{2}\left(\frac{V_t}{d_g}\frac{C_dC_s}{C_gC_d + C_gC_s + C_dC_s}\right)^2$$

With a few simplifying assumptions, equation 3.8.1 can be put into a more familiar form. First, I can replace each capacitance term with the general capacitor equation $C_x = \frac{A\varepsilon_0\varepsilon_x}{d_x}$, and then perform some algebra to produce:

$$(3.8.2) \qquad F_e = \frac{A\varepsilon_0 V_t^2}{2\varepsilon_g\left(\frac{d_d}{\varepsilon_d} + \frac{d_s}{\varepsilon_s} + \frac{d_g}{\varepsilon_g}\right)^2}$$

If I assume $\varepsilon_g = 1$ (for air), equation 3.8.2 takes the form of equations 2.2.1 proposed by Strong and Troxel with the addition of a d_g term. I have therefore shown that, by modeling each electrical layer as a resistor and capacitor in parallel, I can extend force models from the Johnsen-Rahbek effect literature to incorporate dynamic electroadhesive effects.

	$R_d \to \infty$	$R_d \neq \infty$
$\omega \to 0$	$F_e = 0$	$F_e = \dfrac{A\varepsilon_0\varepsilon_g}{2}\left(\dfrac{V_t}{d_g}\dfrac{R_g}{R_d + R_s + R_g}\right)^2$
$\omega \to \infty$	$F_e = \dfrac{A\varepsilon_0\varepsilon_g}{2}\left(\dfrac{V_t}{d_g}\dfrac{C_dC_s}{C_gC_d + C_gC_s + C_dC_s}\right)^2$	

Figure 3.5. Summary of Impedance Force Model at Extremes

A summary of this explanation is shown in Fig. 3.5. This explains how one overarching model can take on the forms described in the various literature background depending on two assumptions, if the dielectric layer is leaky or not, or if the frequency is close to zero or sufficiently high to in a purely capacitive regime. As a final note, it is incorrect to assume that most 'electrovibration' devices are truly in this latter category (purely capacitive), and I argue that this is, indeed, a fact that has been overlooked by the majority of haptics researchers. The frequency of actuation, ω, is typically neither zero nor essentially infinite, therefore generalized equation 3.7.2 must be relied on, unless the system has been explicitly characterized (as I do in Chapter 4).

3.9. Chapter Summary

By unifying Johnsen-Rahbek and electrovibration force models, it can now be seen that both stem from the same underlying mechanism: Coulombic attraction across a very small air gap. *The Johnsen-Rahbek effect typically means DC electroadhesion, while electrovibration refers to the purely AC version, but the fundamental difference between the two is academic.* It is with this explanation that I hope to clarify the underlying principle of electrovibration, and offer some additional implications going forward.

First, the model predicts a theoretical maximum electrostatic force for a given gap geometry and voltage, as expressed in equation 3.3.1. This equation is encouraging for the future of electroadhesive displays, as it implies that considerably high normal forces can be applied to bare skin for only milliwatts of electrical power.

Second, this maximum force will never be able to be attained, as there will always be an attenuation ratio of $\frac{|Z_g(\omega)|}{|Z_t(\omega)|}$ for voltage controlled setups. This effect can somewhat be mitigated by utilizing current control, but the maximum force will nonetheless fall off with $|Z_g(\omega)|$, as will be shown later in this thesis.

Because these electrical impedance effects can come to dominate the overall force equation, I deemed it vital that further investigation into the nature of the electroadhesive force make an effort to characterize the system as a whole, including the relevant properties of the skin/surface interface. It is this detailed characterization that was most likely missing from the data presented in [13]. In that work, it was observed that the force seemed to follow a fractional-order model with frequency. This behavior could be due to the dispersive nature of human skin, which is well documented in the literature [45], and has since been applied to electrovibration [18], or due to other series impedance mechanisms such as improver system grounding, or the series resistance of the conductive layer. Therefore, only with a proper measurement of the relevant system impedances in 3.7.2 can the correct magnitude of the force as it evolves with frequency be calculated.

The effectiveness of this approach is born out in Chapter 4 and Chapter 5, as I found two different electroadhesive surfaces to perform this detailed electrical impedance analysis on, and applied the knowledge gained from careful characterization back to the system in order to engineer incredibly high bandwidth performance.

CHAPTER 4

Electrical Characterization - Existence of Gap

With the first question of my research (what is the origin of force in the system?) theoretically answered (or at least hypothesized), I began work on the second question: What exactly influences the development of an effective interfacial system voltage given an applied voltage or current?

To answer this, I filled out the generalized force models from Chapter 3 using parameters taken almost entirely from empirical measurement. I validated this model with I versus V Lissajous curve observations and used small signal electrical and electrochemical impedance measurements to capture model parameters. At the end of this chapter I discuss how isolated measurements and those taken as a whole converge to unambiguously confirm the existence of a prominent interfacial gap impedance, and show how this gap impedance compares to other elements in the system.

4.1. Rotational Tribometer

I constructed a custom rotational tribometer to provide a velocity and normal force controlled platform for various experiments. The device was built around a modified turntable (ST.150, Gibson Guitar Company, TN, USA). Data was collected using a 16 bit data acquisition (DAQ) board (NI USB-6361, National Instruments, TX, USA) with a sampling rate of 250 kHz, unless otherwise stated. The direct drive turntable maintains a constant rotational velocity via an internal controller, and is monitored by reading the
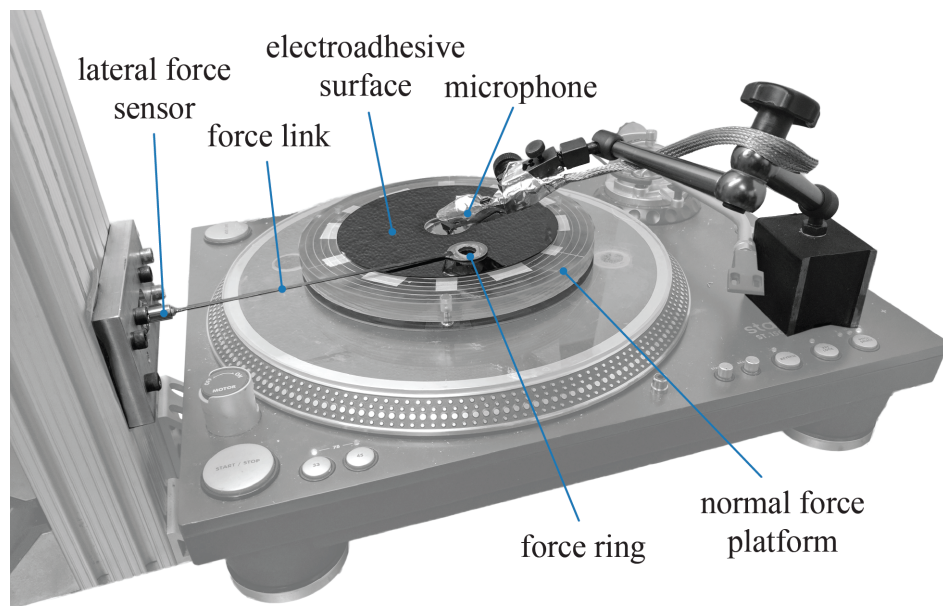
Figure 4.1. Overview of rotational tribometer apparatus and recording instruments. The rotational slip ring, hand rest, and supporting frame have been temporarily removed for clarity.

internal quadrature encoder. The translational velocity at the finger was held at 170 mm/s for all experiments involving movement. A general layout of the apparatus can be seen in Fig. 4.1.

Normal force applied by the finger was monitored using a custom force platform based on three piezoresistive force sensors (FSS1500NSR, Honeywell, MN, USA) mounted to a 12mm thick acrylic disc. The force signal was conveyed off of the platform using a rotational slip ring and displayed on a visual screen for user feedback. Normal force was held at 1N for all experiments.

Lateral force was measured using a piezoelectric force sensor and charge amplifier (9217A and 5010B, Kistler Instrumente AG, Winterthur, Switzerland) which was coupled to a patch of skin contacting the rotating plate via a carbon fiber link and a 0.5 mm thick

FR4 fiberglass ring with 25 mm OD and 13 mm ID (also shown in Fig. 5.1a). A PTFE ring spacer, 0.5 mm thick with 25 mm OD and 23 mm ID, was affixed to the bottom of the fiberglass ring. This spacer ensures that any normal force not traveling though the contact patch has minimal effect on measured lateral force. It also constrains the gross contact area of the skin to $\approx 100mm^2$.

4.2. Electroadhesive Surfaces

Two 150 mm diameter discs with electroadhesive surface coatings were used for experiments, as seen in Fig. 4.2. Both coatings were chosen primarily due to their electrical and frictional properties. In particular, each surface shows good stability in friction force with fingertip sweat pore occlusion, allowing friction measurements that are consistent over long time scales. Each surface also exhibits appreciable electroadhesive effects across an exceedingly wide range of frequencies and with relatively small applied voltages.

The transparent disc on the left of Fig. 4.2 was cut from a readily available touch screen system sold by 3M (tradename 3M MicroTouch™). It's referred to here as the 3M coating. The disc consists of a 3 mm thick glass substrate, on top of which is a 40 nm indium tin oxide (ITO) conductive layer, and a 1 μm SiO_2 dielectric layer [13]. Notably, this surface coating was chosen as it has become increasingly popular with a number of research groups utilizing the electroadhesive effect [3] [13] [14] [15] [16] [17]. Despite its recent popularity in the research community, relatively little is known on how to electrically excite such a surface in order to achieve desired force characteristics. This work aims to help fill this gap.
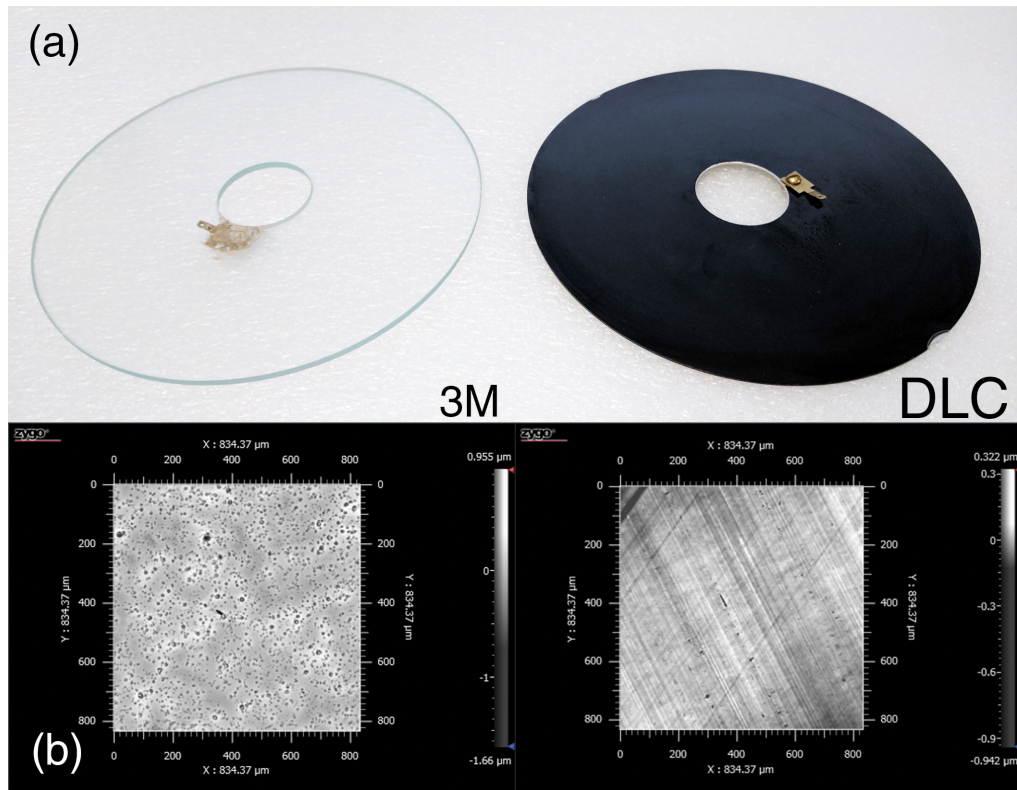
Figure 4.2. (a) Transparent 3M MicroTouch$^{\text{TM}}$ silica coated glass substrate (left), and mildly opaque black DLC BALINIT$^{\circledR}$ DYLYN PRO coated substrate (right). (b) Optical profilometry image of an approximate 0.8x0.8 mm patch of 3M (left) and DLC (right) coatings.

The disc was cut using a CNC waterjet cutter specifically adapted to cut glass. A new direct electrical connection was made to the ITO layer using a conductive silver epoxy on the cut edge of the glass. Importantly, this separate connection to the ITO layer bypasses the normal series capacitance of 3M MicroTouch$^{\text{TM}}$ screens which, if left in place, results in a substantial voltage attenuation in the system, necessitating the need for a higher driving voltages. This series capacitance is also thought to dramatically impact the electrical dynamics of the system at low frequency, as modeled in [**13**].

The second electroadhesive surface (seen on the right Fig. 4.2) used was a 1mm thick aluminum disc. This disc was coated with a diamond like carbon (DLC) coating using a chemical vapor deposition (CVD) process. It is referred to here as the DLC coating. It is approximatly 2 μm thick and goes by the trade-name BALINIT® DYLYN PRO. This coating is specifically designed for plastic injection molding type applications, and has low surface adhesion characteristics. It was chosen to offer a comparison to the 3M coated surface, and to highlight the ubiquity of the electroadhesive effect with thin, low friction surface coatings.

The topographic roughnesses of each surface, shown in Fig. 4.2b, was characterized by a 3D optical surface profiler (Nexview, Zygo Corporation, PA, USA). The 3M coating has and RMS roughness of 193 nm, while the DLC coating has an RMS roughness of 35 nm. Profilometery also revealed the abundance of microscopic pores on the surface of the 3M coating that appear to partially, or perhaps fully, penetrate the silica layer. In contrast, the DLC coating appears to have good conformity, and no pinholes were observed.

4.3. High Performance Current Controller

Current control is again utilized in all experiments for two primary and related reasons: safety and uniformity of effect. Recommended current threshold levels outlined in [46] [47] were adhered to for all experiments, and applied current remained below the limit of electrocutaneous stimulation.

An effective way to ensure this current threshold is with a current controlled source. A voltage controlled source is susceptible to sudden decreases in total system impedance (such as dielectric coating breakdown or sweat accumulation between the finger and
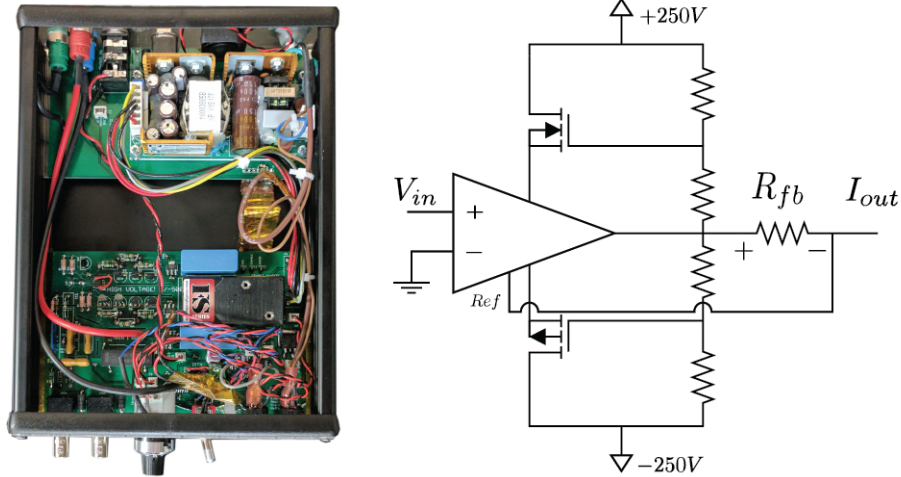
Figure 4.3. High voltage compliant current controlled amplifier with integrated voltage and current sensing circuitry (left) and a simplified electrical schematic showing the amplifier operating principle (right).

surface) which can result in sudden increases in total system current beyond recommended thresholds (shorting). The insensitivity current control offers to changes in system impedance also implies increased uniformity in electroadhesive effect, as it imposes a more uniform voltage across the skin/surface interface regardless of changes in skin, surface, or other environmental impedances such as poor grounding conditions.

A custom high voltage compliant, transcondutance amplifier, seen in Fig. 4.3 (left), was constructed and characterized. The amplifier can source or sink up to 5 mA with a voltage compliance of ± 250 V. It is built around a high common mode voltage differential amplifier (AD8479, Analog Devices Inc, MA, USA) in a bootstrapped power supply configuration. Current is controlled via a 1 kΩ 0.1% feedback resistor in a modified Howland current source topology. A highly simplified schematic of this circuit topology can be seen

in Fig. 4.3 (right). Input voltage V_{in} is applied across the input terminals of the differential amplifier. This amplifier then outputs a current, I_{out}, across R_{fb} such that the voltage across R_{fb} is the same as V_{in}. The transconductance gain of this amplifier, therefore, is equal to $1/R_{fb}$. The resistor ladder and feedback transistors perform the bootstrapping operation in the circuit, floating the the differential amplifier power supplies above and below the required output voltage. Further discussion as to the design and construction of this amplifier are given in Appendix A.

An equivalent output impedance of the amplifier was measured to be on the order of 20 MΩ, limited only by the input common mode rejection ratio (CMRR) of the differential amplifier. The amplifier bandwidth is partially limited by stray output capacitance to ground, and a capacitance compensation positive feedback circuit was utilized to mitigate this effect. With capacitance compensation, the measured -3 dB bandwidth into a typical load impedance was 45 kHz. This represents the large signal working bandwidth of the amplifier into a capacitive load. Additionally, total harmonic distortion (THD) for applied current was measured to be less than 1% throughout this entire range. Redundant internal safety mechanisms limit the possible applied current to <10 mA.

4.4. Current and Voltage Measurement

The setup seen in Fig. 4.4 was used for all electrical measurements presented. The current controlled amplifier applied a test current to an unknown impedance, Z_{ut}, and actual current was measured using a series shunt resistor (1 kΩ 0.1%). This value was small with respect to most impedances measured, thus introducing negligible error. Regardless, it was subtracted from all impedance measurements.
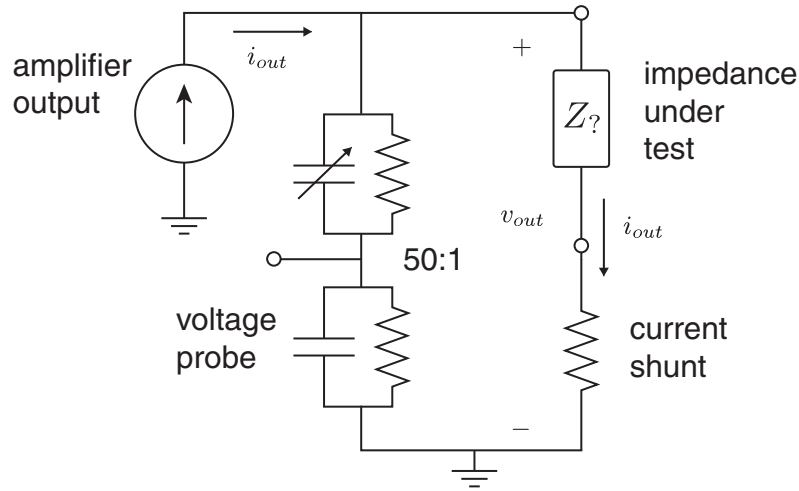
Figure 4.4. Current and voltage measuring setup consisting of a 50:1 impedance divider probe and low side current shunt resistor.

Voltage was monitored using a custom 50:1 high impedance ($\approx 500M\Omega||10pF$) probe. This high impedance ensures that, even for unknown impedances on the order of $10M\Omega||100pF$, the majority of output current travels through the impedance under test, and is not diverted through the probe. The voltage probe and current shunt voltages were buffered by high precision op-amps (OPA192, Texas Instruments Inc., TX, USA) and sampled by the DAQ. Under these conditions, impedances ranging from $\approx 10^3 - 10^8\Omega$ may be measured with minimal error due to probing.

4.5. Electrode and Interface Contact Conditions

Four different electrode and interface conditions, seen Fig. 4.5, were used. They can be broken into a purely electrical impedance condition (I), an electrochemical bioimpedance condition (II), and two conditions that include both electrochemical and electrical impedances (III), (IV). Gross area of contact was held constant between each condition at just under 1 cm^2. I used my non-dominant index finger in conditions (II), (III), and (IV).

Condition (I) was used to investigate the properties of the 3M and DLC dielectric coatings in isolation. Current was supplied to the conductive substrate (ITO or aluminum) and was returned via a copper disc electrode. The copper electrode was coupled to the top side of the coating using a thin layer of conductive silver grease (MG Chemicals 8463). With electrodes on the top and bottom of the coating layer, the impedance through this layer could be measured.

Condition (II) was used to probe the bioimpedance of the skin and body. Current was supplied to the fingertip via a Ag/AgCl electrode with solid electrolyte gel filled sponge (3M Red Dot 9641), seen Fig. 4.7. The Ag/AgCl interface provides very low and stable DC and AC polarization impedances associated with the electronic to ionic
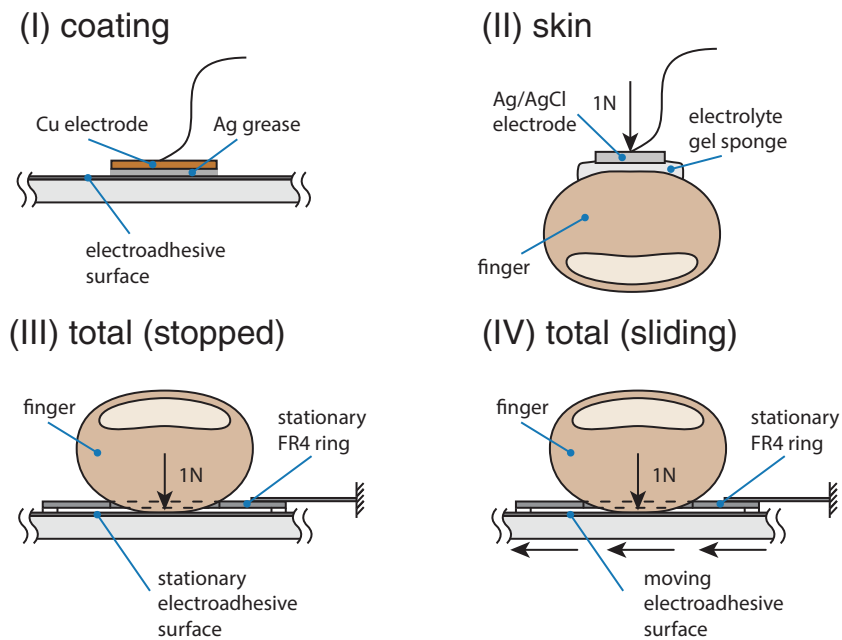
Figure 4.5. Side view of 4 interface conditions: (I) the surface coating in isolation, (II) the skin in isolation, (III) the total impedance of a stationary finger on the surface, and (IV) the total impedance during sliding between the skin and coating (not to scale).

conversion, and also has a very low half-cell potential. In addition, the solid gel electrolyte sponge limits the wetting and penetration of the electrolyte into the skin of the finger, and allows the contact area to be approximately constant and well defined [**48**]. An isolated measurement of two electrodes back to back confirmed that the electrode's combined polarizing and gel impedance was far below other measured impedances, and on par with similar measurements made for Ag/AgCl electrodes.

From the electrode, current travels through the skin of the fingertip, down the hand, and exists the body on the ventral forearm via two Ag/AgCl electrodes of the same type which had a combined 6 times larger contact area than the fingertip electrode. The impedance due to this wrist interface was measured (using a 3 electrode configuration) and found to be approximately 10 times smaller in magnitude than the impedance measured from the fingertip, meaning its bioimpedance contribution is minimal.

Interface conditions (III) and (IV) represent the total electrical impedance that is observed as a finger interacts with each electroadhesive surface. They are used to investigate aspects of electroadhesion which are directly relevant to its practical application, and which illuminate the underlying principles of operation. Current is applied to the electroadhesive surface, as in condition (I), travels through the surface coating, across the coating/skin interface, through the skin and body, and is returned via the Ag/AgCl electrodes at the wrist described in condition (II). Applied normal force was held at 1 N using feedback from the normal force platform. During condition (III), the finger and surface are stationary, while in condition (IV) the surface slides under the finger with a constant velocity of 170 mm/s. Apparent area of contact is controlled by use of a small FR4 ring,

which is glued to perimeter of the skin contact patch and mechanically grounded via a carbon fiber rod.
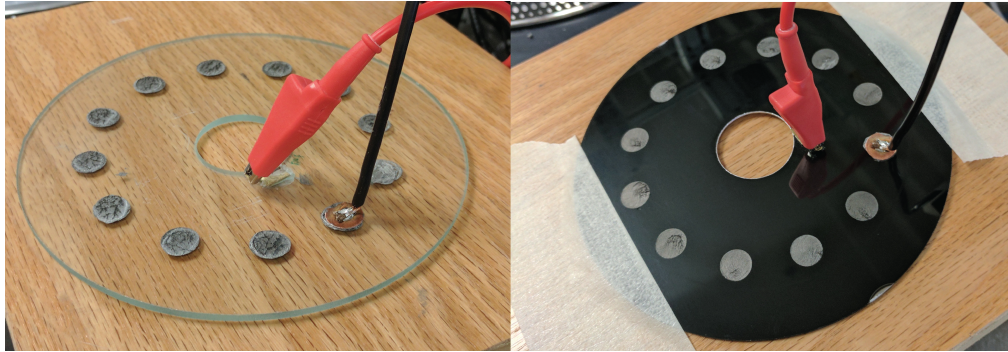
Figure 4.6. The 3M coated surface (left) and DLC coated surface (right) with silver conductive grease applied at 12 different locations. These locations represent where the impedance through the coating layers was measured.
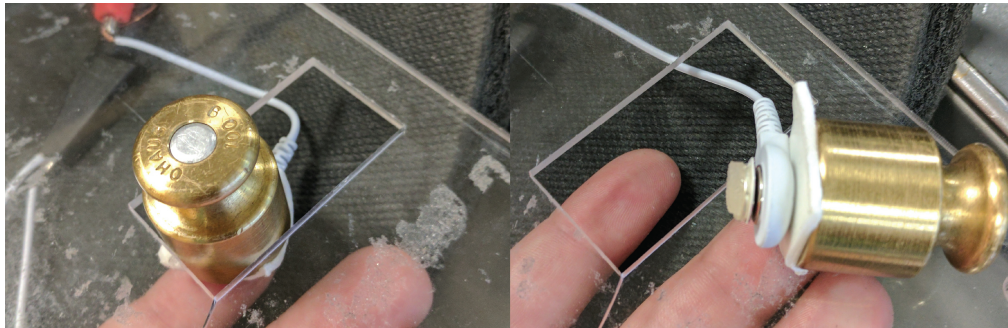
Figure 4.7. Conditions at the fingertip for measuring the bioimpedance of the skin and body. The small Ag/AgCl electrode was stamped out from a larger electrode, and attached to a weight, which was then allowed to bear against the finger. An acrylic frame constrained the weight horizontally.

4.6. Electrical Model and Definitions

4.6.1. Electrical Impedance Model

I adopt the series gap impedance based approach, introduced in Chapter 3. This model assumes that the only voltage which is frictionally relevant is that which develops across
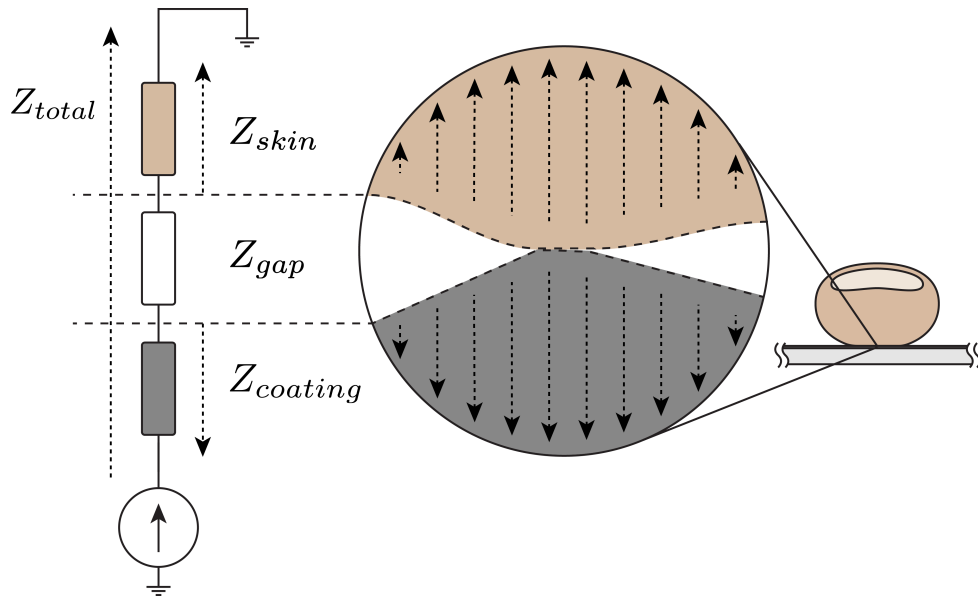
Figure 4.8. Lumped series electrical impedance model (left) showing the definitions of the skin, gap, coating, and total impedance parameters. Also shown in a conceptual image of the gap (right), where the outer of the skin touches the top surface of the coating at a small asperity point. The interfacial gap consists of a small number of these asperity points, and is mostly filled with air elsewhere.

the small interfacial gap between the finger and surface, called V_{gap}. Analysis of this assumption is presented in Chapter 5. Here, I simply relate the air gap voltage, V_{gap}, to the more macroscopic system parameters, total applied current, I_{total}, and voltage, V_{total}, by assuming a linear lumped series impedance model, Fig. 4.8, and performing measurements to investigate these impedances.

4.6.2. Definition of Skin and Coating Impedances

My model lumps the skin and body bioimpedances into a single Z_{skin}, which describes the impedance seen looking from the outside surface of the stratum corneum through the skin and body to ground. In a similar manner, I define the bulk dielectric coating impedance,

$Z_{coating}$, as the impedance seen looking from the top surface of the coating through the coating itself back to the current source. This coating impedance was previously called $Z_{dielectric}$, but its name is changed here to reflect the fact that it may not necessarily be a pure dielectric.

4.6.3. Definition of Total Impedance

The total impedance Z_{total}, is defined as the total observed impedance seen during normal operation from the output of current controlled amplifier through the electroadhesive coating, contact interface, skin, body, and to ground. It is measured under two conditions, when the surface is sliding relative to the finger, $Z_{total(sliding)}$, and when the surface and finger are stationary, $Z_{total(stopped)}$.

4.6.4. Definition of Gap Impedance

The gap impedance, Z_{gap}, is the hardest impedance to define. This is because the gap impedance is used to capture and describe the interface conditions between the skin and the coating surface. As such, it is a variable impedance that can possibly change with spatially dependent parameters such as skin/surface geometry and relative motion, as well as time dependent parameters such as sweat accumulation or viscoelasticity of the skin. For a complete description, the electrode polarization impedance associated with this interface, including any electric double layers and any Faradaic current paths, should also be theoretically included.

With this description, it is impossible to define the gap impedance in isolation, but rather it should always be described with respect to Z_{total}, and set of contacting surfaces

and conditions. Therefore, I define the gap impedance, Z_{gap}, as the impedance that remains from a given measurement of Z_{total} after other known impedances in the system have been accounted for.

4.7. I vs V Curve Experiments

4.7.1. Data Collection

The first assumption I tested for in my impedance model was linearity. This was done by generating a collection of Lissajous curves to inspect the behavior of the different conditions. A sinusoidal current of $\pm 0.1 mA$ was applied using interface conditions (I), (II), and (IV). Conditions (I) and (IV) were measured with both the 3M and DLC coating, each at a single representative location. Six frequencies were chosen, from 0.1 Hz to 10,000 Hz. Voltage and current were sampled at 50x the excitation frequency for 20 complete cycles. The resulting data was bandpass filtered digitally, with corner frequencies an order of magnitude above and below the actuation frequency, using zero phase delay butterworth filters. This filtering reduces the effect of noise in the raw data, yet still allows non-linear harmonics to be apparent.

4.7.2. Results and Discussion

Data from all 30 experiments (5 conditions, 6 frequencies) are displayed in Fig. 4.9. There are a number of general trends, and some specific observations to note.

First, all impedances measured appeared to exhibit quasistaic and resistive like behavior at low frequency, and gradually transition into more capacitive like behavior as frequency increased. This is evidenced by the shape of each curve, which moves from
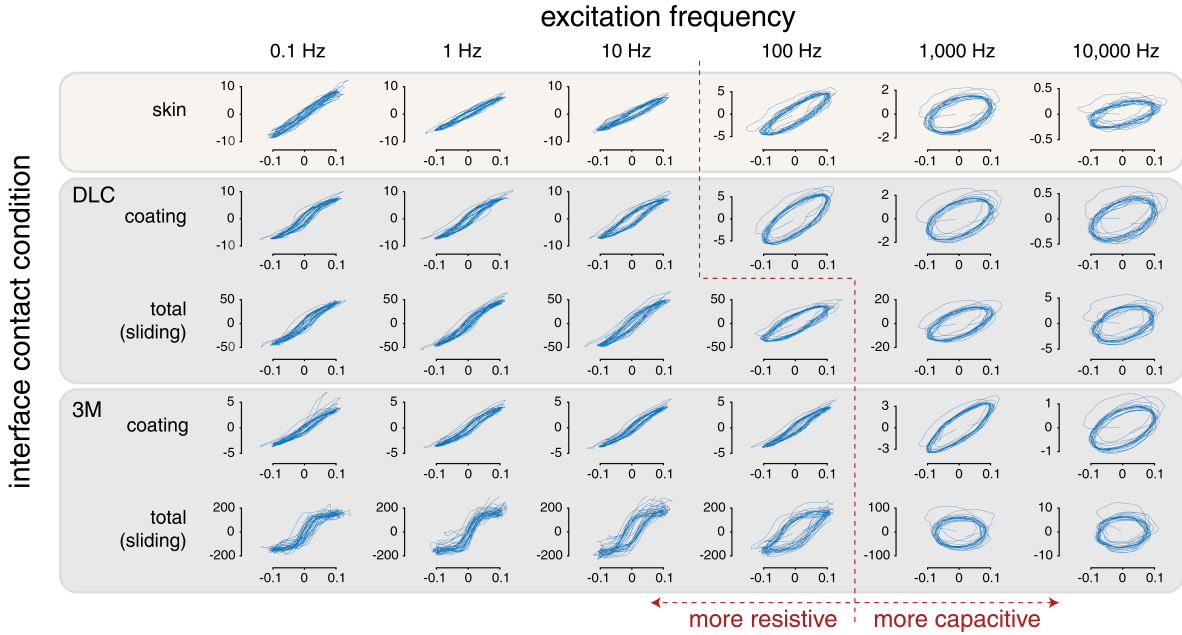
Figure 4.9. Set of 30 current vs voltage Lissajous curves (5 interface conditions and 6 frequencies) created using $\pm 0.1 mA$ sinusoidal test currents. All horizontal scales are current in milliamps, all vertical scales are voltage in volts.

an in-phase line like shape at 0.1 Hz, to an out-of-phase ellipse like shape at 10,000 Hz. This transition is also seen in the overall voltage magnitude, which remains approximately constant across each condition for frequencies below 10 Hz, and then attenuates at higher frequencies. The red dashed line in Fig. 4.9 roughly marks where this transition point takes place for each condition.

Another general trend is that the peak voltage in the total (sliding) conditions is approximately 2x (for DLC) or 10x (for 3M) the combined peak voltages of the skin and respective coatings. This substantial increase in voltage seen in the total (sliding) case is the first bit of direct evidence for a large interfacial gap impedance not accounted for by the skin or coating impedances.

In terms of linearity, each condition displayed non-linear behavior in the lower frequency ranges, even for this relatively small $\pm 0.1mA$ current. These effects appear least pronounced in the skin, and more pronounced in each coating. Also, the total (sliding) case for the 3M screen showed a rapid breakdown type phenomenon at $\approx \pm 150V$, which did not go away until 1,000 Hz, when the resulting voltage fell below this threshold. This breakdown could be heard and felt at the finger in the form of a crackling vibration (but not an electrocutaneous sensation), and is most likely a result of the dielectric breakdown of air in the gap. This fact was later confirmed using optical imaging of the gap, where small points of breakdown could be seen occurring along the fingerprint ridges, presumably at areas of concentrated electric field. In contrast to the lower frequencies, linearity at higher frequencies (and currents) appears to be preserved.

The main conclusion from these experiments is that the linearity of the impedance model introduced earlier cannot be taken for granted, and appears only to be valid for small currents, or when the actuation frequency is sufficiently high as to be solely in the capacitive regime.

4.8. Electrical Impedance Experiments

4.8.1. Data Collection

Results from the previous experiment informed the collection of small signal impedance data. All impedances were measured with a 2s $\pm 10\mu A$ sinusoidal test current where all impedances remained linear. The resulting sinusoidal test voltage was recorded, and the

complex impedance under test

$$(4.8.1) \qquad Z_{ut}(f) = \frac{V_{out}(f)}{I_{out}(f)} = |Z_{ut}(f)|e^{j\angle Z_{ut}(f)}$$

was found using a digital lock-in technique. The 4 interface conditions were measured using both coatings for conditions (I), (III), and (IV). This resulted in 7 unique impedance measurements. Thirty logarithmically spaced frequencies from 1 Hz to 50,000 Hz were tested for each impedance curve measurement (frequency order randomized).

Interface condition (I) was measured at 12 equally spaced locations on the circular path that the finger traverses in condition (III) and (IV), seen Fig. 4.6. At each location, 4 trials were taken back to back, for a total of 48 impedance curves. A single mean and standard deviation was computed across all trials and locations. Condition (II) was measured at the tip of my non-dominate index finger with a series of 10 consecutive trials. The finger was wiped with 70% IPA solution in-between trials and allowed to dry. Applied normal force was held a approximately 1N with a weight, seen Fig. 4.7. Similar to condition (I), condition (III) was measured at 12 locations with 4 trials at each location for a total of 48 trials, and a single mean and standard deviation was computed. I cleaned my finger with IPA and allowed it to dry before each new location, letting at least 10 seconds to pass between my finger touching the disk and the measurement starting as to allow the impedance value to stabilize. Condition (IV) was measured as a series of 10 trials, with my finger and disk cleaned once with IPA at the beginning of all the trials. This was due to the fact that my finger was glued to the FR4 ring, and difficult to remove and clean between trials.

4.8.2. Results and Discussion

Results from the electrical impedance measurements are shown in Fig. 4.10 and Fig. 4.11. In general, these results are highly consistent with the results from the IV curve experiments, but are able to more quantitatively capture the behavior of the various impedances. The details and interpretation of each measurement are given below:

4.8.2.1. Skin and Body Impedance. Recordings of the skin and body impedance show a small variance from trial to trial, Fig. 4.10 (top). As seen by the phase angle, the impedance curve can be split into 3 different regimes, a resistive regime at low frequency, a more capacitive regime starting between 10 and 100 Hz, and another resistive regime after 10 kHz.

This impedance behavior is highly consistent with established literature, as, for many in vivo bioimpedance recordings, the stratum corneum dominates the overall impedance at low frequencies (below 10 kHz), while the resistance of the viable layers of skin and underlying tissue dominate at higher frequency [48]. The increase in phase angle and leveling off of the magnitude after 10 kHz, therefore, is due to the internal body impedance between the fingertip and return current electrodes, a fact also confirmed from a 3 electrode measurement near the return current electrodes. It can be modeled as a ideal resistance.

The behavior of the impedance below 10 kHz (due to stratum corneum) cannot be accurately modeled by a pure resistor in parallel with a capacitor, as the overall phase angle never reaches 90 degrees, but levels off just shy of 70 degrees. Instead, it is common to use a constant phase element (CPE) in parallel with a resistive element [48], which I found can reasonably capture the impedance magnitude behavior of my data. Indeed, CPEs are quite common in electrochemical impedance spectroscopy measurements, and
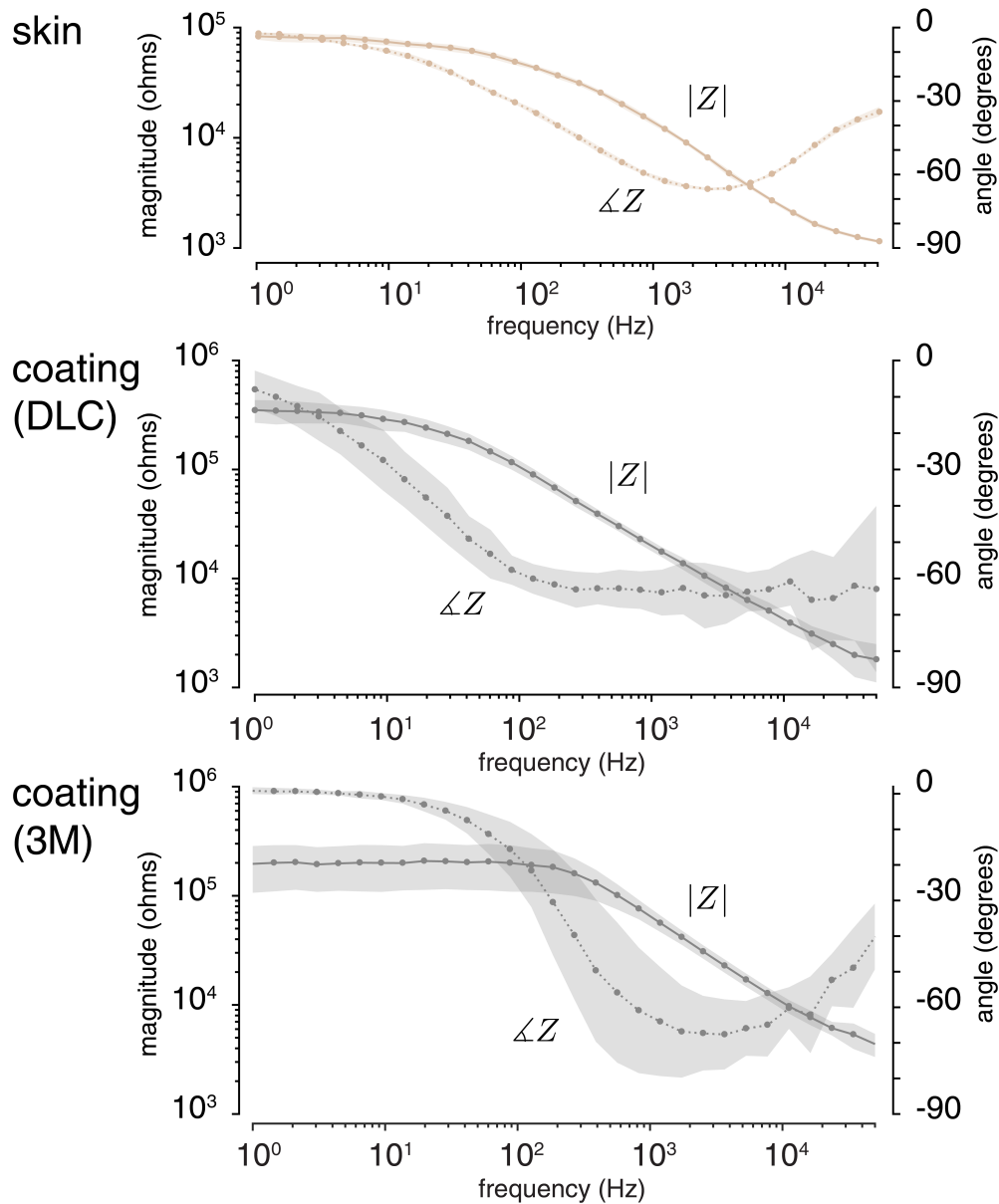
Figure 4.10. Skin and body impedance (top), DLC coating impedance (middle), and 3M coating impedance (bottom) as measured in isolation. The centerline represents trial means, while the shaded regions represent $\pm 1\sigma$. A dashed line indicates phase, while a solid line is impedance magnitude. Area of contact $\approx 1cm^2$, and current $= \pm 10\mu A$.

can possibly be explained by not a single RC time constant for the impedance, but a distribution of time constants across an interface due to changes in resistivity [49]. In the case of the skin, the parallel resistive behavior is due to the sweat ducts and ionic conduction of the stratum corneum itself, while the capacitive constant phase behavior in this frequency range is most likely due to counterions and other charged (but bound) molecules in the skin interacting with a localized gradient of resistivity increasing from the inner viable skin to the dry and dead outer skin. This interaction could then generate a distribution of RC time constants in the stratum corneum.

4.8.2.2. DLC Coating Impedance. The impedance recorded from the DLC coating, Fig. 4.10 (middle), shows highly resistive behavior at 1 Hz, which immediately begins a transition to constant phase element like behavior. Consequently, its overall empirical magnitude seems to be captured well by a resistor in parallel with a CPE, but, unlike the skin, not much can be said as to the origin of either the resistive or capacitive effects. The resistive behavior at larger currents is non-ohmic (as seen in Fig 4.9), therefore some type of semiconductor conduction mechanism is assumed, but analysis beyond this level was not performed, and the there is little in the literature to suggest a specific conduction mechanism. Similarly, the CPE behavior could possibly be caused by a distribution of resistivity within the $2\mu m$ coating, as observed in other thin films [49], interacting with normal polarization mechanisms of the DLC coating.

4.8.2.3. 3M Coating Impedance. The impedance behavior of the 3M coating was unexpected, as it was previously assumed that the $1\mu m$ silica coating was a pure dielectric insulator, with no low frequency or DC conductivity [13]. As the results of Fig 4.10 (bottom) show, this is not the case. There is variable resistivity which dominates below

approximately 100 Hz. Beyond 100 Hz, the impedance shows a transition to capacitive behavior and, unlike the skin and DLC coating, it appears to be captured well using an ideal capacitor. This assessment, however, is difficult to make, as, at even higher frequencies, the impedance becomes resistive again, indicating a additional series resistance. Regardless, this coating's overall impedance behavior seems to be captured well using a resistor in series with a resistor and capacitor in parallel.

The physical mechanism for the parallel resistance seen at low frequency is uncertain, though it is believed to be related to a non-conformity (pin-holes) of the coating seen in profilometry data, as SiO_2 typically has a resistivity on the order of 10^{16} Ωm. It could, however, also be due to a semiconductive mechanism. The parallel capacitance is consistent with a typical parallel plate capacitor with the dielectric and geometric properties of the SiO_2, and the series resistance can be explained by the non-zero sheet resistance of the ITO layer.
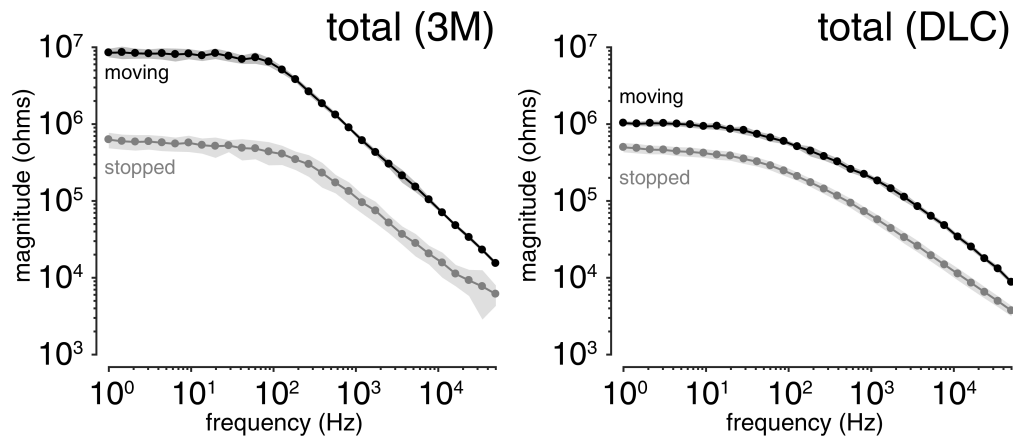
Figure 4.11. Measurement of the total system impedance seen while the surface is stopped (III), versus sliding (IV).

4.8.2.4. Total Impedance, Sliding and Stopped. Fig. 4.11 shows the magnitude of total impedance, Z_{total}, measured in both sliding and stopped cases. In the sliding cases, measurements show similar RC characteristics as those in Fig. 4.10. The 3M case is almost exactly an RC model, while the shallow slope of the DLC case mimics its underlying coating, and can be modeled by a CPE. Compared to the stopped case, however, the sliding data reveal an increase in impedance magnitude of approximately 10x and 2x for the 3M and DLC surfaces respectively. It is unclear why this increase is larger for the 3M screen than the DLC, though its speculated to be caused by the increased surface roughness of the 3M (192nm RMS) coating as compared to the DLC (35nm RMS).

In both cases the total impedance observed while stopped is very nearly equal to the series combination of the respective coating and skin impedances measured in isolation. There is a small difference between the two, however this difference appears consistent with a change in effective contact area between conditions (I)/(II) and condition (IV) (assuming the gross area is in contact with the former, and a smaller area, only the fingerprint ridges, is in contact with the latter). This fact implies that the large change from the sliding to the stopped case cannot be accounted for by other system impedances, but must be the result of an additional physical impedance mechanism, the so-called gap impedance. To put another way, measurements in Fig. 4.10 and 4.11 support the hypothesis that, in going from sliding to stopped, the gap impedance is essentially shorted out, and all that remains is the series combination of the skin and coating impedances. It is hypothesized that this impedance drop is due to a buildup of sweat in the air gap, which is both highly conductive and has a much higher dielectric constant than air, each of

which would dramatically lower the gap impedance. However, more evidence is needed to support this claim, as it could also be due to a relaxation of the skin, causing dramatically increased real area of contact, or a combination of effects.

4.8.2.5. Gap Impedance in Relation to the System. With the existence of the interfacial gap impedance in clear view from Fig. 4.11, I can estimate its value and influence on the to the total system impedance. One way to calculate its value is to simply subtract off the skin and coating impedances from the total impedance seen while sliding:

$$(4.8.2) \qquad \boldsymbol{Z_{gap}} = \boldsymbol{Z_{total(sliding)}} - \boldsymbol{Z_{skin}} - \boldsymbol{Z_{coating}}$$

With this done, I can also calculate the relative impedance magnitude ratio for the skin, coating and gap impedances. This is defined by

$$(4.8.3) \qquad ratio = \frac{|\boldsymbol{Z_i}|}{|\boldsymbol{Z_{total(sliding)}}|}, \quad i = skin, coating, gap$$
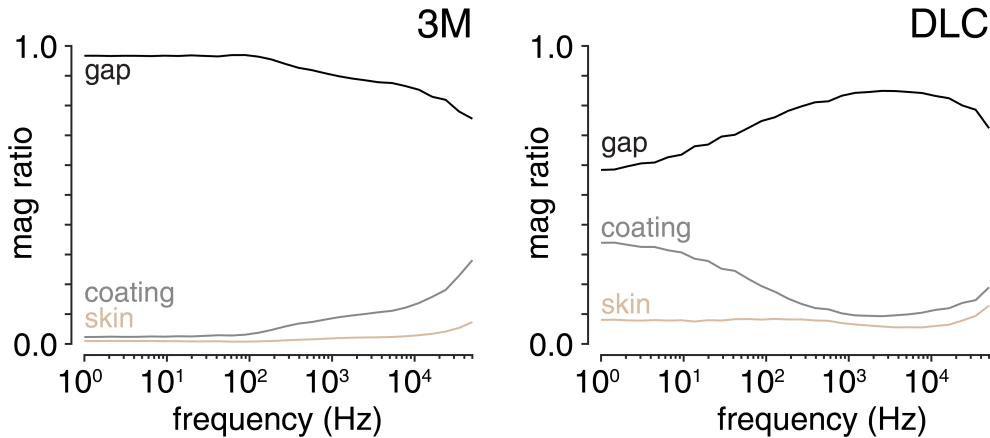
Figure 4.12. Calculated magnitude ratio of each given impedance to that of the total systems impedance seen while sliding.

which allows me to estimate the contribution of each impedance mechanism to the overall system impedance. This ratio is plotted for each element and surface in Fig. 4.12.

As can be seen, the gap impedance clearly dominates the total impedance seen in the 3M case, and remains a majority of the impedance in the DLC case, across the entire frequency range. This implies that the coating and skin impedances have intrinsically small contributions in relation to the gap, and that, for a given applied voltage or current, only a small voltage drop develop across them. The majority of the voltage will instead develop across the gap.

This is a important point, and one that is most likely true only because my careful selection of the surfaces and preemptive elimination of other unnecessary impedances. For a thicker dielectric coating, for instance, this will not be the case, nor would it be if the series capacitance of the 3M screen is left intact, or if careful grounding conditions were not ensured. In fact, I propose that the gap impedance magnitude ratio could be viewed going forward as a metric for the electrical effectiveness of an electroadhesive surface given an applied voltage.

4.9. Chapter Summary

I presented a series impedance model based off of empirical measurement techniques and validated the linearity of this approach under certain conditions: small applied currents or high frequencies. The results of these measurements show that the impedance elements can generally be thought of as resistances in parallel with capacitances. However, while the capacitive behavior is ideal for the 3M based measurements, it is not for

the skin and DLC based measurements. Both coatings tested can sustain a gap voltage while sliding at all frequencies tested, and therefore can produce both DC and AC electroadhesive forces. The skin and coating impedances appear minimal compared to the gap, implying that future electroadhesive displays should not focus on these layers directly, but should investigate what factors create and influence the gap impedance, as this seems to be a critical electrical system parameter.

The series model behavior employed is verified by the fact that the sum of the impedances measured in conditions (I)/(II) add up to nearly the same impedance seen in condition (III), except for a small difference (seemingly consistent with a slight change in effective contact area). Because of this, the difference between $Z_{total(sliding)}$ and $Z_{total(stopped)}$ could also be used to estimate Z_{gap}, as opposed to equation 4.8.2, which might allow for rapid characterization of electroadhesive displays.

CHAPTER 5

Application of Broadband Force - Exploiting the Effect

The electrical characterization in the previous chapter is only practically useful if it can lead to new insights as to how electroadhesion can be used to generate force. The primary insight I had from this process is this: *It would appear that, with the mapping out of an applied current to an interfactial gap voltage, the only thing limiting the bandwidth of applied electroadhesive force is the speed at which the electric field can be controlled.* It was with this clear insight in mind, that I set about creating a well-controlled electroadhesive system, which is capable of applying incredibly high bandwidth (and high fidelity) forces to the finger. The motivation which led me in this direction is discussed in the next sections, followed by a description of my force application technique, and recordings and analysis of said forces/vibrations.

5.1. Quasi-static versus Dynamic Actuation

While the quasi-static behavior of variable friction displays has been the primary subject of research for some time, during the course of my research new surface haptic applications utilized increasingly rapid modulation of friction. This transition towards dynamic actuation stems from the fact that, at the time of my work, all known variable friction displays actuate the entire fingerpad in spatial synchrony, i.e. the entire fingerpad is activated at once. This synchrony offers impoverished information to slowly adapting type I tactile afferents (Merkel's discs), which are sensitive to spatial distributions of

strain energy across the fingerpad. In contrast, dynamic modulation of friction is thought to offer rich information for both fast adapting type I (Messiner's Corpuscles) and type II (Pacinian Corpuscles) tactile afferents, which are most sensitive to transient and broadband vibrations in the range of approximately 10-1,000 Hz [50] [51]. Properly actuating the fingertip at these frequencies may be critical to new surface haptic applications such as virtual texture display [52] [53].

5.2. Specific Application: Surface Texture

Variable friction displays appear particularly well suited for the display of virtual surface texture. In this context, the interaction forces encountered by a finger sliding on real texture can be modeled by a quasi-static friction component that changes over a coarse spatial period, representing localized features, and a rapidly oscillating friction component, representing fine textural features [53].

These interaction forces cause vibrations in the finger that are broadband in nature, particularly for fine surface textures, containing appreciable power in the hundreds of Hertz range [54]. These vibrations trigger strong tactile afferent responses, particularly in fast adapting type I and type II afferents, which capture the spectral content of these vibrations with millisecond spike timing precision [55]. Furthermore, this precise timing appears to be preserved in the firing of somatosensory cortex neurons (primarily derived from fast adapting type II afferents) and also appears to influence tactile perception [56].

It seems then that a consistent approach to virtual surface texture display could be to faithfully reproduce these same quasi-static and dynamic patterns of interaction force

that have been measured with real world textures with the aim of achieving the same cortical firing patterns and, ultimately, tactile perception of surface texture.

A final goal of my research, therefore, was to develop an approach to variable friction surface haptics that is sufficiently broadband to offer rich excitation of fast adapting type I and II afferents. Additionally, this approach should have an ideally flat excitation-to-force dynamic response in the range of 10-1,000 Hz. In this remaining chapter I demonstrate that not only is this broadband tactile excitation possible, but the method and hardware I developed may be easily extended to produce programmable audio emanating from a fingertip, adding a complementary sensory modality to the interaction experience. As a side-effect of the modulation method, I also show that ultrasonic friction forces (up to at least 50-60 kHz) can also be applied to the finger. These results reinforce my insight that the only major limitation to the bandwidth of the electroadhesion force appears to be the speed at which the electric field may be applied to the system.

5.3. Related Wide-Bandwidth Variable Friction

The quasi-static behavior of variable friction devices has been previously addressed in the literature and will be only briefly addressed in this work. An emergent area of study, however, is devoted to the question of system dynamic response.

In 2014, Meyer et al. [9] performed initial bandwidth measurements on electroadhesive and ultrasonic variable friction devices, showing overall magnitude and transient responses. Both methods exhibited roll-offs in force starting around 130 Hz. Beyond this frequency, the ultrasonic device continued to show additional force attenuation, while the

electroadhesive device appeared to flatten out to until the end of their 1 kHz measurement range. The authors proposed a second-order resonant mechanical model to partially explain the attenuation of the ultrasonic device, but offered limited characterization of the electroadhesive device. They only suggested that electroadhesive devices are more responsive than their ultrasonic counterparts, presumably due to their solid state nature. A conclusion was that electroadhesive surfaces showed promise for wide-bandwidth force display.

Followup work showed that the limited bandwidth of the ultrasonic device could be mostly corrected for by using a compensation filter and high performance piezo amplifier, capable of driving the piezos at an increasing voltage with increasing modulation frequency [57]. These techniques led to improved high frequency performance at the cost of added complexity and power consumption. This inherent tradeoff between bandwidth and power consumption in ultrasonic devices was also commented on by Wiertlewski et al. [58].

Similar transient step response measurements were made on ultrasonic and electroadhesive devices by Vezzoli et al. [6]. Their measurements supported the conclusion that ultrasonic devices are limited by resonance. They also hypothesized that electroadhesive devices should only be limited by amplifier bandwidth, and that a high-bandwidth amplifier should yield high-bandwidth forces. My work employs such an amplifier, and details the manner of its application.

5.4. Methods and Apparatus

The rotational tribometer described in Chapter 4 and shown in 4.1 was used here. In addition, the high voltage current controlled amplifier and DAQ was also used to

apply and record currents and voltages to the system. Complete descriptions of the two electroadhesive surfaces are also given in Chapter 4.

5.4.1. Lateral Force Sensing

A representation of the lateral force measurement setup can be seen in Fig. 5.1a. The FR4 ring is glued to the perimeter of the skin contact patch using cyanoacrylate adhesive prior to measurements. This ring is intended to isolate the contact patch from the rest of the finger and bone. When linked to the force sensor, it serves to shunt the contact patch lateral stiffness to the bone with the much higher stiffness of the sensor, while adding minimal moving mass (Fig. 5.1b).

The low frequency lateral impedance of an engaged fingertip to bone can be modeled by a linear spring-mass-damper system, with a damped natural resonance occurring around 250 Hz [59]. The equivalent stiffness of a typical fingertip skin patch is low (≈ 1 N/mm), as is the moving mass (≈ 0.1 g). The piezo force sensor used has a stiffness four orders of magnitude greater (≈ 15000 N/mm) and a small moving mass (< 1 g). The carbon fiber link and fiberglass ring were designed to achieve a high stiffness to weight ratio, so as to reduce their impact on the sensor's performance. The distributed mass and stiffness are lumped into m_{sense} and k_{sense}.

Averaged impulse responses of the force link/sensor are shown in Fig. 5.1c. These responses show a large compression mode resonance at approximately 7 kHz, which is damped when the my finger is glued to the force ring. This analysis implies that, below the resonance of the force link/sensor, the measured lateral force represents the applied lateral force at the perimeter of the skin contact patch.
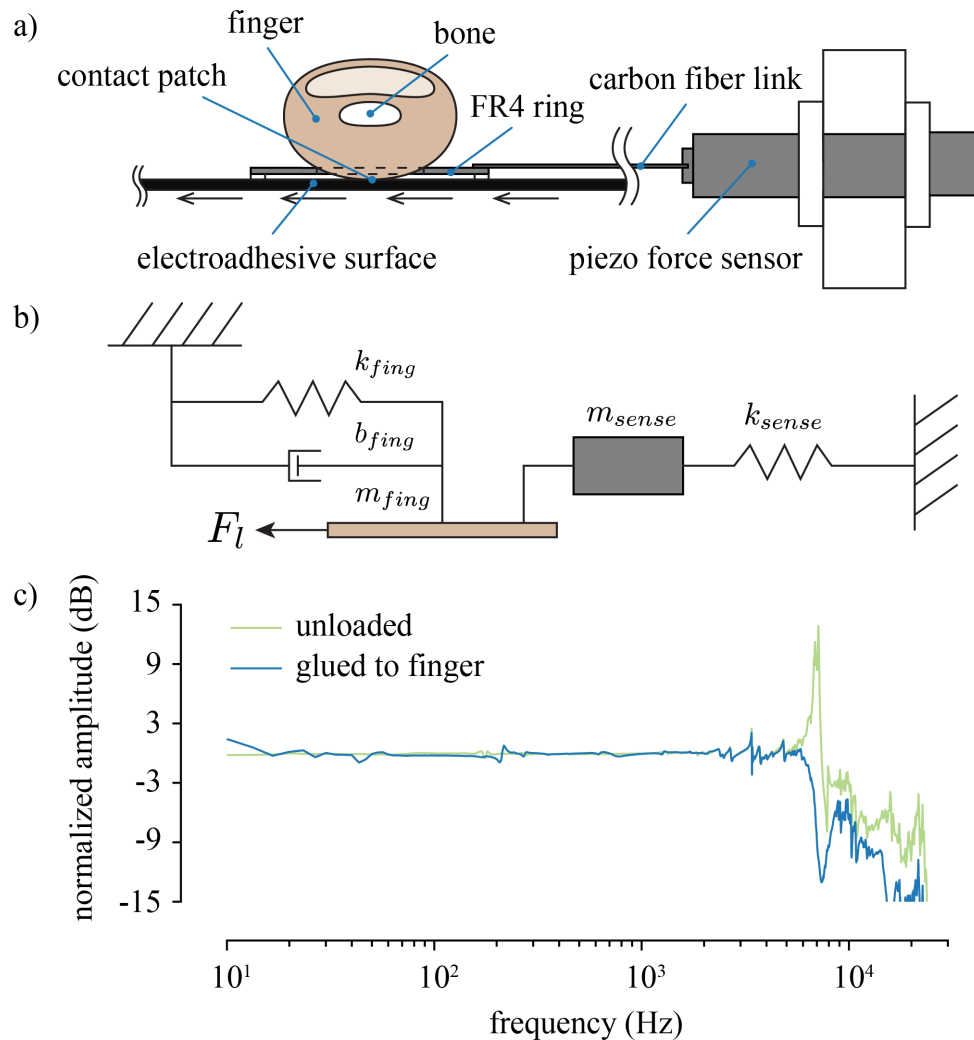
Figure 5.1. a) Cross-section of a finger, glued to a FR4 ring, pressed against the rotating electroadhesive surface. The FR4 ring is affixed to a carbon fiber link and piezo force sensor. b) Lumped lateral impedance model showing the connection of the finger mass and force link/sensor. c) Normalized impulse response of a ball bearing pendulum striking the force link/sensor in axial compression.

5.4.2. Ultrasonic Microphone

Audio emanating from the fingertip was recorded using a MEMS microphone (model number SPU0410LR5H, Knowles Electronics, IL, USA), seen in Fig. 4.1 and Fig. 5.2. This

microphone's frequency response is flat from 100-10,000 Hz, exhibits a broad resonance between 20-30 kHz, and reduced but still appreciable sensitivity far into the ultrasonic regime. This allows basic audio and ultrasonic vibration measurements to be made. The microphone was placed in the acoustic near field of the fingertip, as seen in Fig. 5.2.

5.4.3. Laser Doppler Vibrometer

Velocity of vibrations of the fingertip were recorded with a laser Doppler vibrometer (CLV-1000, Polytec GmbH, Waldbronn, Germany). The decoder range used supports a peak velocity of 250 mm/s at an accuracy of 1.5 um/s from 0.5 Hz to 250 kHz. The laser was focused onto a piece of retroreflective tape glued to the side of my non-dominant index finger, seen Fig. 5.2. The velocity measurement was approximately orthogonal to my fingertip and parallel to the direction of motion of the surface at my finger.
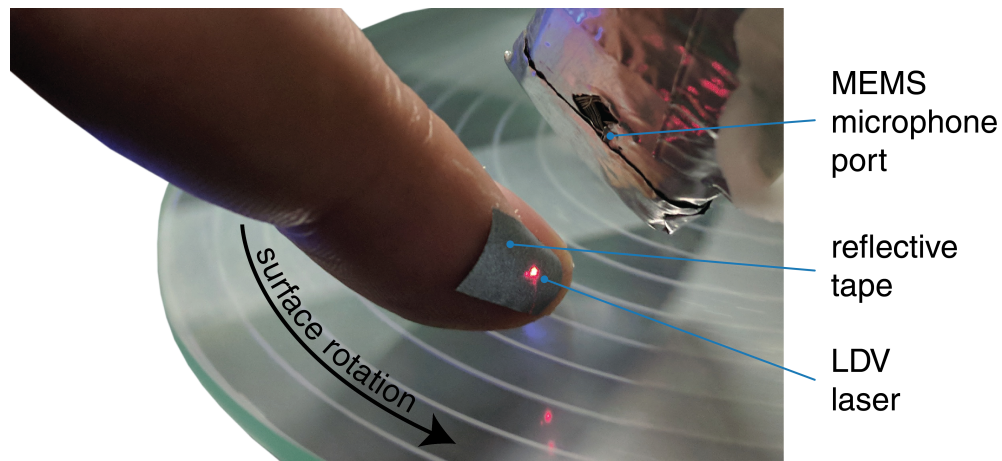
Figure 5.2. Measurement setup for recording vibrations on the skin and in the air as a result of the electroadhesive friction force. Note: the finger is free only during the measurement of vibration (Fig 5.10). For other measurements it is glued to the force ring.

5.5. System Models

5.5.1. Fundamental Force Generation Model

As previously stated, the force model used assumes that the relevant electroadhesive force serving to increase friction between the skin and surface acts not on the skin or surface coating in isolation, but rather across a small air gap formed at the interface of the two. It hypothesizes that this air gap can be modeled as a parallel plate capacitor which has a top plate defined by the outermost layer of stratum corneum and a bottom plate made by the top surface of the electroadhesive coating. With an electric field applied across this air gap, the magnitude of total additional electroadhesive normal force, F_e, pulling down on the charged surface of the skin can be written in scalar form as:

$$(5.5.1) \qquad |F_e| = |Q_{gap}|\frac{|E_{gap}|}{2}$$

where Q_{gap} represents the total net charge on the outer surface of the stratum corneum, and E_{gap} represents the total electric field in the gap. Note the 1/2 term comes from the fact that the charge in the stratum corneum feels only the force due to the electric field created by the opposing charge on the surface of the coating, which is half the total field. Equation (1) is a simplified statement of Coulomb's law for two parallel planes of opposite charge, and it lies at the heart of this electroadhesive force model. It implies that if charge is able to accumulate at edges of the air gap, (regardless the charge being bound or free) and an electric field exists within that air gap, there should be an attractive force generated pulling the skin towards the surface coating and increasing friction. It can also

be put into a more familiar form of a parallel plate capacitor with a distensible dielectric:

$$(5.5.2) \qquad F_e = \frac{A_{gap}\varepsilon_0\varepsilon_{gap}V_{gap}^2}{2d_{gap}^2}$$

where A_{gap} is the area of contact of the gap, ε_0 is vacuum permittivity, ε_{gap} is the dielectric constant of the distensible gap (ε_{gap}=1 for air), V_{gap} is the voltage between the two plates of charge, and d_{gap} is the plate separation. This is a restatement of equation 3.3.1.

5.5.2. Friction Model

The rotation of the turntable ensures a constant slip condition of the contact patch. No stick-slip behavior was observed, and if I model the lateral force conveyed during slipping using a Coulombic kinetic friction model, the effects of electroadhesion can be incorporated by including the additional component of normal force given by equation 5.5.2. This is represented below, where F_l is the lateral friction force (denoted in Fig. 5.1b), μ is the kinetic coefficient of friction, F_n is the externally applied normal force, and F_e is the instantaneously applied electroadhesive force.

$$(5.5.3) \qquad F_l = \mu(F_n + F_e)$$

If F_n is held constant, and μ is assumed constant, then any additional lateral force, F_{add}, is solely proportional to additional applied electroadhesion force.

$$(5.5.4) \qquad F_{add} = \mu F_e, \quad F_{add} = F_{lat} - \mu F_n$$

5.5.3. Electrical Impedance Model

Taken from Chapter 4, the generalized electrical impedance model states that the gap voltage described by 5.5.2 is related to the total applied current, I_{total}, via the complex air gap impedance, Z_{gap}, and Ohm's law:

$$(5.5.5) \qquad\qquad\qquad V_{gap} = I_{total} Z_{gap}$$

As a reminder, the gap impedance can be thought of as the electrical impedance that remains from a measure of the total impedance after all other possible physical impedance mechanisms have been accounted for (such as the series impedances of the skin, body, bulk of the dielectric coating, etc.). It is the electrical impedance associated with the geometric and electrical contact conditions between the skin and surface during sliding.

It was found that this gap impedance accounted for approximately 80-90% of the total system impedance observed during sliding with the 3M coated surface, and between 60-80% with the DLC coated surface. This implies that, for these specific electroadhesive systems, the majority of the total applied voltage is dropped across the air gap impedance. Furthermore, it was found that the gap impedance exhibited two distinct operating regions, a low frequency resistive region and high frequency capacitive region, with a continuous transition zone between the regions from approximately 10-1,000 Hz.

5.6. Impact of Gap Impedance on Force Bandwidth

5.6.1. Predicted Impact

Incorporating the series impedance based electrical model with my force equations, I can begin to predict the impact of the electrical dynamics of the air gap on the force

transduction bandwidth. Combining equations 5.5.2, 5.5.4, and 5.5.5 yields

(5.6.1)
$$F_{add} = \frac{\mu A_{gap}\varepsilon_0\varepsilon_{gap}}{2d_{gap}^2}(I_{total}Z_{gap})^2$$

which is a general equation for the additional lateral force measured by the piezo force sensor given the applied total current and gap impedance. Note that, for this model and my experiments, only the total applied current and gap impedance are assumed to change much with time or frequency. With this assumption I can lump the other system parameters into a single scaling constant

(5.6.2)
$$\alpha = \frac{\mu A_{gap}\varepsilon_0\varepsilon_{gap}}{2d_{gap}^2}$$

and therefore,

(5.6.3)
$$F_{add} = \alpha(I_{total}Z_{gap})^2$$

This equation predicts two important points for current controlled electroadhesive excitation:

(1) The bandwidth of the current controller will directly impact the bandwidth of the electroadhesive force.

(2) For a constant amplitude current source, the resulting dynamic characteristic of the electroadhesive force will mimic that of the air gap impedance squared.

The first point may be neglected below my current controller's DC to 45 kHz bandwidth. The second point, however, is troublesome, as will be demonstrated by a following experiment. Note, however, that with current control the electrical dynamics of other

environmental impedances, such as the impedance from the skin, or the surface coating itself, do not directly contribute to the electroadhesive force dynamics. This is not necessarily the case with a voltage controlled system.

5.6.2. Measured Impact

The 3M coated surface affords a chance to test the force predictions made about the gap impedance, as the gap impedance is essentially the total impedance, implying $Z_{gap} \approx Z_{total}$ and $V_{gap} \approx V_{total}$. This means I can directly measure the dynamic parameters in equation 5.6.3 as I am measuring F_{add} and see how they compare. This could not be done with the DLC surface, as the gap impedance is not as high a proportion of the total impedance, and as the DLC surface exhibits non-linearities at low frequency, which further complicate interpretation of the results.

A sinusoidal test current of $\pm 10 \mu A$ was used at individual logarithmically spaced frequencies from 1 Hz to 3,000 Hz. Applied current and voltage magnitudes were measured using a digital lock-in technique. When an electroadhesive system is subjected to single sinusoid excitation (with zero DC offset) the force response is a sinusoidal ripple at twice this excitation frequency, plus a rectified DC component. It is this double frequency ripple component of force that was recorded in this experiment, again using a digital lock-in technique.

Lateral force, therefore, was recorded from 2 Hz to 6,000 Hz in a series of 10 sequential trials (frequency order was randomized within trials). Additionally, a $10 M\Omega$ resistor was connected from the current output to ground in order to stabilize the DC impedance of the system. This resistance bleeds off excess charge at DC, keeping the electrical system
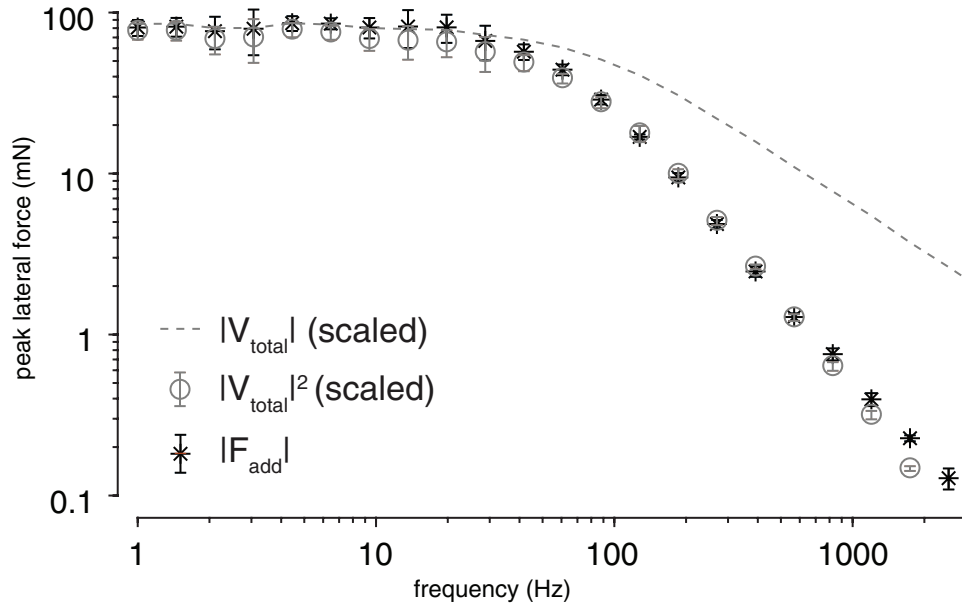
Figure 5.3. Effect of the gap impedance on the force bandwidth with single sinusoid excitation (no modulation). The additional lateral force due to electroadhesion follows the same dynamic characteristic curve as the gap voltage squared ($V_{total} \approx V_{gap}$ for 3M coating).

symmetric, with no appreciable DC voltage component. It was confirmed that the impact of this resistor on the system dynamics was minimal, and did not change the conclusions of the experiment.

Results of the experiment are shown in Fig. 5.3. This plot shows the peak lateral force magnitude, $|F_{add}|$, which occurs at twice the frequency of the recorded total peak voltage magnitude, $|V_{total}|$. The square of the voltage magnitude, $|V_{total}|^2$, was also calculated and shown. Both the voltage, and voltage squared curves have been scaled by an overall linear scale factor to compare their shape with the force curve. Error bars represent $\pm\sigma$.

5.6.3. Discussion

During the experiment, the applied current magnitude was essentially flat with frequency, meaning the dynamic characteristics of the total voltage reflects that of the total impedance, which was previously found to be dominated by the gap impedance. Therefore, it can be said that the gap impedance magnitude is generally flat at low frequencies and begins to attenuate at a rate of -20 dB/decade as the frequency becomes higher. This transition takes place roughly at the RC cutoff frequency of the gap, $f_{RC} = 1/(2\pi R_{gap}C_{gap})$. The impedance could be fit almost perfectly with a $R_{gap} = 17M\Omega$ in parallel with a $C_{gap} = 250pF$, resulting in $f_{RC} = 37Hz$. This calculation implies that not only will the voltage (and thus force) begin to attenuate at very low frequency, but that the most volatile and unknown region of the electrical system dynamics occurs in the relevant tactile frequency range of interest. To put another way, changes to the electrical dynamics far below or above the cutoff frequency are only due to R_{gap} or C_{gap} respectively. Near the cutoff frequency, however, the dynamics are influenced by both R_{gap} and C_{gap} simultaneously.

Second, Fig. 5.3 confirms the impact of the gap impedance dynamics on the force bandwidth, as predicted by 5.6.3. This is evidenced by the fact that the total voltage squared, $|V_{total}|^2$, and additional electroadhesive friction force, $|F_{add}|$, share a nearly identical curve shape, differing only by an overall scale factor. The force attenuation due to the electrical dynamics, therefore, does not occur at a rate of -20 dB/decade, but -40 dB/decade. This means the volatile transition region between dynamic regimes happens within a very narrow range of frequencies, from approximately 20Hz-200Hz. This is troublesome for surface haptic applications as this range is also that of peak tactile sensitivity.

Since my goal was to develop a broadband excitation method with ideally flat frequency dynamics, it does not appear that the direct modulation approach is well suited for the task. Even if I were to compensate for the dynamic curve of Fig. 5.3 by boosting higher frequency current, for instance, there is no reason to believe that this compensation would remain valid across users or across different environmental and surface contact conditions.

Instead, the rest of this chapter will focus on a high frequency amplitude modulation approach to excitation, which I have found to be exceptional in its dynamic characteristics and overall performance, and which avoids this transition region.

As a final note in this section, I used rough gap parameter values to estimate the scaling parameter α, and found my estimate was within $\approx 5\%$ of the value used to plot $|V_{total}|^2$ in Fig. 5.3. The calculation used $\mu = 0.2$, $\varepsilon_{gap} = 1$, an average gap distance, d_{gap} (which calculated by knowing $C_{gap} = 250$pF) of $1.1\mu m$, and a $A_{gap} = 30mm^2$. Note, the value A_{gap} is assumed to be the fingerprint ridge contact area (seen in tribological studies and sometimes called the real contact area, A_r) which has been found to be an average of 30% of the total apparent fingerprint contact area [60]. While the estimate of α could no doubt be made better by an improved measurement of μ and A_{gap}, the insensitivity of α with frequency and its relative estimated accuracy serve as empirical support for the fundamental force and impedance models hypothesized earlier. In fact, I strongly believe that no electroadhesive force model would be able to capture the behavior observed in Fig. 5.3 without the inclusion of the air gap impedance.

5.7. Application of Broadband Forces

5.7.1. Ripple versus Rectified Forces

As mentioned previously, applying single sinusoidal current or voltage excitation to an electroadhesive system yields two force components: a sinusoidal ripple force at twice the excitation frequency, and a rectified DC component. The ripple force is what was measured in Fig. 5.3, and what is used as the primary method of tactile excitation for many finger based electroadhesive setups such as [2] [3] [27] [23] [28] [14] [16] [17].

An alternative manner of exciting these types of systems focuses not on this ripple force, but on the rectified force component. First demonstrated Meyer et al. [13], a high frequency carrier wave can be used wherein the force component at twice the excitation waveform is simply a byproduct of the actuation, and it is the rectified DC force component that is intended to be felt as feedback by the user. In this method, the ripple component should be placed at least at a supratactile frequency ($>$1,000 Hz) and probably at a ultrasonic frequency ($>$20,000 Hz) since it can create incidental audible noise at large amplitudes. The strength of the rectified force component can then be further adjusted in time by modulating the instantaneous magnitude (envelope) of the carrier wave, as demonstrated in [9]. It is this amplitude modulated carrier approach that I expand upon here, though now with a high performance current controller, a higher frequency carrier, different electroadhesive surfaces, and modulation envelope shaping.

5.7.2. Modulation Type Used

In general, the amplitude modulation scheme I used can be represented in the time domain by

$$(5.7.1) \qquad I_{total}(t) = [1 + m(t)]^{\gamma} c(t), \quad c(t) = A_c sin(2\pi f_c t)$$

where $I_{total}(t)$ is the output current of the amplifier, $m(t)$ is the desired bipolar modulation signal to be applied to the finger, and the carrier wave, $c(t)$, has amplitude A_c and frequency f_c. The parameter γ is a corrective factor used later, and for now $\gamma = 1$ simply yields double side-band full carrier (DSBFC) amplitude modulation. In this context, the instantaneous envelope of the carrier is $[1 + m(t)]$ and two limitations are placed upon the signal $m(t)$. Its frequency content must be limited to less than f_c, and its amplitude should be small enough to ensure that the envelope always remains positive. By additionally ensuring $f_c >> f_{RC}$, I am able to exploit the purely capacitive dynamic regime and disregard any transition zone effects.

An example of the raw data gathered from using this amplitude modulation approach is shown in Fig 5.4 and Fig 5.5. Here, the DLC system was actuated over 100s with 1Hz sinusoidal modulation and a 25kHz carrier ($\gamma = 1$). The raw voltage and current are shown in blue (Fig 5.4), revealing the slowly varying carrier wave, while the modulation is shown in orange, calculated from the analytic signal. Note the remarkable stability over time, and linearity of the voltage, given an applied current.

Shown in Fig. 5.5 is the resulting lateral force from the applied current, and the reading of the normal force sensor. Again note the stability of the 1Hz lateral force
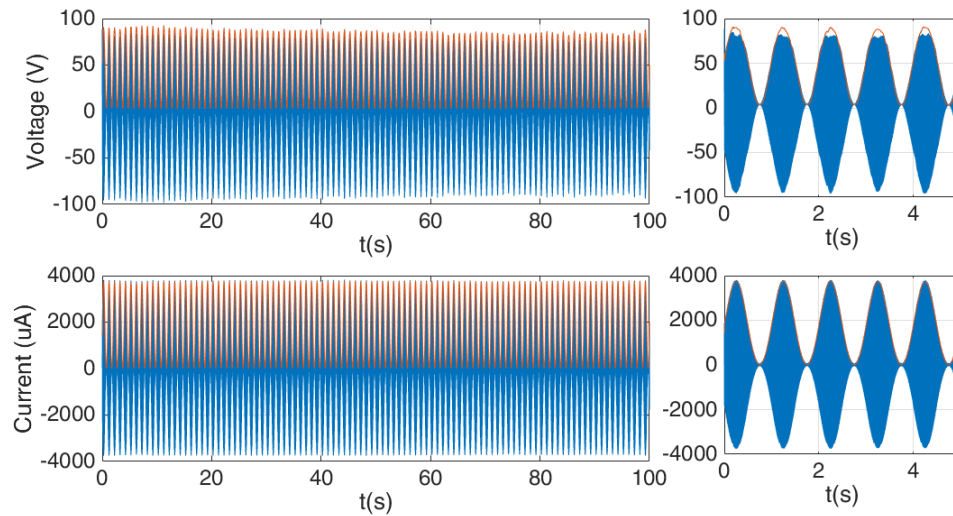
Figure 5.4. Voltage (top) and current (bottom) recordings during 100s of 1Hz sinusoidal modulation. The left shows the entire time course, while the right shows only the first 5 seconds.
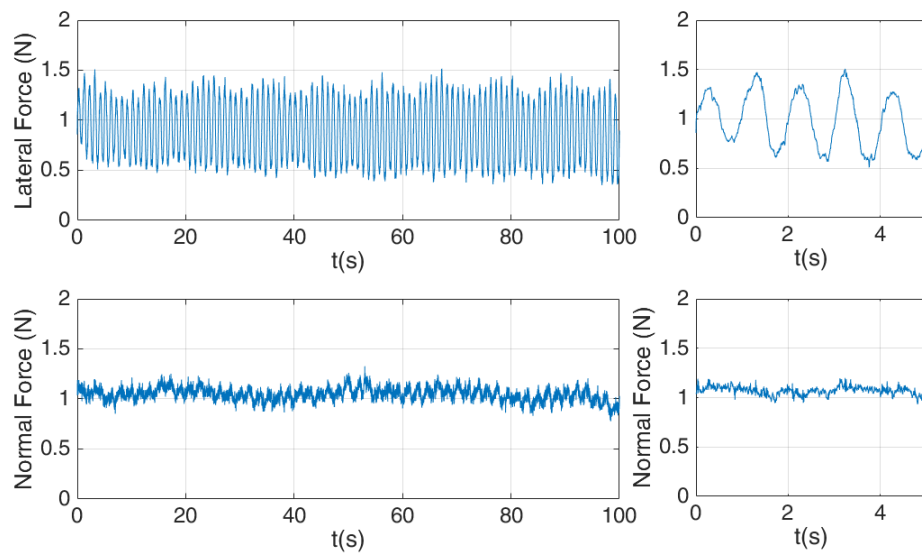
Figure 5.5. Lateral friction force (top) and applied normal force by the user (bottom). The left shows the entire time course, while the right shows only the first 5 seconds.

measurement, and small amount of deviations from 1N in the normal force measurement. With this robust experimental platform in place, one of the primary advantages to using amplitude modulation can be seen in the following experiment.

5.7.3. Sinusoidal Current to Force Magnitude Response

The modulation current to lateral force magnitude response of the 3M and DLC based electroadhesive systems using the modulation given by 5.7.1, $\gamma = 1$, is shown in Fig. 5.6.

Thirty logarithmically spaced modulation frequencies, 10 Hz to 10 kHz, were individually tested in a series of 10 trials. Frequency order was randomized within trials, and a 25 kHz carrier was sinusoidally modulated for 2 seconds, resulting in a 0-4 mA peak amplitude. A 4 mA maximum peak current was used to test the bandwidth of the system for large forces. The envelope of applied current was extracted using the analytic representation of the recorded current, found using the Hilbert transform. Peak current and lateral force magnitudes were computed using a digital lock-in technique and divided. The shaded regions represent $\pm\sigma$, while the solid dots and lines represent the trial means. As seen in Fig. 5.6, the current to force response is essentially flat throughout the entire measurement range for both the 3M and DLC coated surfaces. The peak and attenuation occurring around 6 kHz (denoted by the gray shaded region) is most likely a result of the force sensor's inherent resonance (shown in Fig. 5.1c) and is not believed to be reflective of the transduction process. In fact, there is little evidence or theory to suggest appreciable force attenuation above 6 kHz, as strong audio response is still recorded at higher modulation frequencies. Even greater bandwidth force measurements would be needed to test this hypothesis.
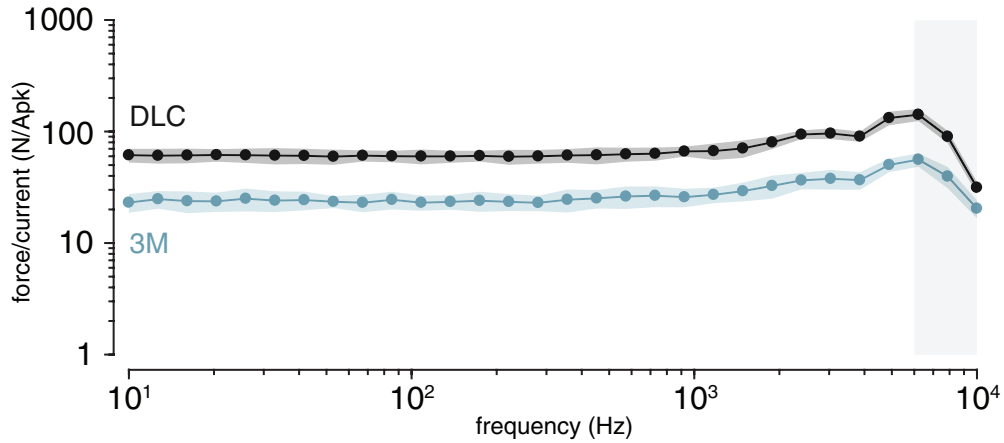
Figure 5.6. Current to lateral force magnitude response reveals a flat response throughout entire measurement range for both the 3M and DLC based systems (recorded at 4 mApk current and 1 N normal force). Each point is mean of 10 trials. The gray shaded region on the right denotes measurements past the resonance of the force sensing setup (included for reference, but may be ignored).

The dramatic difference between the bandwidth observed in Fig. 5.3 and Fig. 5.6 is a main advantage to using a modulated carrier approach. I am able to exploit the high frequency stability of the capacitive regime of operation in order to achieve a dynamically flat response. This, of course, does not come without some disadvantage, as the amount of applied current must be increased (approximately 2 orders of magnitude) in order to achieve the same gap voltage at higher frequency. The amount of overall real power dissipation, however, is still low, as the applied current is almost entirely capacitive, and is not electrically dissipated. Recycling this reactive current, for instance, could be an interesting topic for further research.

Finally, note that the lock-in technique analyzes only the first harmonic of each excitation frequency. While this is the largest force component measured, it does not say anything about the amount of harmonic or intermodulation distortion present. To look

at these effects, I examined the quasi-static envelope curves for each system, as well as what happens when more than one sinusoid is applied.

5.7.4. Quasi-static Transduction Curves

Representative quasi-static curves of total peak current versus measured lateral force for both 3M and DLC coated systems can be seen in Fig. 5.7. Carrier waves were sinusoidally modulated at 10 Hz for 30 seconds, yielding 300 traces of each curve. Little hysteresis was observed, and traces were binned and averaged. The shaded regions represent $\pm\sigma$, while the solid lines represent trace means.

The total peak current envelopes were computed as the magnitude of the analytic representation of measured current. Applied peak voltages remained below approximately 150 V, and a plot of voltage versus lateral force yielded the same shapes as Fig. 5.7, as the total system impedances remained essentially linear. The curves are offset due to normal kinetic friction, approximately 0.2 and 0.4 N for the 3M and DLC surface respectively. The additional lateral forces above these nominal friction levels are a result of the electroadhesion force, as described by equation 5.5.4.

As can be seen in Fig. 5.7, the current to force transduction curve is different in both shape and dynamic range for the 3M and DLC coated surfaces. The DLC coated surface appears to have a kinetic coefficient of friction that is approximately twice that of the 3M screen, which may contribute to the fact that the dynamic range of the lateral force is also approximately twice that of the 3M screen for the same amount of peak current.

This comparison, however, is difficult to make, as the DLC exhibits a strongly non-linear force behavior that cannot be captured by a simple power law. The force curve
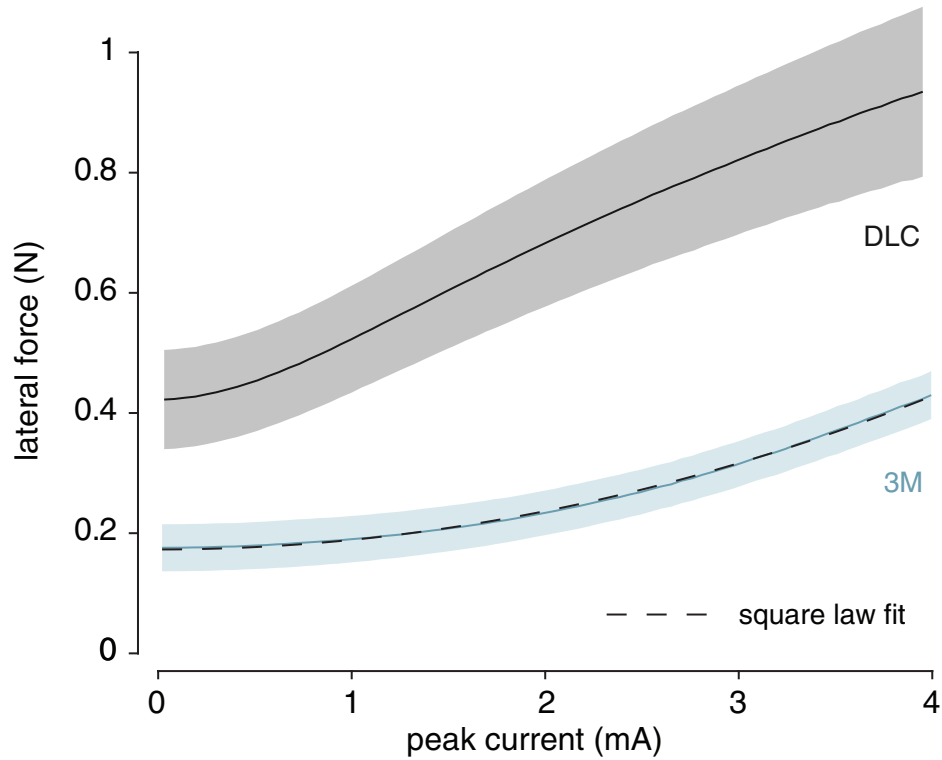
Figure 5.7. Recorded lateral force (N) versus peak current (mA), averaged over 30 seconds of 10 Hz sinusoidal modulation (1 N normal force). Data was binned and averaged. The solid lines represents the trace means, and the shaded regions denotes $\pm\sigma$. An offset square law, represented by a dashed line, can be fit to curve resulting from the 3M coated surface.

appears to be quadratic for low currents (<1mApk), but it quickly begins to level off and saturate. This behavior is not predicted by my force models, but it is speculated that it could be related to the exceptionally low roughness of the surface itself ($R_{RMS} = 35nm$). Further investigation into its origin is needed.

In contrast, the 3M coated surface (which has $R_{RMS} = 193nm$) exhibits behavior that is consistent with a square law based transduction model. An offset square law can be fit to the data quite well, and the linear scaling coefficient from this fit is within approximately a factor of 1.5 from the scaling constant used in Fig. 5.3. This is quite encouraging, as

these data were taken at different times, and using different frequencies and peak current amplitudes. This suggests that the additional lateral force due to electroadhesion may be able to be approximately predicted by monitoring the electrical impedance, similar to the method recently used in [**61**] with electroadhesive pucks. Further inquiry into this line of research, however, would be needed.

As a summary of Fig. 5.7, neither the 3M or DLC coated surfaces produce a pure sinusoidal output force given sinusoidal input modulation current; this is the very definition of the systems being non-linear. However, they do produce their first harmonic at the same frequency of the input modulation sinusoid, which is more than can be said for electroadhesive systems using a non-modulated approach. In fact, it is the addition of the DC offset to the modulation envelope (i.e. my restriction that the envelope function remain positive) that helps avoid frequency doubling distortion. Instead, the distortion comes from the shape of the transduction curves. Because of this fact, an additional envelope shaping step may be used to reduce distortion of the system further, if desired. This is illustrated in the following section.

5.7.5. Envelope Shaping & Broadband Harmonic Signals

In order to further inspect the current to force distortion characteristics of the system a modulation signal consisting of the sum of 10, 100, and 1,000 Hz sinusoids was used and the resulting force was measured. Each sinusoid had a relative amplitude of 1/3 in order for the overall envelope to be close to fully modulated, but non-negative. I chose this signal as a type of worst case distortion scenario.
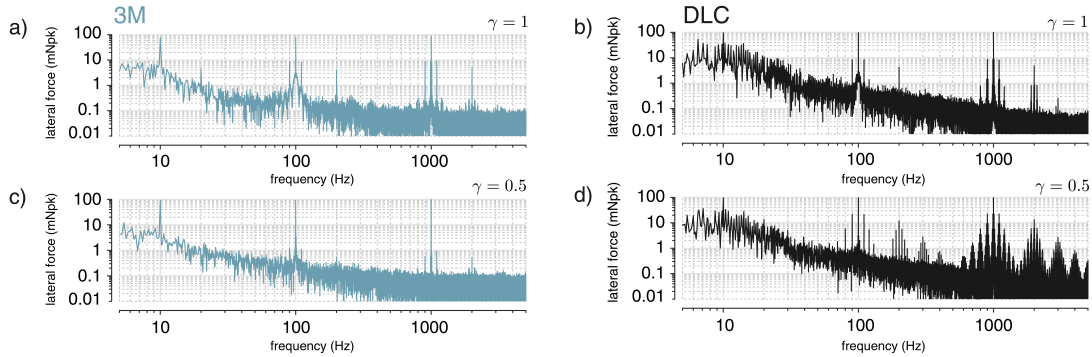
Figure 5.8. Magnitude spectra of the lateral force (mNpk) recorded from 10 seconds of a multi-harmonic sinusoidal modulation excitation for both the 3M (a and c) and DLC (b and d) coated surfaces. The modulation signal contained the sum of a 10 Hz, 100 Hz, and 1,000 Hz sinusoid, each at a relative amplitude of 1/3. On the top row (a and b), the shaping parameter $\gamma = 1$, resulting in normal DSBFC amplitude modulation. On the bottom row $\gamma = 0.5$, resulting in a square rooting of the modulation envelope. Distortion products are minimal in the case of the 3M coated surface with envelope correction applied.

The two surfaces and two values of the envelope shaping parameter γ were used. The peak carrier current amplitude was approximately 4 mA, and the carrier frequency was 25 kHz. Trials were 10 seconds long, and the magnitude of the discrete Fourier transform of the resulting lateral force signals are shown in Fig. 5.8. The 1/f shaped noise floor is assumed to come from non-electroadhesive phenomenon, and thus does not contain meaningful information here. The harmonic peaks above the noise are the components of interest.

For Fig. 5.8a and 5.8b $\gamma = 1$, resulting in typical DSBFC modulation as used in Fig. 5.6 and Fig. 5.7. Here the effect of the non-linear current-to-force transduction is clearly seen, as there is not only the intended harmonics at 10, 100, and 1,000 Hz, but second harmonics at 20, 200, and 2,000 Hz, and intermodulation products at intermediate frequencies such as 100±10 Hz, 1,000±100 Hz, etc. In each case, the intended harmonics

occur with approximately the same amplitude (as predicted by Fig. 5.6). The next largest frequency components are due to intermodulation distortion, approximately an order of magnitude down from my the intended forces. At an even lower amplitude are the second harmonic distortion components, and, for the case of the DLC coating, even a third harmonic of the 1,000 Hz component can be seen above the noise.

It remains to be seen whether this level of distortion is acceptable, or even perceptible, in tactile applications. It is, however, perceptible in audio applications. Because of this, I chose to additionally test my surfaces with $\gamma = 0.5$, exploiting the knowledge gained previously and preemptively shaping the modulation envelope using the square root function, which should then be inverted by the transduction process. The results of Fig. 5.7 predict that this envelope shape should work well for the 3M coated surface, which closely matches a square law, but not at all for the DLC coated surface, which has a transduction curve that is not easily modeled.

As seen in Fig. 5.8c, the square rooting of the modulation envelope had a dramatic effect on the distortion components, reducing all of them by an additional order of magnitude as compared to the $\gamma = 1$ case. Here I was able to reproduce this three harmonic signal with distortions in desired force around 1%. This type of DSBFC modulation with a shaped envelope appears to be a relatively simple way to achieve low-distortion and surprisingly linear behavior out of what is inherently a highly non-linear system.

Care must be taken, however, as the envelope shaping relies exclusively on knowing the correct inverting function. As can be seen in Fig. 5.8d, when a square root envelope was used with a system which does not obey a square law, the DLC coated surface, the resulting force spectrum was dramatically worse than the $\gamma = 1$ case. Efforts may be

made to model a different inverting function for this system, but it is not clear at this time if this behavior could be captured by a single stable function.

5.7.6. Broadband Arbitrary Force Spectra

As opposed to narrowband signals, such as those shown in Fig. 5.8, broadband signals should not introduce as much noticeable harmonic or intermodulation distortion. This is because the modulation index of each individual component in the broadband signal is small, and therefore remains in a locally linear portion of the overall quasi-static curve (similar to a small signal analysis argument). With this in mind, I also show how even the DLC electroadhesive system can be used to apply arbitrary broadband force spectra to the skin of the finger, Fig. 5.9. In this example, an illustrative broadband signal was constructed using bandpassed white noise. The signal was 60 seconds long, and contained the majority of its frequency content within the range of 500 to 1500 Hz, as seen by the spectrum $M(f)$ in Fig. 5.9a.

This signal was passed through the modulation process in the digital domain ($\gamma = 1$). A DC offset of 1.75 mA was applied in order to bias it into a middle portion of the quasi-static transduction curve (Fig. 5.7). It was then multiplied by a 25 kHz sinusoid, resulting in a signal with an envelope approximately ranging between 0 and 3.5 mApk. The signal was then reconstructed by the DAQ and converted to an applied current by the current controller. A measurement of the output current spectrum (shown in Fig. 5.9b) reveals the upper and lower sidebands of the applied signal, and the large 25 kHz carrier component.
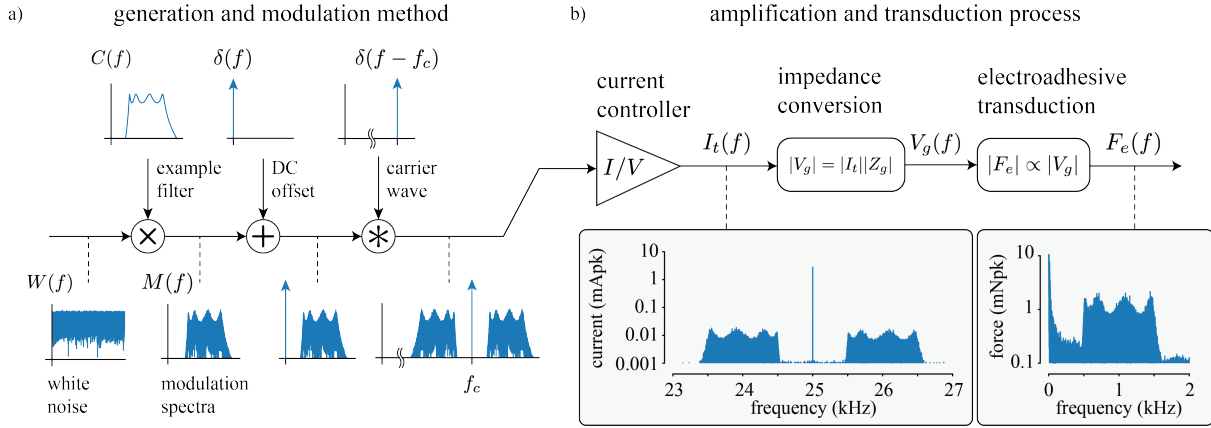
Figure 5.9. a) An illustrative broadband signal is generated by taking the spectrum of a white noise source, $W(f)$, and multiplying it by a Chebyshev type I bandpass filter, $C(f)$. The resulting spectrum, $M(f)$, contains broadband noise from 500-1500 Hz, and represents a desired modulation spectrum. A DC offset, $\delta(f)$, is added, and a sinusoidal carrier wave, $\delta(f - f_c)$, is convolved with the signal according to conventional DSBFC AM modulation. b) A custom current controller takes the desired current spectrum and applies it to the finger/DLC interface, as seen by a recorded plot of $I_t(f)$. This current induces a matching gap voltage spectrum according to the gap impedance. The electroadhesive transduction process converts the gap voltage to an additional applied force to the sliding finger. This process also serves to demodulate the signal, recovering the original desired spectrum, $M(f)$, as evidenced by the plot of measured additional lateral force.

The lateral force spectrum resulting from this current stimulation (also shown in Fig. 5.9b) shows the recovery of the original modulation spectrum, $M(f)$, from the demodulation performed by the transduction process. Note that the overall shape and relative magnitude of the modulation spectrum appear preserved throughout the entire process. This may be due to biasing the desired signal in the middle of the quasi-static transduction curve, and using a broadband spectra signal with small modulation indices. In this special case, an offset broadband signal, it is proposed that the square-law transduction may be suitably approximated by a purely linear relationship. The non-linearities of the

system, however, can still be revealed under other conditions, such as those discussed in previous sections.

5.8. Resulting Tactile, Audible, and Ultrasonic Vibrations

Thus far in my analysis I have restricted my mechanical measurements to the forces applied to the skin of the fingertip, as measured by the force ring and piezoelectric sensor. The manner in which this sensor is applied, however, effectively shunts the relatively low lateral impedance of the fingertip with the much higher impedance of the sensor, largely impeding vibration from developing and traveling up the finger. This is, of course, not how these surfaces are to be used in application, but only a useful tool for validation.

Now that I have verified a technique to apply low distortion and flat force profiles to the finger, I can release the finger from the force ring and observe vibrations as they would develop naturally. This yields a powerful tool for probing the unhindered dynamics of a finger sliding on a flat surface. To sense these vibrations I use two non-contact methods: a MEMS microphone to capture vibrations in the air, and a laser Doppler vibrometer (LDV) to record vibrations on and of the finger. The details of these instruments are given in previous sections, and the setup used for the following measurement is shown in Fig. 5.2.

To illustrate the extremely wide bandwidth capabilities of this modulation technique and hardware, a 10 second logarithmic chirp signal was applied to my finger. Its instantaneous frequency varied continuously from 10 Hz to 15,000 Hz. This modulation signal was applied to the 3M coated surface with $\gamma = 0.5$, a carrier frequency of 25 kHz, and a peak carrier amplitude of 4 mA. A 1 MΩ resistor was placed from the output of the amplifier
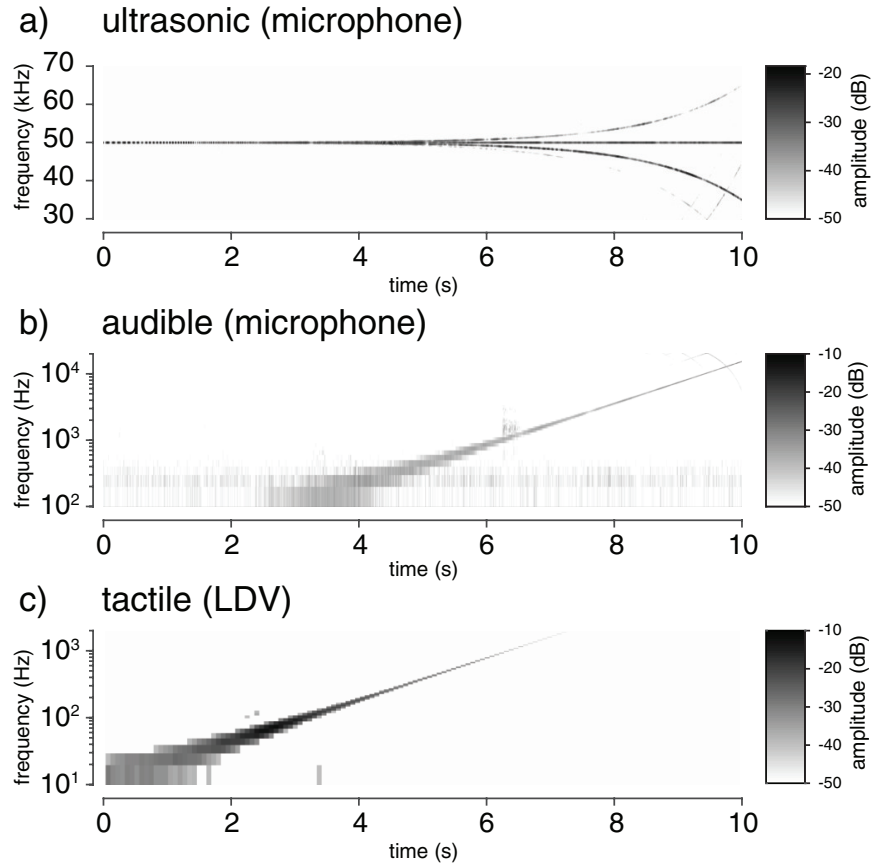
Figure 5.10. Spectrogram plots of vibrations on the skin and in the air resulting from 10s logarithmic chirp current modulation (10-15,000 Hz, $f_c = 25$ kHz, $\gamma = 0.5$). a) Ultrasonic Vibrations in the air are recorded as a by-product of the modulation process. b) Audible vibrations are heard and recorded emanating from the fingertip. c) Tactile vibrations are felt and recorded with the LDV.

to ground, once again to stabilize the DC impedance of the 3M screen. This resistor has minimal effect on the electrical system at 25 kHz, but ensures no charge build-up occurs on the plate at DC.

The data recorded is shown in Fig. 5.10 in the form of spectrograms, with different plots broken up into tactile, audible, and ultrasonic frequency ranges. The MEMS microphone was used for Fig. 5.10a and 5.10b, while the LDV response is shown in Fig. 5.10c.

The plots were created using a Hanning window function and 25% window overlap. Window lengths of 5ms, 10ms, and 100ms were used for the ultrasonic, audible, and tactile ranges respectively since the short time Fourier transform does not scale window length with frequency. Microphone and LDV response amplitudes were normalized by their peak value and the were thresholded at -50dB.

Beginning at 0 seconds, the chirp signal's instantaneous frequency is 10 Hz, and this produces a rectified vibration of the fingertip at that frequency. Also note the immediate response of the microphone at 50 kHz, twice the carrier frequency. This is the first direct evidence of ultrasonic ripple forces being applied to the skin using electroadhesion. As time progresses and the chirp's frequency increases, the single rectified harmonic vibration of the finger also increase. At approximately 3 seconds, the chirp is at about 100 Hz, and the rectified vibration is picked up in the air as well. The vibration on the skin increases further in frequency until approximately 1 kHz (and 6 seconds), where it then attenuates below the -50dB threshold. The microphone audible response, however, continues to increase. Looking at the ultrasonic ripple response, it clearly shows the upper and lower sidebands diverging from the center frequency as the modulation frequency becomes large with respect to the carrier. Finally, the audible and ultrasonic responses can be seen to continue all the way to the end of the chirp at 10 seconds. At this point there are 4 harmonics picked up by the microphone, at 15, 35, 50, and 65 kHz.

In this example I used an instantaneously narrowband signal in order to visualize how vibrations can be induced across an exceedingly large range of tactile, audible, and ultrasonic frequencies, with seemingly negligible amounts of harmonic distortion. With this modulation technique and hardware in place, however, it should be appreciated that

there is little hindering the excitation of the entire frequency spectrum at once with broadband force signals, as demonstrated by Fig. 5.8 and Fig. 5.9, which would result in broadband vibrations developing on the finger as well. Thus, my final research goal of developing a system which offers broadband and rich excitation of rapidly adapting tactile afferents is achieved.

5.9. Chapter Summary

The recordings and models reported here have several implications for surface haptic and audio-haptic displays. To begin, this current controlled, high frequency modulation technique can be readily applied to the entire frequency range of perceivable tactile forces (DC-1 kHz). As shown by Fig. 5.8, broadband force spectra can be easily applied to the finger, and envelope magnitude shaping may be employed to reduce harmonic and intermodulation distortion to levels seemingly on par with frictional noise. Therefore, I verify the assumption of previous research that electroadhesive based devices are well suited for high bandwidth tactile force rendering.

Additionally, my analysis reinforces the point that high performance hardware is needed if high performance, safe, and repeatable results are to be expected. For example, even if only a 1 kHz force bandwidth is desired, at least a 11 kHz carrier should be used so that the ripple forces don't leak into the audible frequency range and distract from user perception. At higher frequency, however, greater currents are needed to generate the same air gap voltage and force, which increases the risk of inadvertent electrocutaneous stimulation. The use of current control dramatically reduces this risk.

In the case of audio-tactile displays, initial measurements such as Fig. 5.10 show promising results. The frequency range of resulting vibrations is exceedingly large, and signals such as intelligible speech and musical song are able to be produced by the finger while remaining remarkably recognizable to the human ear. Achieving this fidelity, however, demands still higher performance hardware (f_c >20 kHz).

Further research into the current-to-audio transfer function characteristics should also be performed. Early microphone measurements in the acoustic near field suggest the resulting audio response may be relatively flat, but factors influencing the propagation of electroadhesive induced sound away from the fingertip have yet to be revealed. The impact of the acoustic properties of the contacting surface have also yet to be investigated.

As far as ultrasonic implications, it appears that the friction switching capabilities of electroadhesion, recently demonstrated by Mullenbach et al. [19], could possibly extend into the ultrasonic regime, as there appears to be considerable friction modulation capability at frequencies of 50 kHz and higher. This could lead to audibly silent active forcing of the finger, which would expand the practical capabilities of surface haptic devices in an intriguing new direction.

Finally, the insights given by the air gap impedance based force model and discussion not only led to the experiments and conclusions above, but offer up a research direction for electroadhesive friction modulation focused squarely on the design and optimization of the skin/surface interface, reinforcing the summary from Chapter 4. Questions that remain to be answered include: How might the charge accumulation or intensity of the electric field in the gap be maximized? How can the surface geometry and material optimize the amount of friction force for the same applied electroadhesive normal force?

What limits the amount of applied gap voltage, or what might lead to its collapse or degradation? Answers to these questions would not only lead to better surface haptic displays, but would also yield to a better understanding of the physics behind the 140 years of electroadhesive observations.

CHAPTER 6

Conclusions & Future Work

In this conclusion, I restate the original questions posed in the introduction of this dissertation, and examine the answers that my work suggests. I also offer several concrete application areas in which the research presented here may be extended, and include example measurement techniques, preliminary data, and an integrated electroadhesive interface I have already developed.

6.1. Original Research Questions

I'd like to return to the original questions I posed in the introduction, and reinspect them in light of my work. They were:

(1) What is the direct origin of the transduction from an electrical voltage to a mechanical force in these finger based systems, i.e. what voltage (or charge) and where, creates an effective increase in frictional force?

(2) What factors affect how an applied voltage (or current) by some external source results in this effective voltage?

The answer to question one now seems much more concrete than before. My work provides strong evidence that it is the voltage (or charge) at the edges of an interfacial air gap that serve to increase friction on the skin. This explanation seems to work for the majority of known electroadhesive observations, and can generally explain my own observations, whereas other models cannot.

Furthermore, this interface can somewhat be modeled by a Columbic kinetic friction model (friction force proportional to applied load), with the electroadhesive force at the interface acting as an effective applied normal force. This is a large step forward in understanding the origin of the transduction, however, as alluded to below, future work may be done to illuminate this question further. I characterize what I have defined so far as an effective working model, one that is only as complex as it needs to be to explain the observed behavior so far, not one that is absolute ground truth. The quasi-static behavior of the DLC surface in Fig. 5.7, for instance, it not explained by the current working model.

The majority of the second question is answered quite concretely in Chapter 4. There are various system impedances that play a role in the mapping of an applied excitation to gap voltage, many of which I examined in detail. These impedances, such as that of the surface coating, grounding condition, skin, and body, can be quantified and examined easily, and their effects are (relatively) straightforward. However, the part of question two that still remains is this: *what creates the gap impedance (or perhaps what shorts it out) in the first place?* My work offers some suggestions, but has not been able to examine this suggestions scientifically. I believe analysis of the origin and influence of external factors on the gap impedance would be incredibly useful for designing the next generation of electroadhesive displays.

6.2. High Fidelity Variable Friction

As shown in Chapter 5, electroadhesion can be effectively controlled to create the highest bandwidth variable friction devices to date, with striking linearity. This ability

may lead to new practical texture displays that are able to reproduce fine textural details of virtual textures better than ever before. The exceptional speed of the effect also lends itself to closed-loop lateral force control of variable friction displays, an area which is only recently being considered.

It appears, therefore, that the problem of variable friction system bandwidth is mostly solved, and future research of high fidelity variable friction actuation may focus on increasing the dynamic range of friction (possibly by combining electroadhesion and ultrasonic effects, or engineering a new electroadhesive surface coating), and reproducing spatial variations of friction force *within* the fingerpad itself (possibly using small electrodes, and controlling them with more complex driving electronics). Each of these would appear, at this time, to offer a large benefit in the perceptual gamut of variable friction displays, and represent areas of research that have yet to really be explored.

6.3. Ultrasonic Active Forcing

As shown in Chapter 3, the electroadhesive effect is capable of very large force magnitudes (under the right conditions). I was able to increase the frictional force on my finger by 2N (an effective normal force of 7N). This ability, to harness and control large magnitude friction forces, has already enabled the development of active forcing friction devices [19] using the concept of an electroadhesive friction switch. Moving this line of research forward, however, requires even higher performance surfaces and electrical driving schemes. A main challenge of active forcing is moving the fingertip switching frequency into the ultrasonic range, something that Chapter 5 seems to strongly suggests

is attainable. The model and characterization methods in Chapter 4 can be used to characterize new candidate surfaces, and the electrical hardware developed may be extended to yet even higher performance standards. Indeed, it would appear that the only way ultrasonic active forcing will be practically attainable is through the development of new electroadhesive surfaces and driving methods extended from this line of research.

6.4. Mechanical Characterization of the Finger

Because the system I developed in Chapter 5 can apply purely sinusoidal friction forces to the finger in a relatively controlled manner, it can be used to linearly probe various aspects of finger and fingertip mechanics, such as effective fingertip admittances. As an example of this, I can take the data presented in Fig. 5.10 and view it in a different manner than the spectrogram. If I instead simply compute the transfer function from applied voltage squared to resulting vibrations, the overall vibration dynamic can be seen, Fig. 6.1. In these plots, I computed the magnitude spectra of the total voltage squared, which can be done by squaring the signal in the time domain, and taking the DFT (e.g. $\mathfrak{F}\{v_{total}(t)^2\}$), or can be found using the auto-convolution (or auto-correlation since the recorded data is guaranteed to have Hermitian symmetry) of the total voltage spectra, (e.g. $|V_{total}(f) * V_{total}(f)| = |V_{total}(f) \star V_{total}(f)|$). I used the latter method here.

Performing this calculation gives an approximation of the applied force spectrum to the finger, as it was previously shown that applied force has a flat correlation with total applied voltage/current (in the capacitive regime). I then divided the spectra of LDV response and microphone response by the total applied voltage squared spectrum, generating a transfer function.
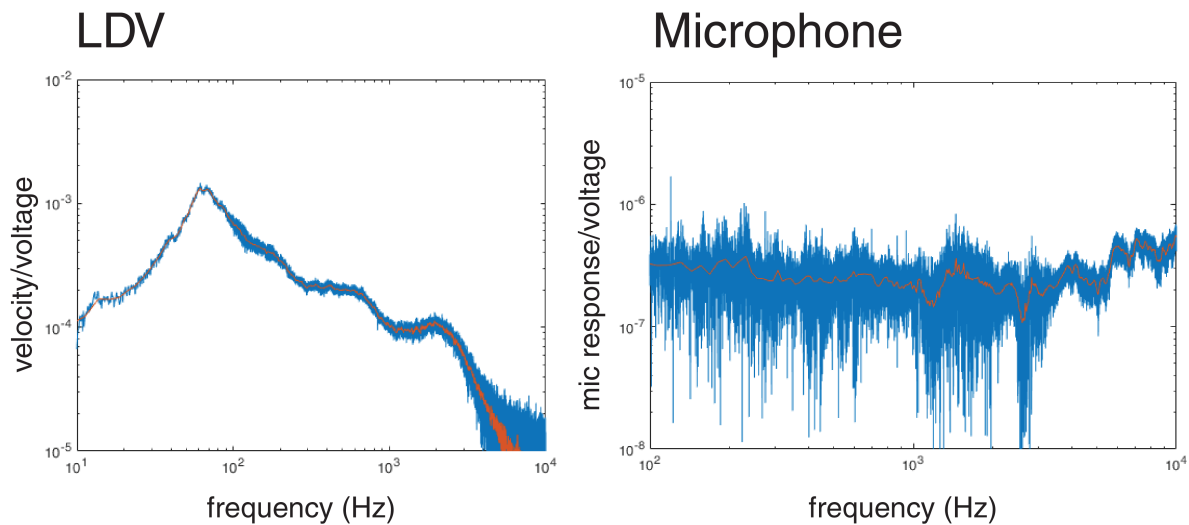
Figure 6.1. Spectra of vibrations captured and shown in Fig. 5.10, which have then been divided by the spectra of the total applied voltage squared. The blue traces are the raw spectra, while the orange traces have been binned and averaged in frequency.

Looking at Fig. 6.1 (left), one can interpret the transfer function as an effective mechanical admittance curve, with a few notable resonances. Here the overall magnitude scale is not calibrated, so only the shape is considered. The largest resonance is evidenced by an 20 dB increase in admittance around 70 Hz, which appears consistent with rigid motion of the entire finger. Also note the dramatic decrease in admittance past 2 kHz, suggesting that little motion happens on the skin past this frequency. Could this be related to the tactile sensing system not responding much past 1 kHz as well? Further study could investigate this question.

Turning to the microphone audible range transfer function Fig. 6.1 (right), the shape is remarkably flat. This, however, may be due to the fact that the microphone was placed in the acoustic near field for these wavelengths, and, as such, none of the propagation dynamics are taken into account. Regardless, this plot is quite encouraging, and begs the

question of what part of the skin or finger is vibrating exactly to generate this acoustic response in the air? Do these types of acoustic vibrations develop during normal tactile exploration as well, and do we perceptually integrate this information?

The answers to some of the questions posed above could have implications for the neuroscience and pyschophysics of texture going forward, and could possibly be found using the force modulation technique developed here.

6.5. Origin of Skin Friction, Electroadhesive and Otherwise

The implications of the interfacial gap impedance (with regards to friction) extend beyond the electroadhesive effect. The impedance exists with or without significant electrical excitation, and can inform future models of fingertip friction as a whole. For example, early evidence points to a correlation between interfacial gap impedance and real area of contact seen via FTIR imaging (a technique demonstrated recently by [**62**] [**63**]), meaning Z_{gap} could be a good proxy for a measure of integrated real area of contact. This evidence is presented in Fig. 6.2 and Fig. 6.3.

Fig. 6.2a shows a still image taken from a video of my finger as it is sliding and stopping on the 3M surface. The shot is looking directly at the contact patch of the finger through the glass substrate, and illuminated with a red laser source. The glowing of the patch is primarily due to the FTIR effect. The video was masked by an ellipse (as shown in Fig. 6.2b), and the masked intensity of red pixels was integrated over each frame. The results of this calculation was then inverted, to give the inverse intensity value plotted in time, Fig. 6.2c.
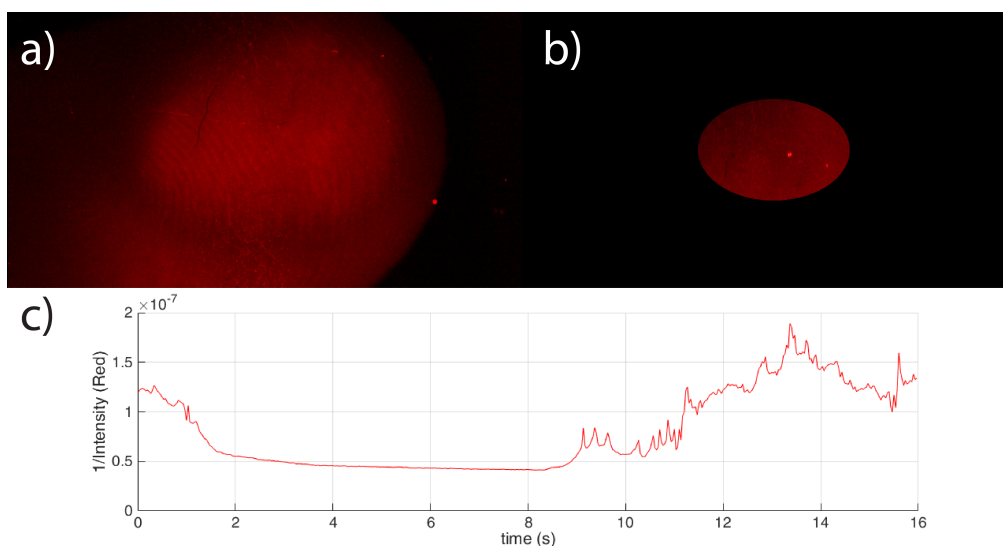
Figure 6.2. FTIR images taken of the fingertip contact patch, either a) raw frame, or b) frame masked by an ellipse for processing. Part c) shows the inverse integrated intensity over time of the red pixel channel of the video. Data collected during sliding and stopping of the finger.
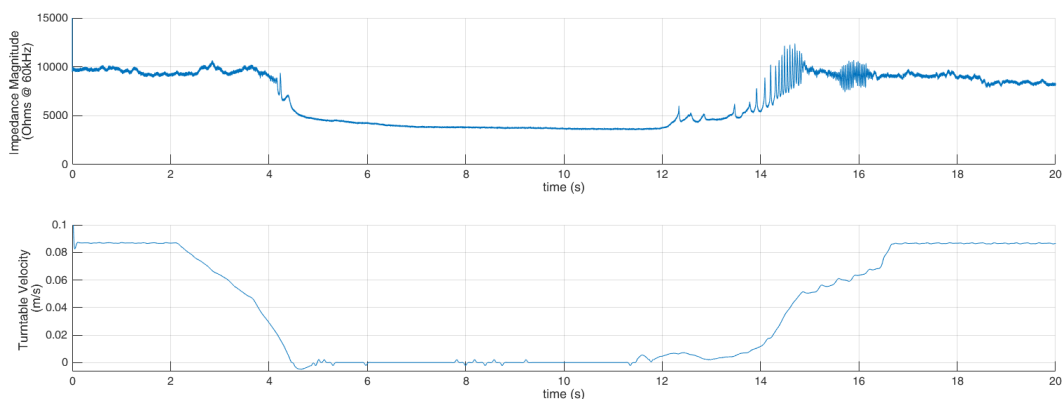
Figure 6.3. Electrical impedance magnitude recorded using a 60 kHz low amplitude current (top) and the velocity of the turntable (bottom) recorded during the video recording of the contact patch. Data collected during sliding and stopping of the finger.

This processing was performed so that the FTIR data may be compared to the data in Fig. 6.3. In this figure, both the electrical impedance (top) and velocity of the rotational

platform (bottom) are shown. The electrical impedance was recorded using a $\pm 10\mu A$ sinusoidal current at 60kHz

Although the time scales have not been lined up between the data in Fig. 6.2 and Fig. 6.3, the correlation between all of the time records is still clear. The turntable starts off at a constant velocity, then ramps down and stops. During this transition both the electrical impedance and inverse contact patch intensity drop, with very similar characteristic time constants. Once the table starts again, both the impedance and inverse intensity show transient behaviors that appear qualitatively correlated. If expanded upon in more detail, this correlation could be used in future studies to elucidate the nature of fingertip friction, or to estimate area of contact in real-time during usage, expanding the usefulness of the techniques and measurements shown here to a wider scientific audience.

6.6. Human Computer Interaction Design

The combination of acoustic and tactile actuation of the finger, though not mentioned much in this thesis, does have interesting implications for interaction design. In this context, the ability to turn the finger into a controlled audio-tactile source could potentially make for incredibly engaging and realistic multimodal interactions.

As a first step in this research direction I envisioned and built an audio-visual-tactile platform named Tactile Soundboard. The general idea behind this interface platform can be seen in Fig. 6.4, where a virtual violin is depicted as being struck by the user's finger. The details of this interface's construction and some prototyped demonstrations are given in Appendix A, but I would also like to highlight a unique characteristic of the combined acoustic-touch paradigm I've developed.
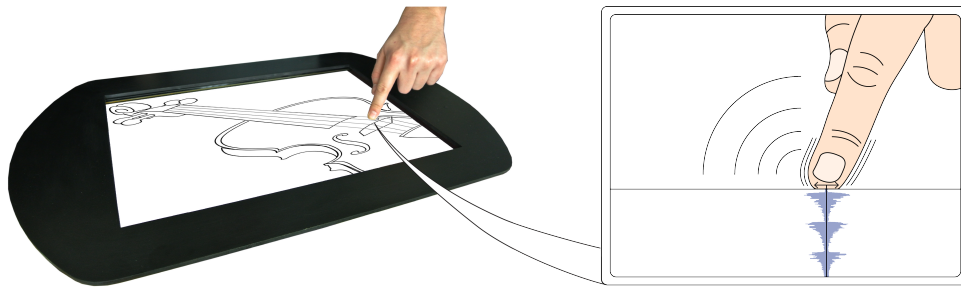
Figure 6.4. Tactile Soundboard renders high-bandwidth audio-tactile feedback directly to the finger via broadband electroadhesion. Depicted is a user directly plucking a virtual violin. Tactile feedback is felt directly on the finger, while audio feedback is heard emanating from the skin.

As depicted in Fig 6.5, Tactile Soundboard provides a mapping between input and output that is consistent across modalities and focused at a single location, the tip of the finger, at a specific point in time. This technique extends the direct touch input and visual output paradigm found in everyday smartphone, tablet, and tabletop interfaces to include continuous and direct audio-tactile output at the finger. The real power in this mapping configuration, as I see it, stems from the sense of directness that is achieved between the user and system. This directness comes from the feeling that there is little ambiguity between what the user intends to achieve, and how the system is able to interpret that intention [64]. Another way of saying this is that a product or interface is perceived to be direct if the user is readily able to transverse the gulfs of execution and evaluation during interaction [65], and one way to reduce these cognitive gulfs is through the use of intuitive mapping between user input and system output.

With this principle in mind, Tactile Soundboard (and any high bandwidth electroadhesive technique) is poised to take advantage of two established principles of multisensory neural processing and perception: spatial coincidence and temporal overlap [66]. Because the feedback is generated at and on the fingertip itself, it is inherently spatially

inputs
position
time

user

system **outputs**
force   sound
vibration image
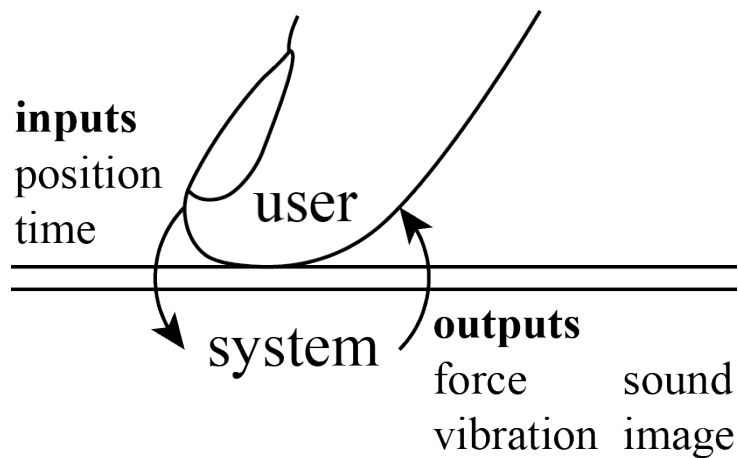
Figure 6.5. Multisensory feedback loop of inputs and outputs, centered around the finger at the point of interaction.

localized and temporally synchronous, two factors that strongly influence multisensory integration at a fundamental, neuronal level. Future studies could possibly exploit this characteristic to create the most direct, realistic, and engaging touch screen based interfaces to-date. Furthermore, because the feedback actuation is so generalized, the ways in which the acoustic-tactile feedback can be structured may lead to exceedingly varied and wide-reaching applications. Categorizing and determining which applications are the most promising, therefore, could save future interaction designers precious time and effort.

6.7. Final Remarks

I hope that at this point I have successfully persuaded any readers of my dissertation that the future of finger based electroadhesion is bright, and that those working in the field (myself included) have only just scratched the surface of what is possible with the effect, pun intended. Looking back to where my understanding of the effect was as I began my research, I very much felt like Gray, Johnsen, Rahbek, Mallinckrodt, and others, who

noticed a peculiar effect with their fingers and felt compelled to investigate it further. Lucky for me, technology and electronics have improved vastly in the last century and a half, and now real progress can be made in understanding and controlling the effect (as demonstrated in previous chapters).

What also strikes me as lucky is to be able to investigate electroadhesion at this particular point is time. While no practical application for the effect seemed to exist during previous researchers' lifetimes, I must reiterate the fact that this is not the case as I write this. Our everyday lives are being taken over more and more by touchscreen driven interactions, and I believe elecroadhesion could truly have a part to play in increasing the effectiveness and enjoyability of these interfaces.

This is perhaps why I spent such a great deal of effort on a demonstration interface such as Tactile Soundboard; I sought to convey the import of high fidelity and acoustic range forces and vibrations to those around me. Nonetheless, I've probably overreached myself, as there is still much to be investigated and understood about broadband electroadhesion as it is applied to human fingers. I hope what is documented here is one small step in that direction, and that it encourages others to follow and take heed of the insights I have gained along the way.

References

[1] G. B. Prescott, *The speaking telephone, talking phonograph, and other novelties.* New York: D. Appleton & Company, 1878.

[2] J. Linjama and V. Mäkinen, "E-sense screen: Novel haptic display with capacitive electrosensory interface," *HAID*, vol. 9, pp. 10–11, 2009.

[3] O. Bau, I. Poupyrev, A. Israr, and C. Harrison, "TeslaTouch: electrovibration for touch surfaces," in *Proceedings of the 23nd annual ACM symposium on User interface software and technology*, UIST '10, (New York, NY, USA), pp. 283–292, ACM, 2010.

[4] L. Winfield, J. Glassmire, J. E. Colgate, and M. Peshkin, "T-PaD: Tactile Pattern Display through Variable Friction Reduction," in *EuroHaptics Conference, 2007 and Symposium on Haptic Interfaces for Virtual Environment and Teleoperator Systems. World Haptics 2007. Second Joint*, pp. 421 –426, Mar. 2007.

[5] M. Biet, F. Giraud, and B. Lemaire-Semail, "Squeeze film effect for the design of an ultrasonic tactile plate," *IEEE Transactions on Ultrasonics, Ferroelectrics, and Frequency Control*, vol. 54, pp. 2678–2688, Dec. 2007.

[6] E. Vezzoli, W. B. Messaoud, M. Amberg, F. Giraud, B. Lemaire-Semail, and M. A. Bueno, "Physical and Perceptual Independence of Ultrasonic Vibration and Electrovibration for Friction Modulation," *IEEE Transactions on Haptics*, vol. 8, pp. 235–239, Apr. 2015.

[7] V. Levesque, L. Oram, K. MacLean, A. Cockburn, N. D. Marchuk, D. Johnson, J. E. Colgate, and M. A. Peshkin, "Enhancing Physicality in Touch Interaction with Programmable Friction," in *Proceedings of the SIGCHI Conference on Human Factors in Computing Systems*, CHI '11, pp. 2481–2490, ACM, 2011.

[8] S.-C. Kim, A. Israr, and I. Poupyrev, "Tactile Rendering of 3d Features on Touch Surfaces," in *Proceedings of the 26th Annual ACM Symposium on User Interface Software and Technology*, UIST '13, (New York, NY, USA), pp. 531–538, ACM, 2013.

[9] D. Meyer, M. Wiertlewski, M. Peshkin, and J. Colgate, "Dynamics of ultrasonic and electrostatic friction modulation for rendering texture on haptic surfaces," in *2014 IEEE Haptics Symposium (HAPTICS)*, pp. 63–67, Feb. 2014.

[10] J. Mullenbach, C. Shultz, J. E. Colgate, and A. M. Piper, "Exploring Affective Communication Through Variable-friction Surface Haptics," in *Proceedings of the 32Nd Annual ACM Conference on Human Factors in Computing Systems*, CHI '14, pp. 3963–3972, ACM, 2014.

[11] A. Israr, O. Bau, S.-C. Kim, and I. Poupyrev, "Tactile Feedback on Flat Surfaces for the Visually Impaired," in *CHI '12 Extended Abstracts on Human Factors in*

Computing Systems, CHI EA '12, (New York, NY, USA), pp. 1571–1576, ACM, 2012.

[12] O. Bau and I. Poupyrev, "REVEL: Tactile Feedback Technology for Augmented Reality," *ACM Trans. Graph.*, vol. 31, pp. 89:1–89:11, July 2012.

[13] D. Meyer, M. Peshkin, and J. Colgate, "Fingertip friction modulation due to electrostatic attraction," in *World Haptics Conference (WHC), 2013*, pp. 43–48, 2013.

[14] G. Ilkhani, M. Aziziaghdam, and E. Samur, "Data-Driven Texture Rendering on an Electrostatic Tactile Display," *International Journal of Human–Computer Interaction*, vol. 0, pp. 1–15, Jan. 2017.

[15] Y. Vardar, B. Guclu, and C. Basdogan, "Effect of Waveform on Tactile Perception by Electrovibration Displayed on Touch Screens," *IEEE Transactions on Haptics*, vol. PP, no. 99, pp. 1–1, 2017.

[16] J. Kang, H. Kim, S. Choi, K. D. Kim, and J. Ryu, "Investigation on Low Voltage Operation of Electrovibration Display," *IEEE Transactions on Haptics*, vol. PP, no. 99, pp. 1–1, 2017.

[17] H. Zophoniasson, C. Bolzmacher, M. Anastassova, and M. Hafez, "Electrovibration: Influence of the applied force on tactile perception thresholds," in *2017 Zooming Innovation in Consumer Electronics International Conference (ZINC)*, pp. 70–73, May 2017.

[18] E. Vezzoli, M. Amberg, F. Giraud, and B. Lemaire-Semail, "Electrovibration Modeling Analysis," in *Haptics: Neuroscience, Devices, Modeling, and Applications*, pp. 369–376, Springer, Berlin, Heidelberg, June 2014.

[19] J. Mullenbach, M. Peshkin, and J. E. Colgate, "eShiver: Lateral Force Feedback on Fingertips through Oscillatory Motion of an Electroadhesive Surface," *IEEE Transactions on Haptics*, vol. 10, pp. 358–370, July 2017.

[20] E. Gray, "Improvement in electric telegraphs for transmitting musical, tones," July 1875. Cooperative Classification H04L27/26.

[21] A. Johnsen and K. Rahbek, "A physical phenomenon and its applications to telegraphy, telephony, etc.," *Journal of the Institution of Electrical Engineers*, vol. 61, pp. 713–725, July 1923.

[22] E. Mallinckrodt, A. L. Hughes, and W. Sleator, "Perception by the Skin of Electrically Induced Vibrations," *Science*, vol. 118, no. 3062, pp. 277–278, 1953.

[23] S. Grimnes, "Electrovibration, cutaneous sensation of microampere current," *Acta Physiologica Scandinavica*, vol. 118, no. 1, pp. 19–25, 1983.

[24] L. D. Hartsough, "Electrostatic wafer holding," *Solid State Technology*, vol. 36, pp. 87–91, Jan. 1993.

[25] G. J. Monkman, "An Analysis of Astrictive Prehension," *The International Journal of Robotics Research*, vol. 16, pp. 1–10, Feb. 1997.

[26] H. Prahlad, R. Pelrine, S. Stanford, J. Marlow, and R. Kornbluh, "Electroadhesive robots #x2014;wall climbing robots enabled by a novel, robust, and electrically controllable adhesion technology," in *2008 IEEE International Conference on Robotics and Automation*, pp. 3028–3033, May 2008.

[27] R. M. Strong and D. E. Troxel, "An Electrotactile Display," *IEEE Transactions on Man-Machine Systems*, vol. 11, pp. 72–79, Mar. 1970.

[28] D. J. Beebe, C. M. Hymel, K. A. Kaczmarek, and M. E. Tyler, "A polyimide-on-silicon electrostatic fingertip tactile display," in *Proceedings of 17th International Conference of the Engineering in Medicine and Biology Society*, vol. 2, pp. 1545–1546 vol.2, Sept. 1995.

[29] H. Tang and D. J. Beebe, "A microfabricated electrostatic haptic display for persons with visual impairments," *IEEE transactions on rehabilitation engineering: a publication of the IEEE Engineering in Medicine and Biology Society*, vol. 6, pp. 241–248, Sept. 1998.

[30] A. Agarwal, K. Nammi, K. Kaczmarek, M. Tyler, and D. Beebe, "A hybrid natural/artificial electrostatic actuator for tactile stimulation," in *Microtechnologies in Medicine amp; Biology 2nd Annual International IEEE-EMB Special Topic Conference on*, pp. 341–345, 2002.

[31] K. A. Kaczmarek, K. Nammi, A. K. Agarwal, M. E. Tyler, S. J. Haase, and D. J. Beebe, "Polarity effect in electrovibration for tactile display," *IEEE transactions on bio-medical engineering*, vol. 53, pp. 2047–2054, Oct. 2006.

[32] J. A. Greenwood and J. B. P. Williamson, "Contact of nominally flat surfaces," *Proc. R. Soc. Lond. A*, vol. 295, pp. 300–319, Dec. 1966.

[33] J. A. Greenwood, "Constriction resistance and the real area of contact," *British Journal of Applied Physics*, vol. 17, p. 1621, Dec. 1966.

[34] A. D. Stuckes, "Some theoretical and practical considerations of the Johnsen-Rahbek effect," *Proceedings of the IEE - Part B: Radio and Electronic Engineering*, vol. 103, pp. 125–131, Mar. 1956.

[35] R. Atkinson, "A simple theory of the Johnsen-Rahbek effect," *Journal of Physics D: Applied Physics*, vol. 2, p. 325, Mar. 1969.

[36] C. Balakrishnan, "Johnsen-Rahbek Effect with an Electronic Semi-Conductor," *British Journal of Applied Physics*, vol. 1, p. 211, Aug. 1950.

[37] T. Watanabe and T. Kitabayashi, "Effect of Additives on the Electrostatic Force of Alumina Electrostatic Chucks," *Journal of the Ceramic Society of Japan*, vol. 100, no. 1157, pp. 1–6, 1992.

[38] S. Kanno and T. Usui, "Generation mechanism of residual clamping force in a bipolar electrostatic chuck," *Journal of Vacuum Science & Technology B*, vol. 21, pp. 2371–2377, Nov. 2003.

[39] S. Kanno, K. Kato, K. Yoshioka, R. Nishio, and T. Tsubone, "Prediction of clamping pressure in a Johnsen-Rahbek-type electrostatic chuck based on circuit simulation," *Journal of Vacuum Science & Technology B*, vol. 24, pp. 216–223, Jan. 2006.

[40] S. Qin and A. McTeer, "Wafer dependence of Johnsen–Rahbek type electrostatic chuck for semiconductor processes," *Journal of Applied Physics*, vol. 102, p. 064901, Sept. 2007.

[41] T. Watanabe, T. Kitabayashi, and C. Nakayama, "Electrostatic Force and Absorption Current of Alumina Electrostatic Chuck," *Japanese Journal of Applied Physics*, vol. 31, p. 2145, July 1992.

[42] T. Yamamoto and Y. Yamamoto, "Analysis for the change of skin impedance," *Medical and Biological Engineering and Computing*, vol. 15, pp. 219–227, May 1977.

[43] Y. Yamamoto and T. Yamamoto, "Characteristics of skin admittance for dry electrodes and the measurement of skin moisturisation," *Medical and Biological Engineering and Computing*, vol. 24, pp. 71–77, Jan. 1986.

[44] S. Derler, L. C. Gerhardt, A. Lenz, E. Bertaux, and M. Hadad, "Friction of human skin against smooth and rough glass as a function of the contact pressure," *Tribology International*, vol. 42, pp. 1565–1574, Dec. 2009.

[45] T. Yamamoto and Y. Yamamoto, "Dielectric constant and resistivity of epidermal stratum corneum," *Medical and biological engineering*, vol. 14, pp. 494–500, Sept. 1976.

[46] "IEEE Standard for Safety Levels With Respect to Human Exposure to Electromagnetic Fields, 0-3 kHz," *IEEE Std C95.6-2002*, pp. 1–0, Oct. 2002.

[47] "IEEE Standard for Safety Levels with Respect to Human Exposure to Radio Frequency Electromagnetic Fields, 3 kHz to 300 GHz," *IEEE Std C95.1-2005 (Revision of IEEE Std C95.1-1991)*, pp. 1–238, Apr. 2006.

[48] S. Grimnes and O. G. Martinsen, *Bioimpedance and Bioelectricity Basics*. Academic Press, Aug. 2014.

[49] B. Hirschorn, M. E. Orazem, B. Tribollet, V. Vivier, I. Frateur, and M. Musiani, "Constant-Phase-Element Behavior Caused by Resistivity Distributions in Films II. Applications," *Journal of The Electrochemical Society*, vol. 157, pp. C458–C463, Dec. 2010.

[50] R. S. Johansson and J. R. Flanagan, "Coding and use of tactile signals from the fingertips in object manipulation tasks," *Nature Reviews Neuroscience*, vol. 10, pp. 345–359, May 2009.

[51] H. P. Saal, X. Wang, and S. J. Bensmaia, "Importance of spike timing in touch: an analogy with hearing?," *Current Opinion in Neurobiology*, vol. 40, pp. 142–149, Oct. 2016.

[52] A. I. Weber, H. P. Saal, J. D. Lieber, J.-W. Cheng, L. R. Manfredi, J. F. Dammann, and S. J. Bensmaia, "Spatial and temporal codes mediate the tactile perception of natural textures," *Proceedings of the National Academy of Sciences*, vol. 110, pp. 17107–17112, Oct. 2013.

[53] D. J. Meyer, M. A. Peshkin, and J. E. Colgate, "Tactile Paintbrush: A procedural method for generating spatial haptic texture," in *2016 IEEE Haptics Symposium (HAPTICS)*, pp. 259–264, Apr. 2016.

[54] L. R. Manfredi, H. P. Saal, K. J. Brown, M. C. Zielinski, J. F. Dammann, V. S. Polashock, and S. J. Bensmaia, "Natural scenes in tactile texture," *Journal of Neurophysiology*, vol. 111, pp. 1792–1802, May 2014.

[55] E. L. Mackevicius, M. D. Best, H. P. Saal, and S. J. Bensmaia, "Millisecond precision spike timing shapes tactile perception," *The Journal of Neuroscience: The Official Journal of the Society for Neuroscience*, vol. 32, pp. 15309–15317, Oct. 2012.

[56] M. A. Harvey, H. P. Saal, J. F. D. Iii, and S. J. Bensmaia, "Multiplexing Stimulus Information through Rate and Temporal Codes in Primate Somatosensory Cortex," *PLOS Biology*, vol. 11, p. e1001558, May 2013.

[57] M. Wiertlewski, D. Leonardis, D. J. Meyer, M. A. Peshkin, and J. E. Colgate, "A High-Fidelity Surface-Haptic Device for Texture Rendering on Bare Finger," in *Haptics: Neuroscience, Devices, Modeling, and Applications*, pp. 241–248, Springer Berlin Heidelberg, June 2014. DOI: 10.1007/978-3-662-44196-1_30.

[58] M. Wiertlewski and J. E. Colgate, "Power Optimization of Ultrasonic Friction-Modulation Tactile Interfaces," *IEEE Transactions on Haptics*, vol. 8, pp. 43–53, Jan. 2015.

[59] M. Wiertlewski and V. Hayward, "Mechanical behavior of the fingertip in the range of frequencies and displacements relevant to touch," *Journal of Biomechanics*, vol. 45, pp. 1869–1874, July 2012.

[60] T. Soneda and K. Nakano, "Investigation of vibrotactile sensation of human fingerpads by observation of contact zones," *Tribology International*, vol. 43, pp. 210–217, Jan. 2010.

[61] T. Nakamura and A. Yamamoto, "Interaction force estimation on a built-in position sensor for an electrostatic visuo-haptic display," *ROBOMECH Journal*, vol. 3, p. 11, Dec. 2016.

[62] M. Wiertlewski, R. F. Friesen, and J. E. Colgate, "Partial squeeze film levitation modulates fingertip friction," *Proceedings of the National Academy of Sciences*, vol. 113, pp. 9210–9215, Aug. 2016.

[63] S. Bochereau, B. Dzidek, M. Adams, and V. Hayward, "Characterizing and imaging gross and real finger contacts under dynamic loading," *IEEE Transactions on Haptics*, vol. PP, no. 99, pp. 1–1, 2017.

[64] E. L. Hutchins, J. D. Hollan, and D. A. Norman, "Direct Manipulation Interfaces," *Hum.-Comput. Interact.*, vol. 1, pp. 311–338, Dec. 1985.

[65] D. A. Norman, *The Design of Everyday Things*. Basic Books, Sept. 2002.

[66] B. E. Stein and M. A. Meredith, *The Merging of the Senses*. MIT Press, Jan. 1993.

[67] K. E. MacLean, "Haptic Interaction Design for Everyday Interfaces," *Reviews of Human Factors and Ergonomics*, vol. 4, pp. 149–194, Oct. 2008.

[68] W. W. Gaver, "The SonicFinder: An Interface That Uses Auditory Icons," *Hum.-Comput. Interact.*, vol. 4, pp. 67–94, Mar. 1989.

[69] Z. Ren, H. Yeh, R. Klatzky, and M. C. Lin, "Auditory Perception of Geometry-Invariant Material Properties," *IEEE Transactions on Visualization and Computer Graphics*, vol. 19, pp. 557–566, Apr. 2013.

[70] V. Jousmäki and R. Hari, "Parchment-skin illusion: sound-biased touch," *Current Biology*, vol. 8, pp. R190–R191, Dec. 1998.

[71] J. Huang, D. Gamble, K. Sarnlertsophon, Xiaoqin Wang, and S. Hsiao, "Feeling Music: Integration of Auditory and Tactile Inputs in Musical Meter Perception," *PLoS ONE*, vol. 7, pp. 1–11, Oct. 2012.

APPENDIX A

Tactile Soundboard: Example Human Computer Interface using Broadband Electroadhesion

A.1. Implementation

Tactile Soundboard was designed to be robust and to use as many off-the-shelf parts as possible. There is only one component (the high performance electroadhesion amplifier) that cannot be easily purchased or constructed. In this section, I review the design decisions behind each piece of hardware selected, and discuss the modular, audio-based software approach.

A.2. System Design

Tactile Soundboard has 6 main hardware components, which can be seen in Fig A.1: An infrared (IR) touch sensing frame, a high resolution visual display and stand, a high performance audio hardware interface, a compact workstation PC, a custom fitted transparent electroadhesive surface, and an accompanying high voltage capable current controlled amplifier.

Touch sensing is done via a low cost, commercially available IR touch frame (PQ Labs 24 inch model 4S). It has an effective refresh rate of approximately 160 Hz. Positional accuracy is on the order of a few millimeters, but it supports an interpolated position through its native SDK down to approximately 16 microns. This in-plane optical finger
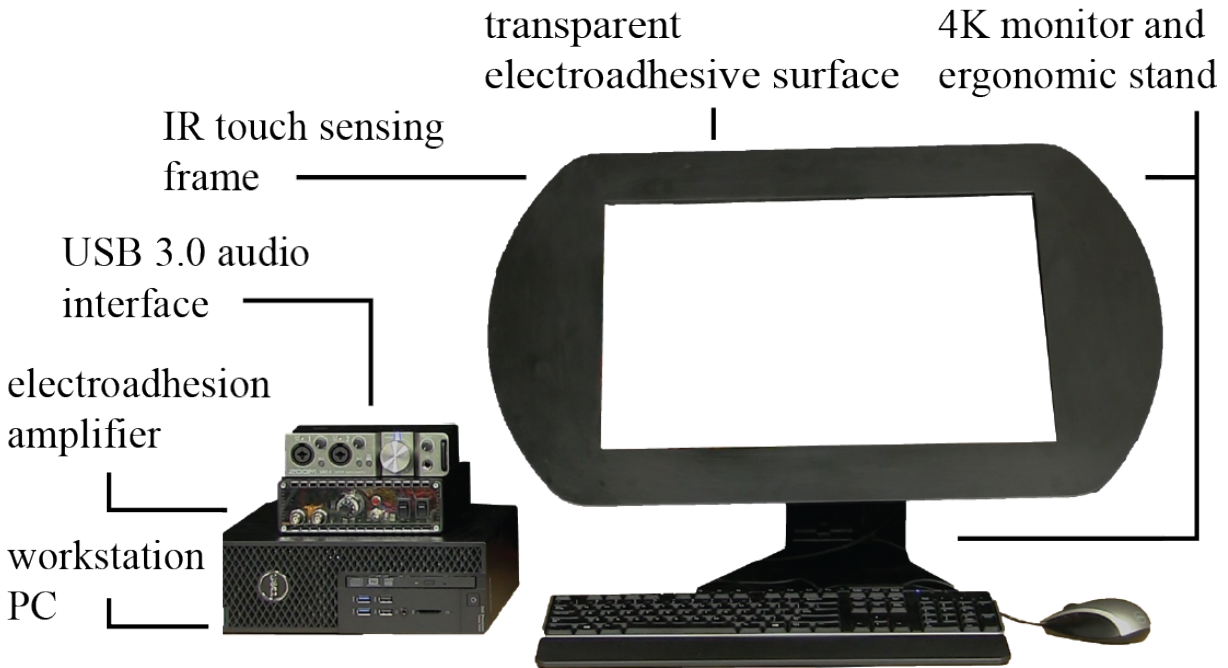
Figure A.1. Main system components that make up Tactile Soundboard. Tactile input and audio-tactile-visual output is integrated together on the electroadhesion enabled interaction surface.

position sensor was chosen primarily for flexibility, ease of implementation, and a publicly available SDK.

The visual monitor (ASUS MG24UQ) has a pixel resolution of 3840 x 2160, a pixel density of 180 dots per inch (DPI), and is driven at 60 frames per second (fps). The monitor is mounted on a ergonomic touch screen stand with adjustable tension control (Ergotron Neo-flex), allowing both its height and tilt to be adjusted. The workstation PC runs Windows 7, and contains a dedicated graphics card to handle 4K output.

The USB 3.0 audio interface (ZOOM UAC-2) was chosen because of its high performance specifications. It supports 24 bit depth conversion and an output bandwidth of 20 Hz to 60 kHz when run at a 192 kHz sampling rate. This sampling rate and bandwidth is

necessary for the system, as the broadband electroadhesive technique performs ultrasonic amplitude modulation at 25 kHz in software, and most conventional audio interfaces only support up to a 22 kHz sampling rate. The audio interface is also supported by a native Audio Stream Input/Output (ASIO) protocol driver, which bypasses typical Windows operating system software layers and accesses the audio hardware directly. Implementation of this ASIO driver resulted in almost 4x reduction in round trip latency.

A.3. Custom Electroadhesion Components

The electroadhesive surface used for Tactile Soundboard is the same 3M microtouch type of panel used in [3]. It was cut to size to fit in the IR touch frame, and the internal capacitive connections were shorted, yielding a direct connection to the ITO touch panel. The advancements that enabled broadband electroadhesion was not in this surface hardware layer, but rather the supporting high performance amplification and double sideband, full carrier modulation techniques (DSBFC) used to drive it.

The high bandwidth current controlled amplifier is necessary because the bandwidth of the electroadhesion force relies directly on the capabilities of the amplifier used, and a flat amplifier response leads to a flat force response applied to the skin, as demonstrated earlier in this thesis. The design and construction of the amplifier is given in detail in Appendix B.

A.4. Software

Software for Tactile Soundboard is created using the open source C++ audio framework Juce (juce.com), which allows both standalone and plug-in type applications to be

compiled. Most custom applications are created as Virtual Studio Technology (VST) plug-ins. This allows them to be loaded into a plug-in host runtime environment and interface in real-time with a wide array of pre-existing audio tools, effects, and synthesizers. This approach to software design and prototyping allows effects such as convolution reverb, equalization, and mixing to be easily applied and computationally efficient. Juce also provides a library of lightweight graphical user interface classes, and supports integration with OpenGL.

A.5. Demonstrations

The software architecture of Tactile Soundboard allows for rapid prototyping of audio-tactile-visual interactions. This capability is demonstrated through four applications below, each of which contains elements of custom software and precompiled audio plugins or existing audio processing libraries.

A.5.1. Audio-tactile-visual Toggle Switch

There is a long history of using haptics to display virtual reality simulations [67], and of using audio interfaces to replicate physical characteristics of everyday sound [68]. Inspired by that history, I implemented an audio-tactile-visual toggle switch, as seen in Fig. A.2. As the user starts to push on the switch, electroadhesion is increased, resisting their motion. As the user continues to slide, a threshold location is reached at which point the switch flips and the electroadhesive force turns off. This interaction alone provides compelling audio-tactile feedback to the user, as the release of the switch and the snap of the finger can be both felt and heard.
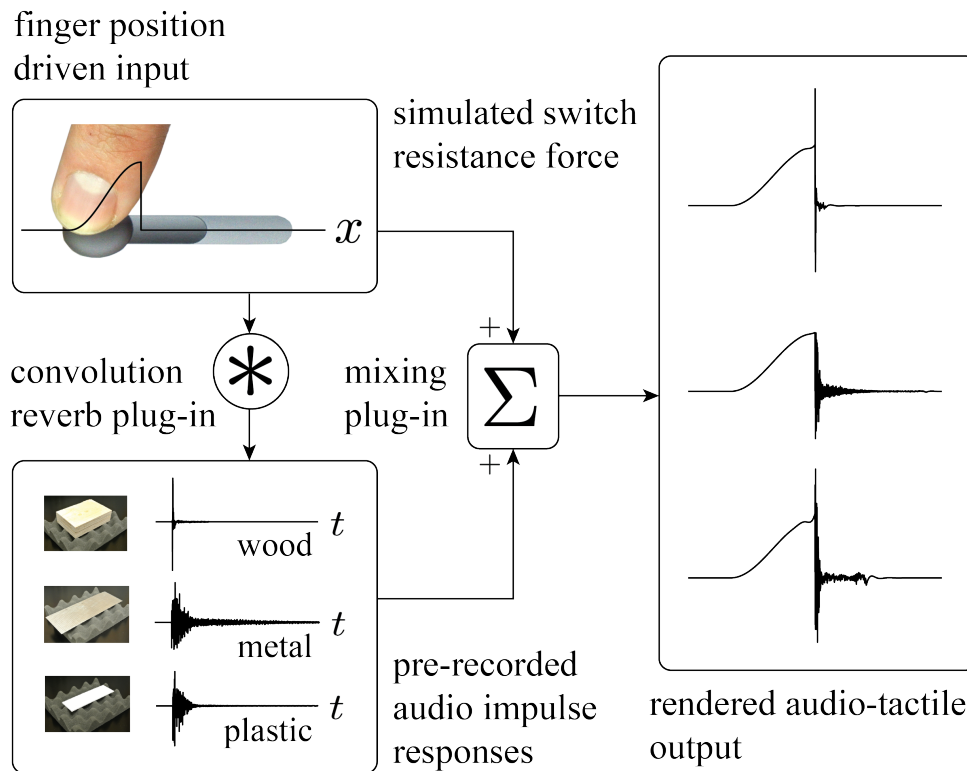
Figure A.2. Illustration of a combination audio-tactile switch widget. Simulated resistance force is mapped as a function of position, while temporal impulse response are recorded and mixed with haptic effects in real-time.

I can also augment this experience through the use of a convolution reverb plug-in. I took three types of materials, plastic, wood, and metal, that have been shown to be perceptually discriminable from percussive impulse sound alone [69], and recorded their impulse responses with a hammer and microphone. These responses formed a material response library that could then be convolved with the audio-tactile switch output, and mixed back into to the original force simulation. The resulting interaction now conveys the same audio-tactile resistance and snap, but the resulting click of the switch is instilled with the acoustic properties of the various sampled materials.
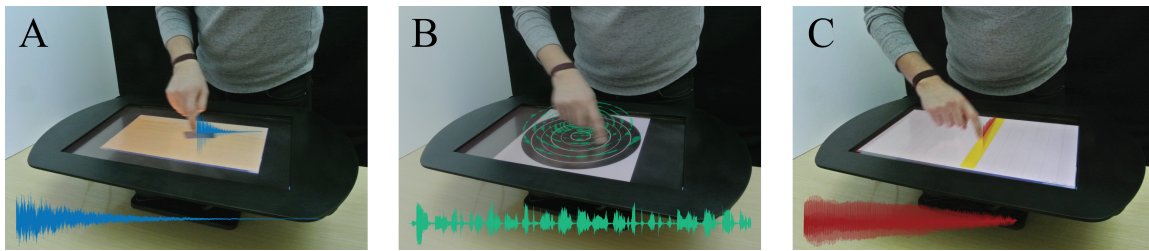
Figure A.3. Three demonstrations of audio-tactile interactions rapidly prototyped with a combination of custom written software and common audio processing plugins and libraries. (A) Wood sanding interaction (B) Rotational velocity control of music playback (C) Bowing a violin using a virtual midi keyboard. Colored traces are representative of the audio-tactile waveform that is rendered to the fingertip.

A.5.2. Playing a Virtual Instrument

Tactile Soundboard can be used to build and play virtual instruments, Fig A.3C. I modified a virtual midi keyboard so that the finger can be stroked laterally across the keys, or alternatively along the keys, which is similar to bowing a stringed instrument. The output of the midi keyboard is routed to the input of a free virtual violin synthesizer plugiin, which takes the midi control and pitch information, and renders the audio-tactile output of a real, sampled violin. The resulting playback is no doubt similar to Gray's original electroadhesion powered violin, but here I am in complete control of the musical timbre of the interaction, and can easily reroute the midi input to trigger any number of musical synthesizers or virtual instruments. This method of combining a spatially mapped interface with pre-existing audio synthesis tools shows great promise for high-fidelity, yet rapidly prototyped, experimental interactions.

A.5.3. Sanding Wood

Adjusting the levels of audio and tactile frequency bands relative to one another is known to have a dramatic effect on tactile experiences [70]. I prototyped a virtual sanding application which allows users to experience software generated audio-tactile surface texture effects, Fig. A.3A. Pink noise was generated from an audio plug-in and fed into a custom GUI plug-in which one, modulates the noise amplitude by the velocity of the finger; and two, draws the wood and sandpaper to the screen. With no equalization applied, high frequency content is passed through the finger giving the experience a crisp and dry feeling. An equalization filter plug-in allows higher frequencies to be attenuated, leading to a markedly different overall perception, similar to the illusion of dampness reported in [70].

A.5.4. Controlling Musical Performance

Because music is almost always perceived both tactilely and audibly, the ability to generate music by the finger while directly experiencing both touch and sound could open up new avenues for learning, performance, and experience [71]. I developed a music playback application that leverages the conceptual model of an LP record player for audio-tactile playback and control, Fig A.3B. A custom graphical user interface displays a black disk and maps a user's rotational velocity to a variable playback rate, which is then implemented with an audio effect library. This method not only allows users to control the start, stop, and playback rate of music with their motion, it allows them to feel the low frequency bass and beats of the song, letting them sync their movement in space accordingly.

APPENDIX B

Transconductance Amplifier Theory and Design

The transconductance amplifier was enabled by three main components, a high-voltage DC-DC converter, a high common mode voltage differential amplifier, and a network of high-voltage capable bias transistors and resistors. In addition to the main amplifier, there are safety circuits included, and measuring circuits. These parts are described in the bill of materials (BOM), schematic, and functional schematic below, Fig B.1. The circuit it based around the principle of a Howland current source, using the internal resistors of the differential amplifier and a single external feedback resistor, which sets the transconductance gain. As a practical description of the circuit, the differential amplifier will drive its output terminal to whatever voltage is needed such that the differential voltage across the feedback resistor (which is buffered and sent back to the diff amp), is equal to the differential input to the entire amplifier.

The key to high voltage operation of the circuit, however, is that the differential amplifier is not simply driven from stable high-voltage supplies. Instead, the power supplies to the diff amp themselves are part of the feedback circuit, via the arrangement of the bias transistors and resistors (the ref buffer is also powered by this floating power supply). This is a so-called bootstrapping power supply configuration, as the power supplies adjust themselves to whatever voltage is needed on the output. These components act to keep the power supplied to the differential amplifier approximately $\pm 17V$ above and below the output of the diff amp at all times (unless, of course, the amplifier is driven to a power
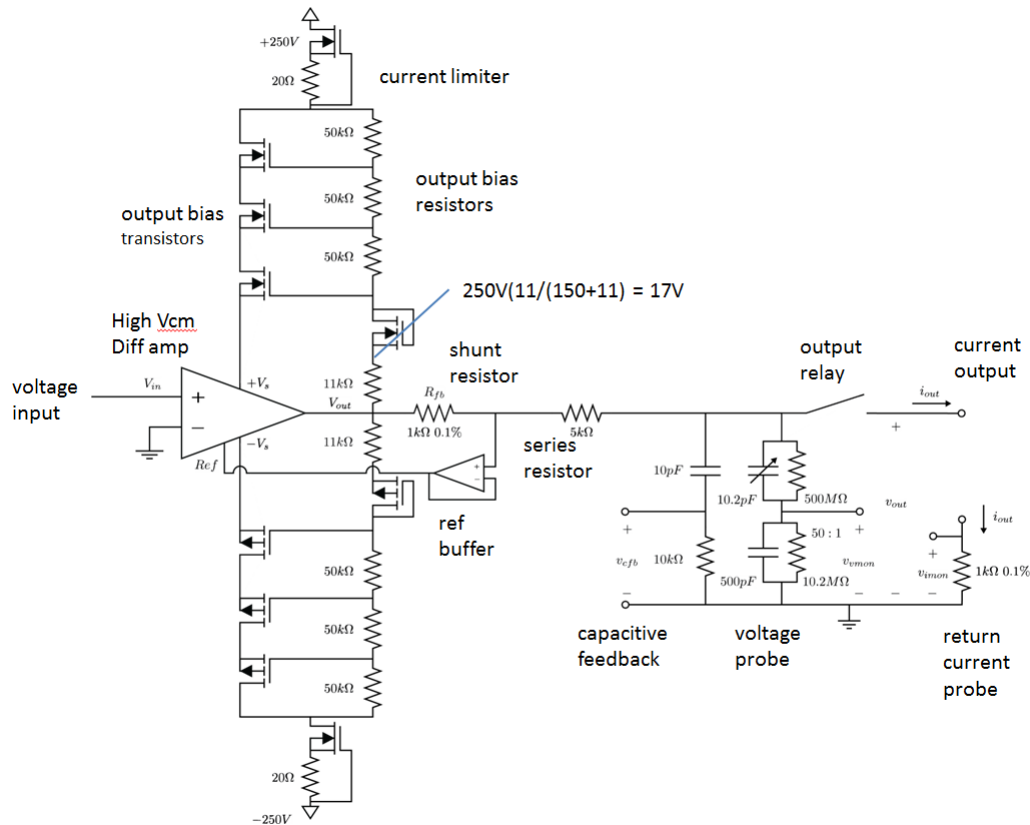
Figure B.1. Functional circuit schematic, showing the basic building block circuits for the transconductance amplifier and measurement circuit.

supply rail). The transistors are all operated in a source-follower configuration, and multiple transistors are used to lessen the burden voltage across each individual transistor, and reduce the effect of heat dissipated through any one transistor. The bias resistors are then used to simply set the DC operating point of each transistor, making sure that the voltage remains relatively spread across each one.

The symmetrical nature of the circuit allows both p-channel and n-channel devices to be used with nearly an identical schematic configuration. A sample calculation is shown in Fig B.1, which shows the nominal voltage at the node above the $11\text{k}\Omega$ bias resistor. This node voltage represents the voltage that will appear on the positive floating supply

of the diff amp (with respect to the output voltage of course). It is a simple resistor divider calculation, and can be used in cases where the applied voltage (or transistor configuration) wishes to be altered.

Another key to this amplifier's operation is the high voltage differential amplifier, which can sustain up to 600 V of common mode voltage on its two input terminals. This specification is tested when the differential amplifier floats towards the positive or negative high voltage supply rails. For instance, if the diff amp is floating at the +250V rail, the inputs to the amplifier (which are near ground potential) will have a -250V common mode voltage with respect to the amplifier. This voltage is subtracted off by the high CMRR of the diff amp (approx 90dB), but can still negatively effect the output of the amplifier for high output voltage. Effectively, it produces a negative output resistance to ground of 20 MΩ (with respect to the input voltage).

Feeding current to the main amplifier and biasing network are two current limited devices, which have a shunt resistor and depletion mode pass transistor. Combined, these two components become incredibly high impedance if the current through the pass transistor becomes too high (approx greater than 20mA). In addition, a series output resistor limits the current output of the device should a short circuit occur, and an isolated reed-switch relay physically disconnects the amplifier from the output.

Attached to the output is a capacitive feedback probe, voltage monitor probe, and return current monitor probe. These circuits monitor the output and either are buffered and are available for external use, or are internally buffered and used as positive feedback to the main amplifier input.

136

HIGH VOLTAGE POWER SUPPLY

HV Current Protection FETS

Enable LED

Enable Switch

HV Output Enable

Capacitive Current Feedback

Series Safety Resistors

50:1 High Impedance Voltage Probe

OUTPUT SAFETY, MONITORING, & FEEDBACK

MAIN TRANSCONDUCTANCE AMPLIFIER

HV Rail Pilot Light

MAIN POWER SUPPLY IN

Main Power LED

INPUT AND SIGNAL CONDITIONING

Gain Selection Switch

VAR. GAIN_OUT

DC_OFFEST_IN

DC Pol Select

Front Pot

MAIN_IN

Backboard Conn

1V Precision Reference

High Common Mode Voltage Diff Amp

ADB479ARZ

U3

TITLE: RevB_FrontBoard

Document Number:

Date: 5/18/2017 11:00 AM

REV:

Sheet: 1/1

TITLE: RevB_BackBoard

Document Number:

REV:

Date: 4/11/2017 5:07 PM

Sheet: 1/1

PSU STANDOFFS

Fan Pwr

CONN. TE-MINICT, 2POS

MO1FTH, 2NM

+5V

GND

+5V

GND

TVS_DIODE_18V5_DIODE_18V

GND

GND

D1

D2

CONN. 1/4_STEREO

IN+

IN-

GND

GND

+5V

GND
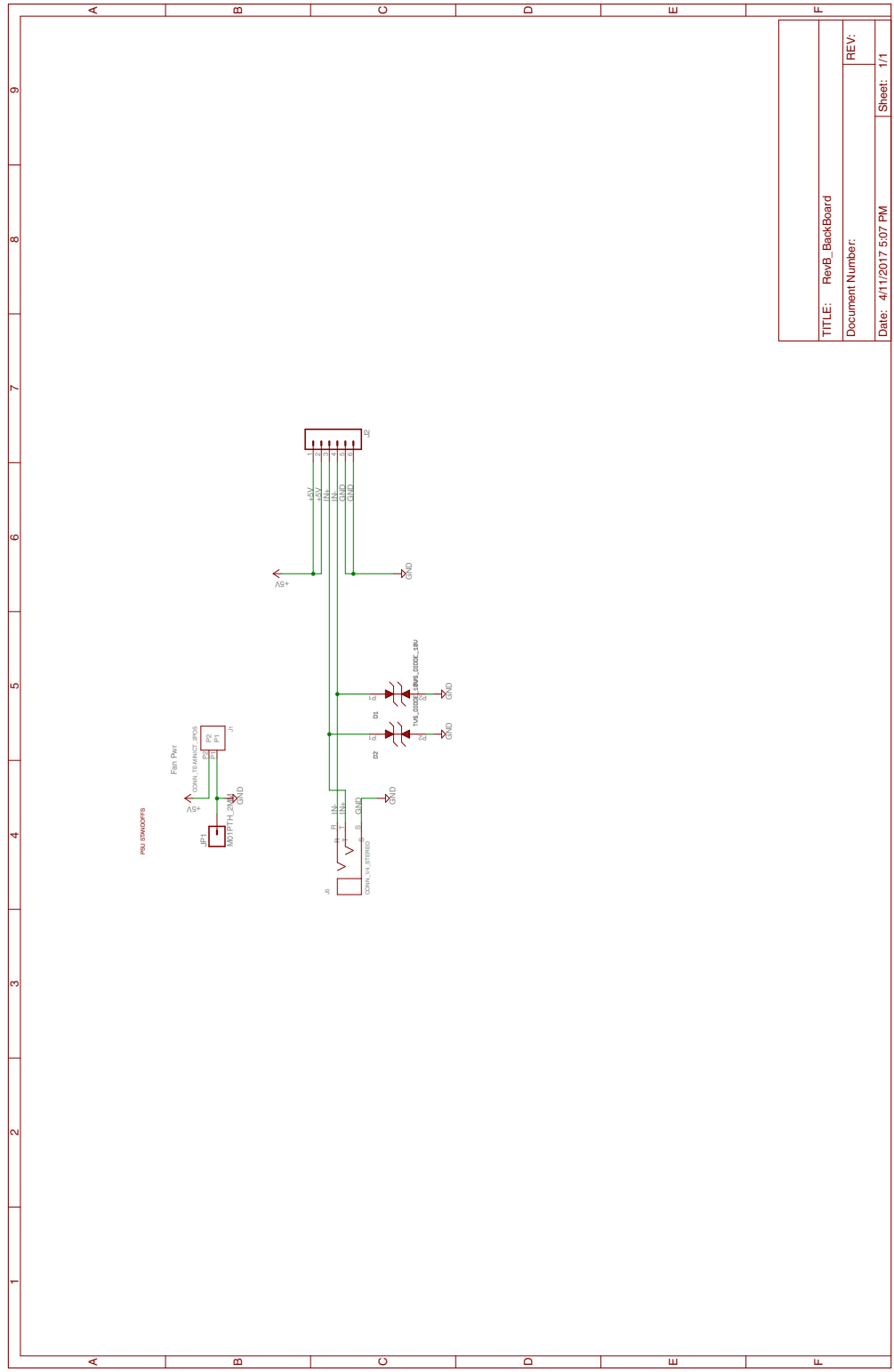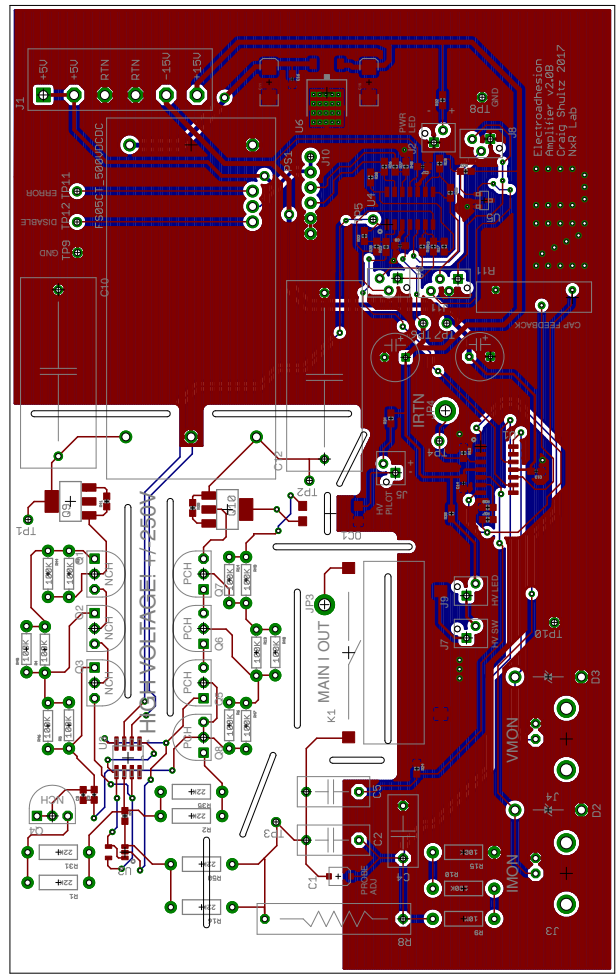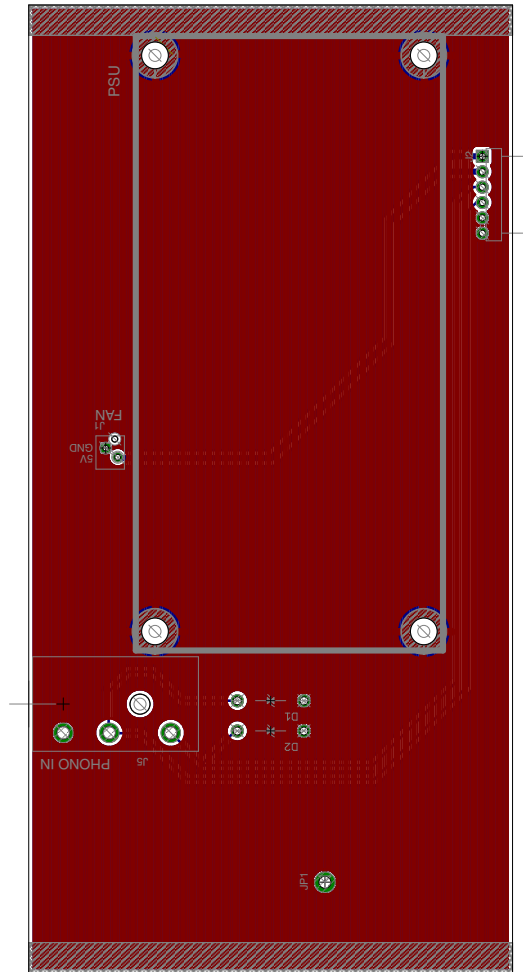
Name	Ref Des (FRONT)	Ref Des (BACK)	Manufacturer	P/N
Transistors				
MOSFET P-CH 500V 0.1A TO92-3	Q5 Q6 Q7 Q8		Microchip Technology	VP2450N3-G
MOSFET N-CH 800V 0.3A TO-92	Q1 Q2 Q3 Q4		STMicroelectronics	STQ1NK80ZR-AP
MOSFET N-CH 800V SOT-223	Q9 Q10		IXYS Integrated Circuits Division	CPC3980ZTR
OPTOISOLATOR 5KV DARLINGTON 4SMD	OC1		Fairchild Semiconductor	FOD852SD
Op amps				
IC OPAMP RRI/O 14SOIC	U1 U4		Texas Instruments	OPA4192IDR
IC OP AMP PREC E-TRIM 5SOT23	U2		Texas Instruments	OPA191IDBVR
IC OPAMP DIFF 130KHZ RRO 8SOIC	U3		Analog Devices Inc.	AD8479BRZ
Protection				
TVS DIODE 10VWM 14.5VC 1.5KE	D2 D3	D1 D2	Vishay Semiconductor	ICTE10C-E3/54
REED RELAY 1 FORM A 12V SMD	K1		Standex-Meder Electronics	KT12-1A-40L-SMD
Power Supplies				
AC/DC CONVERTER 5V +/-15V 40W	PSU		XP Power	ECM40UT33
MACHINE SCREW PAN PHILLIPS M3	PSU		B&F Fastener Supply	MPMS 003 0008 PH
WASHER SPLIT LOCK M3 STEEL	PSU		B&F Fastener Supply	MLWZ 003
ROUND STANDOFF M3 STEEL 5MM	PSU		Wurth Electronics Inc	9774050360R
IC VREF SHUNT 1V SOT23-3	U5		Analog Devices Inc.	ADR510ARTZ-REEL7
IC REG LDO 12V 1A TO252-3	U6		Fairchild/ON Semiconductor	KA7812ERTM
DUAL O/P, DC-HV DC PCB MOUNT, 10	PS1		XP Power	FS05CT-12
Connectors and Cables				
CONN BNC JACK R/A 50 OHM PCB	J3 J4		Molex	731375003
4MM SAFETY JACK, SOLDER HOLE - P	ENCLOSURE		B&K Precision	CT2240-6

4MM SAFETY JACK, SOLDER HOLE - P	ENCLOSURE		B&K Precision	CT2240-2
4MM SAFETY JACK, SOLDER HOLE - P	ENCLOSURE		B&K Precision	CT2240-5
TEST POINT PC MINI .040"D BLACK	TP1 TP2 TP3 TP4 TP5 TP6 TP7 TP8 TP9 TP10		Keystone Electronics	5001
TEST LEAD BANANA TO GATOR 39.4"	ENCLOSURE		Cal Test Electronics	CT3805-100
CONN HEADER RT/A .100 6POS 30AU	ENCLOSURE	J2	TE Connectivity AMP Connectors	103906-5
FLEX CABLE - AFG06G/AF06/AFE06T	JP1	JP2	TE Connectivity AMP Connectors	A9CAG-0606F
CABLE ASSY MINI CT 3POS	ENCLOSURE		TE Connectivity AMP Connectors	2058943-2
CABLE ASSY MINI CT 2POS	ENCLOSURE		TE Connectivity AMP Connectors	2058943-1
CABLE ASSY MINI CT 4POS	ENCLOSURE		TE Connectivity AMP Connectors	2058943-3
2 Positions Header, Shrouded Connector 0.059" (1.50mm) Through Hole Tin	J2 J5 J7 J8	J1	TE Connectivity AMP Connectors	292207-2
3 Positions Header, Shrouded Connector 0.059" (1.50mm) Through Hole Tin	J6 J8	J3	TE Connectivity AMP Connectors	292207-3
4 Positions Header Connector 0.059" (1.50mm) Through Hole Tin			TE Connectivity AMP Connectors	292207-4
0.250" (6.35mm) Quick Connect Female 14-16 AWG Crimp Connector Fully Insulated	PSU		TE Connectivity AMP Connectors	3-350819-2
0.187" (4.75mm) Quick Connect Female 18-22 AWG Crimp Connector Fully Insulated	PSU		TE Connectivity AMP Connectors	2-520194-2
LOOM KIT ECM40/60DT	PSU		XP Power	ECM40/60DT LOOM
CORD 18AWG 3COND 3.3' SVT	PSU		Tensility International Corp	839-1201-ND
GROMMET RUBBER GRAY	PSU		Essentra Components	LTG-39897

WIRE TEST LEAD 18AWG RED 10'	ENCLOSURE		Mueller Electric Co	WI-M-18-10-2
WIRE TEST LEAD 18AWG BLK 10'	ENCLOSURE		Mueller Electric Co	WI-M-18-10-0
6.35mm (0.250", 1/4") - Headphone Phone Jack Stereo Connector Solder		J5	Switchcraft Inc.	RA49B12B
CONN PLUG STEREO 6.35MM RA 3COND	ENCLOSURE		Tensility International Corp	50-00185
Capacitors				
CAP POLYMER 270UF 20% 16V T/H	C6 C7		Nichicon	RL81C271MDN1KX
CAP MICA 10PF 5% 1KV RADIAL	C2 C5		Cornell Dubilier Electronics (CDE)	CDV19CF100JO3F
CAP TRIMMER 1.2-3PF 500V SMD	C1		Sprague-Goodman	SGC3S030
CAP MICA 620PF 1% 500V RADIAL	C4		Cornell Dubilier Electronics (CDE)	CD19FD621FO3F
CAP CER 0.1UF 100V X7S 0603	C16 C17 C8 C3 C9 C13 C14		TDK Corporation	CGA3E3X7S2A104M 080AB
CAP FILM 2UF 10% 1.1KVDC RADIAL	C10 C12		EPCOS (TDK)	B32774D0205K
CAP TANT 10UF 25V 10% 2413	C11 C15		KEMET	T491C106K025AT
Resistors				
RES SMD 10K OHM 1% 1/10W 0603	R33 R37		Yageo	RC0603FR-0710KL
RES SMD 1K OHM 1% 1/10W 0603	R32 R24 R38 R34 R30		Yageo	RC0603FR-071KL
RES SMD 47 OHM 5% 1/10W 0603	R39 R41		Yageo	RC0603JR-0747RL
RES MF HV .25W 10M OHM 1% AXIAL	R9		Stackpole Electronics Inc.	RNV14FAL10M0
RES MF HV .25W 100K OHM 1% AXIAL	R3 R4 R5 R6 R13 R14 R15 R10 R44 R45 R46 R47 R48 R49		Stackpole Electronics Inc.	RNV14FAL100K
RES 500M OHM 1.5W 1% RADIAL	R8		Ohmite	SM104035006FE

RES 22K OHM 1/4W 5% AXIAL	R2 R3 R31 R35 R16 R50		Yageo	HHV-25JR-52-22K
RES SMD 1K OHM 0.1% 1/10W 0603	R7 R12 R17 R43		Susumu	RG1608P-102-B-T5
RES SMD 10K OHM 0.1% 1/10W 0603	R26 R27 R28 R40 R18 R19 R25 R20 R22 R23		Susumu	RG1608P-103-B-T5
TRIMMER 10K OHM 0.75W TH	R11		TT Electronics/BI	89PR10KLF
POT 20K OHM 2W WIREWOUND LINEAR	ENCLOSURE		TT Electronics/BI	7286R20KL.25
Enclosure				
BOX ALUM BLACK/NAT 8.66"LX6.5"W	ENCLOSURE		Hammond Manufacturing	1455T2201
DIAL-7/8" 10-TURN 1/4" SHAFT	ENCLOSURE		TT Electronics/BI	2696
SWITCH TOGGLE SPDT 5A 120V	ENCLOSURE		E-Switch	100SP1K1B25M1QEH
SWITCH TOGGLE SP3T 5A 120V	ENCLOSURE		E-Switch	100DP6K2B25M1QE
SWITCH ROCKER SPST 15A 125V	ENCLOSURE		E-Switch	R1966ABLKBLKEFGRN
SWITCH ROCKER SPST 15A 125V	ENCLOSURE		E-Switch	R1966ABLKBLKEFRED
FAN AXIAL 25X10MM VAPO 5VDC WIRE	ENCLOSURE		Sunon Fans	MC25100V2-000U-A99
PNL MNT W/ WIRE 700NM 2MCD RED	ENCLOSURE		Bivar Inc.	MPR3RD